



6-2021

Novel Low Temperature Properties of Filled and Unfilled Single Crystal IrSb₃

Matthew Cook

Western Michigan University, mscook776@gmail.com

Follow this and additional works at: <https://scholarworks.wmich.edu/dissertations>

 Part of the Condensed Matter Physics Commons

Recommended Citation

Cook, Matthew, "Novel Low Temperature Properties of Filled and Unfilled Single Crystal IrSb₃" (2021).
Dissertations. 3724.

<https://scholarworks.wmich.edu/dissertations/3724>

This Dissertation-Open Access is brought to you for free and open access by the Graduate College at ScholarWorks at WMU. It has been accepted for inclusion in Dissertations by an authorized administrator of ScholarWorks at WMU. For more information, please contact wmu-scholarworks@wmich.edu.



NOVEL LOW TEMPERATURE PROPERTIES OF FILLED AND
UNFILLED SINGLE CRYSTAL IrSb₃

by

Matthew Cook

A dissertation submitted to the Graduate College
in partial fulfillment of the requirements
for the degree of Doctor of Philosophy
Physics
Western Michigan University
June 2021

Doctoral Committee

Clement Burns, Ph.D.
Pnina Ari-Gur, Ph.D.
Asghar Kayani, Ph.D.
Lisa Paulius, Ph.D.

NOVEL LOW TEMPERATURE PROPERTIES OF FILLED AND UNFILLED SINGLE CRYSTAL IrSb₃

Matthew Cook, Ph.D.

Western Michigan University, 2021

The skutterudite family of materials has garnered a lot of attention in the condensed matter community and it persists to be an important system for exploring the fundamental physics of solids. The initial interest into compounds with this common structure was due to their promising thermoelectric properties giving the possibility of efficient energy harvesting. Since, there has been a huge effort to systematically synthesize new filled skutterudite compounds, as nearly every type of strongly correlated behavior has been found within this family. As the field of topological materials has gained momentum, these materials have also been given a renewed interest in this regard. The skutterudite IrSb₃ has been characterized in past studies with a focus on its (high temperature) thermoelectric properties, however not much work has been reported on the low temperature properties of single crystal samples. There have also been conflicting results found in *ab initio* calculations that have been carried out in the past few decades.

In this study, I report novel properties of single crystal IrSb₃ grown using a horizontal flux transport method, those that are in contrast to previous measurements and theoretical calculations. I also discuss the implications of filling IrSb₃ with a rare-earth ion and the characterization of the new single crystal skutterudite, Pr_{0.5}Ir₄Sb_{10.2}Sn_{1.8}. The structure and composition of these materials are first confirmed through powder x-ray diffraction and energy dispersive x-ray spectroscopy. The physical characterization is carried out through low temperature measurements of the specific heat, resistivity, and magnetization. These measurements show that IrSb₃ can express behavior consistent with a zero-gap point fermi surface semimetal, as some calculations predict. This material also shows many transport characteristics common to topological semimetals, such as ultrahigh mobility, extremely large magnetoresistance, and sublinear magnetoresistance. The Pr filled skutterudite shows heavy

fermion correlations in the resistivity and specific heat, while the magnetic susceptibility predicts a Kondo temperature $T_K \approx 4 K$. There is also evidence of a superconducting transition seen as a small drop in the resistivity and a diamagnetic signal in the magnetization. Only a very small fraction of material becomes superconducting at low temperatures, possibly due to an impurity phase, superconductivity of reduced dimensionality, or sample inhomogeneity.

Copyright by
Matthew Cook
2021

ACKNOWLEDGMENTS

I would first like to thank Dr. Clement Burns, my Ph.D. advisor and mentor. He has thought of and guided me through many fruitful projects, most of which were filled with many unexpected surprises. His calm and assuring demeanor made working under him a very pleasant experience, as I was never made to feel less than adequate. I learned about many aspects of pursuing a career in academia and research through our almost daily meetings, and for that I am eternally grateful.

I would also like to thank Dr. Pnina Ari-Gur for the constant use of the x-ray diffractometer within her lab at WMU. I am also appreciative of Dr. Steve Kaczmarek for granting access to his scanning electron microscope and being extremely communicative along the way. I would like to acknowledge Dr. Ulrich Welp of Argonne National Lab as well for allowing me to collaborate on specific heat measurements on the ferromagnetic superconductor $\text{RbEuFe}_4\text{As}_4$. I also greatly appreciate Dr. Lisa Paulius and Dr. Asghar Kayani for joining my PhD committee and being extremely helpful and responsive along the way.

I would like to thank my wife and her family for always showing me support through this journey. The sacrifices that she has made in order for me to finish my program will always be remembered and reciprocated. My daughter also deserves some recognition, as she has helped me learn to make good use of my time and learn when to take a step back for play time.

Matthew Cook

TABLE OF CONTENTS

ACKNOWLEDGEMENTS.....	ii
LIST OF TABLES.....	v
LIST OF FIGURES.....	vi
CHAPTER	
1 INTRODUCTION.....	1
1.1 History and Motivation.....	1
1.2 Theoretical Background.....	5
1.2.1 Local Moment Physics.....	5
1.2.1.1 Heavy Fermions and Magnetic Moment Interactions.....	5
1.2.1.2 Kondo Lattice.....	6
2 METHODS.....	9
2.1 Crystal Growth.....	9
2.1.1 IrSb ₃ Horizontal Flux Growth.....	9
2.1.2 Pr _{0.5} Ir ₄ Sb _{10.2} Sn _{1.8} Flux Growth.....	11
2.2 Structure and Composition.....	13
2.2.1 Powder X-ray Diffraction.....	13
2.2.2 Energy Dispersive X-ray Spectroscopy.....	14
2.3 Physical Properties.....	15
2.3.1 Resistivity.....	15
2.3.2 Magnetization.....	17

Table of Contents---Continued

CHAPTER	
2.3.3 Specific Heat.....	19
3 ANALYSIS AND DISCUSSION.....	22
3.1 IrSb ₃	22
3.1.1 Composition.....	22
3.1.2 Magnetization.....	23
3.1.3 Specific Heat.....	24
3.1.4 Resistivity.....	26
3.1.4.1 Longitudinal Resistivity.....	26
3.1.4.2 Magnetoresistance.....	30
3.1.4.3 Hall Resistivity.....	34
3.2 Pr _{0.5} Ir ₄ Sb _{10.2} Sn _{1.8}	37
3.2.1 Crystallography and Composition.....	37
3.2.2 Magnetization.....	39
3.2.3 Specific Heat.....	43
3.2.4 Resistivity.....	53
4 CONCLUSION.....	60
REFERENCES.....	64

LIST OF TABLES

1. Relative Composition of IrSb₃ from EDS Measurements.....22
2. Rietveld Refinement Parameters for Pr_{0.56}Ir₄Sb_{10.08}Sn_{1.92}.....39

LIST OF FIGURES

1.1	Unit cell of filled skutterudite structure.....	2
2.1	Horizontal flux transport growth of IrSb ₃	10
2.2	Horizontal growth of IrSb ₃ when first removed from furnace.....	10
2.3	Largest single crystal IrSb ₃ samples.....	11
2.4	IrSb ₃ single crystals wired for resistivity measurements.....	16
2.5	Small IrSb ₃ single crystal mounted on quartz rod for magnetization.....	18
2.6	IrSb ₃ single crystal mounted on sample platform of PPMS specific heat option.....	20
3.1	EDS graph for IrSb ₃ showing peaks attributed to each element.....	23
3.2	SEM picture of sample 73.1 of single crystal IrSb ₃	23
3.3	The temperature independent magnetic susceptibility of single crystal IrSb ₃	24
3.4	High temperature specific heat of IrSb ₃	25
3.5	Low temperature specific heat divided by temperature versus temperature squared of IrSb ₃	25
3.6	Normalized temperature dependence of the resistivity of three samples of IrSb ₃	27
3.7	Arrhenius plot of IrSb ₃ sample 73.0 for $70 K \leq T \leq 125 K$	28
3.8	Resistivity of IrSb ₃ sample 73.0 for temperatures $38 K \leq T \leq 100 K$	29
3.9	Low temperature resistivity versus temperature for IrSb ₃	30
3.10	Low temperature resistivity versus temperature in various fields for IrSb ₃	31
3.11	Measurement geometry for magnetoresistance for IrSb ₃	31

List of Figures–Continued

3.12	MR% of IrSb ₃ for various temperatures with field along the <i>a</i> axis.....	33
3.13	MR% of IrSb ₃ for various temperatures with field along the <i>b</i> axis.....	33
3.14	Symmetrized Hall resistivity versus temperature for IrSb ₃	35
3.15	Hall coefficient (left) and carrier concentration (right) for IrSb ₃	36
3.16	Hall mobility versus temperature for IrSb ₃	37
3.17	Photograph of Pr _{0.5} Ir ₄ Sb _{10.2} Sn _{1.8} at x650 magnification.....	38
3.18	XRPD pattern and refinement for Pr _{0.5} Ir ₄ Sb _{10.2} Sn _{1.8}	38
3.19	The molar magnetic susceptibility (left axis) and its inverse (right axis) for Pr _{0.5} Ir ₄ Sb _{10.2} Sn _{1.8}	40
3.20	ZFC and FC magnetic susceptibility near the superconducting transition for Pr _{0.5} Ir ₄ Sb _{10.2} Sn _{1.8}	42
3.21	Hysteresis loops for Pr _{0.5} Ir ₄ Sb _{10.2} Sn _{1.8}	42
3.22	High temperature specific heat for Pr _{0.5} Ir ₄ Sb _{10.2} Sn _{1.8}	44
3.23	Low temperature specific heat for Pr _{0.5} Ir ₄ Sb _{10.2} Sn _{1.8}	44
3.24	Low temperature specific heat over temperature for Pr _{0.5} Ir ₄ Sb _{10.2} Sn _{1.8}	45
3.25	Low temperature electronic and magnetic specific heat over temperature for Pr _{0.5} Ir ₄ Sb _{10.2} Sn _{1.8}	47
3.26	Low temperature electronic and magnetic specific heat over temperature versus temperature squared for Pr _{0.5} Ir ₄ Sb _{10.2} Sn _{1.8}	47
3.27	Low temperature specific heat (left axis) and corresponding entropy (right axis) for 0.25 K ≤ <i>T</i> ≤ 20 K for Pr _{0.5} Ir ₄ Sb _{10.2} Sn _{1.8}	48
3.28	Low temperature field dependent specific heat for Pr _{0.5} Ir ₄ Sb _{10.2} Sn _{1.8}	49
3.29	The nuclear specific heat with field dependence inset for Pr _{0.5} Ir ₄ Sb _{10.2} Sn _{1.8}	50

List of Figures–Continued

3.30	Field dependence of the nuclear specific heat coefficient for $\text{Pr}_{0.5}\text{Ir}_4\text{Sb}_{10.2}\text{Sn}_{1.8}$	52
3.31	The specific heat over temperature and linear specific heat coefficient versus field for $\text{Pr}_{0.5}\text{Ir}_4\text{Sb}_{10.2}\text{Sn}_{1.8}$	53
3.32	The low temperature resistivity for sample 21.1 of $\text{Pr}_{0.5}\text{Ir}_4\text{Sb}_{10.2}\text{Sn}_{1.8}$	54
3.33	The low temperature resistivity of 5 samples of $\text{Pr}_{0.5}\text{Ir}_4\text{Sb}_{10.2}\text{Sn}_{1.8}$ in a logarithmic temperature scale.....	55
3.34	Superconducting transitions in the magnetoresistance of sample 21.1 of $\text{Pr}_{0.5}\text{Ir}_4\text{Sb}_{10.2}\text{Sn}_{1.8}$	57
3.35	Superconducting transition at 1.8 K (left axis) and corresponding derivative with respect to field (right axis) for sample 21.1 of $\text{Pr}_{0.5}\text{Ir}_4\text{Sb}_{10.2}\text{Sn}_{1.8}$	57
3.36	Superconducting transition at 2 K for sample 64.2 of $\text{Pr}_{0.5}\text{Ir}_4\text{Sb}_{10.2}\text{Sn}_{1.8}$	58

1 INTRODUCTION

1.1 History and Motivation

The mineral “skutterudite” that is composed of CoAs_3 , was originally named for the area of Norway (Skutterud) where it was found. Compounds that share the same crystal structure are now referred to as skutterudites. This structure is similar to the well-studied perovskite family in that they have large voids within the unit cell of the crystal. Large cations can fill these voids and have extreme effects on their properties. The “filled” skutterudite family of materials has played a large part in exploring strongly correlated electron behavior and new quantum states within solids over the last several decades. Much of the initial interest in this family was directed towards their thermoelectric properties and improving the thermoelectric figure of merit, the Seebeck coefficient. This is generally accomplished by adding in a filler ion to the interstitial spaces that are inherent to the skutterudite structure. There has recently been renewed interest into the unfilled skutterudites, as *ab initio* band structure calculations have predicted non-trivial topological states. In particular, recent predictions show IrSb_3 to be a zero-gap topological insulator [1], RhSb_3 to be a new class of zero-gap 3D Dirac semimetal [2], IrBi_3 to be a strong topological insulator [3], and CoSb_3 to be near a topological critical point [4]. These recent bodies of work have given the scientific community a different lens in which to view this system.

The filled skutterudites follow the formula RB_4X_{12} , where R is a lanthanide, actinide, alkali, or alkali earth metal (La, Ce, Pr, Yb, Eu, etc...), B are transition metals (Fe, Os, Ru, Co, Rh, Ir), and X are pnictogen atoms (P, As, Sb). Figure 1.1 shows a unit cell of the filled skutterudite structure. These materials crystalize in an $\text{LaFe}_4\text{P}_{12}$ -type structure with two formula units per unit cell ($\text{Im}\bar{3}$ space group), which includes 8 corner-sharing canted octahedra of BX_6 groups. The octahedra have a distorted shape which has implications for the properties of the materials, as this lowers the point symmetry for the R ions [5]. At the center of this structure is a distorted icosahedral cage that can house R filler ions. The filler ions donate their electrons to the conduction band and become effective positive ions. These filler ions also tend to rattle in their

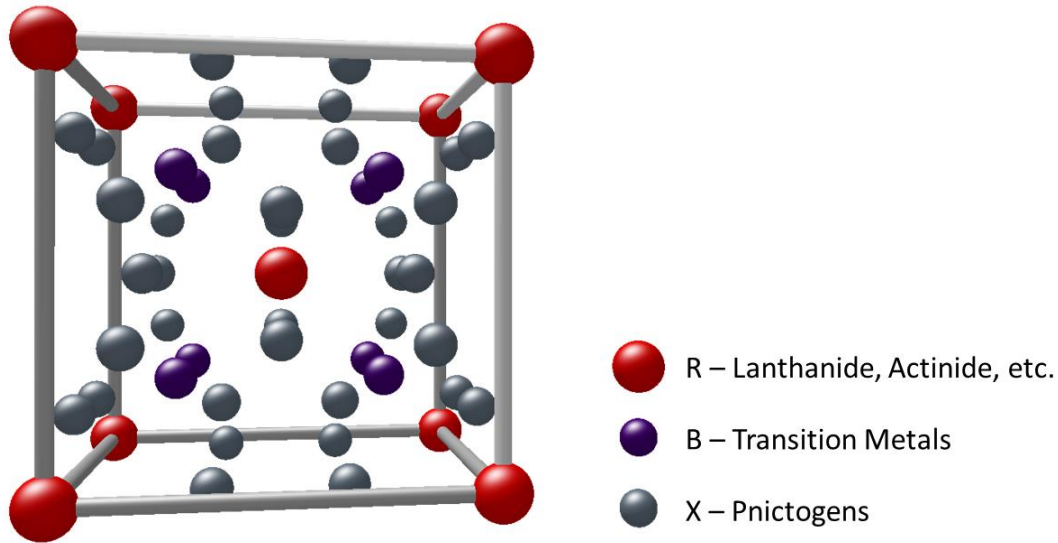


Figure 1.1: Unit cell of the filled skutterudite structure.

oversized cages, creating low energy optical modes. These anharmonic oscillations can scatter phonons, reducing lattice thermal conductivity [6]. This property has brought interest to this family of materials for thermoelectric applications. Poor thermal conductivity paired with good electronic conductivity is necessary to maximize the thermoelectric figure of merit $Z = S^2 \sigma / \kappa$, where S is the Seebeck coefficient, σ is the electric conductivity and κ is thermal conductivity [7]. Skutterudites are one of the most promising thermoelectric materials due to their large figure of merit ($ZT > 1$), the relatively low cost of constituent elements, and their wide range of operating temperatures (300 K to 900 K) [8]. In terms of thermoelectric efficiency, $ZT > 1$ is considered very well performing, as $ZT = 2.6$ is the largest figure of merit reported in a bulk material [9]. Many studies have been undertaken to try and improve this figure through examining the effects of different filler ions within the skutterudite lattice, as well as making substitutions on the other sites to effect the electronic properties [10–14].

This family of materials has also proven to be a workhorse in the development of fundamental condensed matter physics, as they show heavy fermion (HF) states [15–18], antiferro-quadrupolar order [19,20], non-Fermi liquid states [21,22], metal insulator transitions [23,24], topological insulators [25], and BCS [26,27] and exotic [28,29] superconductivity. Due to the rich variety of novel states found, there has been a systematic

investigation into rare-earth based filled skutterudites. Pr based skutterudites in particular have drawn much attention. Until recently, the $4f^2$ configuration of Pr^{3+} ions within intermetallic compounds was thought to be stable, as no strongly correlated behavior was observed in this family of compounds. Most of the rare-earth HF compounds that had been studied were trivalent Ce or Yb systems. PrInAg_2 and $\text{PrFe}_4\text{P}_{12}$ have proven to challenge this thinking, as both compounds show evidence of heavy electron behavior. The correlations in PrInAg_2 are thought to be from coupling between the quadrupole moments of the non-Kramers doublet ground state of the Pr^{3+} ions and conduction electrons [30]. $\text{PrFe}_4\text{P}_{12}$ has a field induced heavy HF Fermi-liquid ground state, which appears upon the suppression of an anti-quadrupolar ordered phase [31]. The anti-quadrupolar ordering is due to a structural phase transition which occurs in the proximity of 7 K; one that lowers the symmetry (due to shifts in the position of Fe), which results in a splitting of the $4f^2$ doublet into eigenstates with quadrupolar degrees of freedom [32].

A recent report by Luo *et al.* [33] has shown that these compounds follow simple Zintl electron counting rules that can predict hundreds of new filled skutterudite compounds. A Zintl phase is formed through an electropositive network of cations that donate electrons to the covalently bonded electronegative anions to complete their outer shell. A prototypical example of a Zintl phase compound within the skutterudite family is CoSb_3 . In this example, the pnictogen Sb rings that make up distorted squares would be the anions, while the transition metal Co make up the cations. Sb in this phase is in a $[\text{Kr}]4d^{10}5s^25p^3$ valence configuration, so each need 3 electrons to fill their p shell. Two of those electrons come from the two covalently bonded Sb ions while the two Co ions donate the third. Thus, at a half electron for each Sb bond, we find Co at a valence of +3. Thus the skutterudite Zintl compound can be written $\text{Co}_4^{3+}(\text{Sb}_4)_3^{4-}$ [34]. This concept can be extended to adding a filler ion into the empty voids of the structure if the valence count is kept close to ideal. By keeping a constant count of 96 (24×4 valence electrons per formula unit), one can make substitutions on the X ion site to create new stable compounds with this structure. In this work, I describe an attempt at filling IrSb_3 with Pr^{3+} ions in a single crystal growth, inspired by the work in Ref. [35] and the interesting properties found in the related material $\text{PrOs}_4\text{Sb}_{12}$.

$\text{PrOs}_4\text{Sb}_{12}$ is the first instance of a Pr based HF superconductor [35]. It shows a double superconducting transition [36] that is in the proximity of a field induced anti-ferroquadrupolar ordered phase [31]. $\text{PrOs}_4\text{Sb}_{12}$ also displays unconventional heavy fermion superconductivity

that is thought to be mediated by quadrupole fluctuations [37]. Zero field muon spin relaxation (μ SR) measurements have shown that $\text{PrOs}_4\text{Sb}_{12}$ breaks time reversal symmetry in its superconducting state as the spontaneous appearance of internal magnetic fields below T_c would suggest [29]. Due to this fact, it is thought to host Majorana Fermionic states, which are highly sought after in pursuit of stable quantum computing systems [38].

The amazing properties found within the Pr and Os based skutterudite created interest in the related compound $\text{Pr}_{0.9}\text{Ir}_4\text{Sb}_{10.2}\text{Sn}_{1.8}$, which was first theorized and synthesized into a stoichiometric powder in Ref. [33]. Some attempts to grow single crystal versions of this material have produced the related compound, $\text{Pr}_{0.5}\text{Ir}_4\text{Sb}_{10.2}\text{Sn}_{1.8}$. From the Zintl counting perspective, a rare earth atom (which donates its electrons and becomes a positive ion) added to the interstitial spaces of IrSb_3 must be compensated by removing electrons from the system. So a partial filling of Pr^{3+} ions in IrSb_3 can become chemically stable by making partial substitutions of Sn on Sb sites. By adding in 3 electrons with a Pr^{3+} ion on the R site, we must also remove 3 electrons from the X site. Thus, $\text{Pr}_{0.6}\text{Ir}_4\text{Sb}_{10.2}\text{Sn}_{1.8}$ would represent the ideal count that is closest to the new material that we synthesized.

This work begins with a characterization of the low temperature properties of high quality single crystal IrSb_3 that was grown in a horizontal self-flux transport approach. Due to much of the interest of this system being in its thermoelectric properties, there has not been a comprehensive look into its properties at extremely low temperatures. Most previous inquiries were carried out on low quality polycrystalline samples. This is in contrast to the large and well formed single crystals used in this study. Initial characterizations through electrical transport suggest non-trivial topological behavior, as well as metallic behavior not before seen in this compound. If confirmed, this system would be added to relatively small list of 3D topological materials. A detailed analysis of its topological nature is however not included in this work, but is planned for future publication.

The remainder of this thesis focuses on the effects of adding Pr^{3+} filler ions into the IrSb_3 structure, with a complete characterization and analysis of $\text{Pr}_{0.5}\text{Ir}_4\text{Sb}_{10.2}\text{Sn}_{1.8}$. Specific heat, electrical transport, and magnetization measurements all support the existence of heavy fermions within this material. Superconductivity is also detected at low temperatures; however, the fraction of material that is superconducting is quite small ($< 1\%$).

1.2 Theoretical Background

1.2.1 Local Moment Physics

1.2.1.1 Heavy Fermions and Magnetic Moment Interactions

In the 1930's a resistance minimum was observed in resistivity measurements of gold, copper, and silver by de Hass et al. [39]. This phenomenon was not explained theoretically for another 30 years. The first microscopic model for local moment formation in metals was established by Anderson in 1961 [40]. The Hamiltonian of the model was built on previous work by Friedel [41] but includes a term that accounts for a Coulomb interaction between d electrons. The Hamiltonian is given by

$$H = H_{0f} + H_{0d} + H_{corr} + H_{sd}, \quad (1.1)$$

where H_{0f} is the unperturbed energy of free-electron states and H_{0d} gives the energy of unperturbed d states of an impurity atom. H_{corr} is the exchange-correlation energy of the repulsive interaction between d electrons and H_{sd} is an s - d interaction term (which is a one-electron energy term).

Jun Kondo in 1964 was able to describe the resistance minimum found in metals with a dilute concentration of magnetic impurity atoms. He employed the s - d exchange model from Zener [42], Kasuya [43], and Yosida [44], which included a key perturbative term in the Hamiltonian that describes an antiferromagnetic interaction between a local moment and conduction electron. This term is given by $H_I = J\vec{\sigma}(0) \cdot \vec{S}$, where J is the super-exchange interaction parameter, $\vec{\sigma}(0)$ is the conduction electron spin density at the origin, and \vec{S} is a spin $\frac{1}{2}$ [45]. The inverse scattering rate (to second born approximation) τ^{-1} of conduction electrons on magnetic localized electrons resulted in

$$\frac{1}{\tau} \propto \left[J\rho + 2(J\rho)^2 \ln \frac{D}{T} \right]^2, \quad (1.2)$$

where D is the electron bandwidth and ρ is the density of states of the conduction electrons. This offers a quantitative explanation of how a minimum in the resistivity is observed; as the

temperature is lowered, the logarithmic term begins to dominate the lattice resistivity. The need for a negative J implies antiferromagnetic coupling is necessary for the Kondo effect to take place.

Localized spin fluctuations can also qualitatively and quantitatively explain the Kondo effect, as the fluctuations become important at low temperatures where $kT_K \ll \tau_0^{-1}$ with τ_0 being the lifetime of the spin fluctuations. A localized spin fluctuation can be thought of as the continuous scattering from electron to hole and back of opposing spins on the impurity site [46]. Below the characteristic temperature T_K , where the thermal energy is of the order of the lifetime of fluctuations ($k_B T_K \sim \hbar/\tau_0$ from the time-energy uncertainty principle), a spin-compensated state forms. This picture is equivalent to a Kondo resonance forming well below the Kondo temperature. Again, this resonance (first introduced by Abrikosov [47], Suhl [48], and Nagaoka [49]) forms as the localized f-electron states of a heavy fermion hybridize with the Bloch waves of the conduction sea [50]. This resonance corresponds to an enhancement of the density of states at the fermi level and the particles in this area show an enhanced effective mass.

The numerical renormalization group concept was required to make further progress, as Kondo's perturbative method breaks down at low energies. With this technique, it was shown that the low temperature properties of a Kondo material are scaled by a characteristic energy

$$T_K \sim D e^{-1/(2J\rho)} \quad (1.3)$$

called the Kondo temperature [50]. The high energy local moment state becomes screened continuously into a Landau-Fermi liquid singlet state as the temperature decreases below T_K .

The screening is primarily from conduction electrons in the neighborhood of the Fermi surface.

1.2.1.2 Kondo Lattice

Within the Kondo impurity regime, the Kondo effect results in magnetic impurities being screened by conduction electrons until they are confined to a singlet state. The effect of this is an increase in the probability of spin-flip scattering at temperatures $O(T_K)$, as the singlet ground state of the impurities act as a scattering center. The resistivity thus increases, as the electron's momentum is not conserved when they scatter. Strangely, the same physical process can result in a metallic state as we move to materials that contain a lattice of magnetic ions within their structure. The Kondo effect develops coherence within a lattice of magnetic ions with

translational symmetry, and the scattering now conserves momentum. This leads to a decrease in resistivity at temperatures below the characteristic Kondo temperature, and ideally, the formation of a Landau-Fermi liquid results [51].

Landau-Fermi liquid theory assumes there is a one-to-one correspondence of non-interacting states with interacting quasiparticle states near the Fermi surface, if the interactions are slowly turned on [52]. The magnetic susceptibility χ and electronic specific heat coefficient $\gamma = C_v / T$ are given by

$$\chi = \frac{\mu_B^2 \rho^*}{1 + F_0^a}, \quad (1.4)$$

$$\gamma = \frac{\pi^2 k_B^2}{3} \rho^*, \quad (1.5)$$

where k_B is the Boltzmann constant, μ_B is the Bohr magneton, and F_0^a is the antisymmetric Landau parameter which measures the spin dependent portion of the quasiparticle interactions. The quasiparticle density of states at the Fermi-level (ϵ_F) is given by

$$\rho^* = \frac{k_F}{\pi^2 \hbar^2} m^*, \quad (1.6)$$

where m^* is the effective mass and k_F is the Fermi wave-vector [50]. The linear specific heat coefficient is proportional to the effective mass of the quasiparticles, which is why these compounds are referred to as “heavy fermions”. The electronic specific heat coefficient γ is greatly enhanced from that of a typical metal; on the order of 100-6000 times that of Cu [53]. At high temperatures, the magnetic susceptibility shows Curie-Weiss behavior which eventually gives way to a constant paramagnetic spin susceptibility at temperatures below T_K . The low temperature resistivity obeys the Landau-Fermi liquid result, $\rho = \rho_0 + AT^2$.

Most HF materials obey two scaling relations: (1) The Kadowaki-Woods ratio $A/\gamma^2 \approx 10^{-5} (\mu\Omega cm)(mol K^2 mJ^{-1})$ was found to be constant for many heavy fermion materials with the parameters varying several orders of magnitude. (2) The Wilson ratio

$$W = \frac{\pi^2 k_B^2}{\mu_B^2} \frac{\chi}{\gamma} \approx 2, \quad (1.7)$$

was also found to be nearly constant with large variations in the values of χ and γ [50]. It can be seen from the Landau-Fermi liquid expressions for those quantities that the renormalized density of states is common to both terms and factors out of the Wilson ratio. This relation allows one to perceive HF materials as a Landau-Fermi liquid with a large effective mass (renormalized density of states) that originates from a coherent lattice Kondo effect [51].

The coupling term J found in the Kondo Hamiltonian is also responsible for an interaction that competes with the Kondo effect for a different ground state. The RKKY interaction is named after those who first considered it: Ruderman & Kittel [54], Kasuya [43], and Yosida [44]. This interaction allows for spin-exchange between local moments and is mediated by conduction electrons scattering between magnetic sites. The long-range exchange of the RKKY interaction causes local moments to order. Doniach was the first to realize that if the RKKY coupling energy becomes greater than the energy scale set by T_K , then Kondo spin screening would be overtaken by magnetic order [55]. Therefore, depending on the strength of each interaction, a magnetic or nonmagnetic ground state can be realized at low temperatures.

2 METHODS

2.1 Crystal Growth

2.1.1 IrSb₃ Horizontal Flux Transport

Single crystals of IrSb₃ were grown in a horizontal configuration by way of flux transport [56]. Rather than slowly cooling the ampoule, as is done in a vertical configuration, it is held within a heat gradient. Generally, the highest temperature is set at the base of the tube where the constituent materials have been loaded and decreases outwards. The flux within the ampoule will melt and fill the bottom of the tube and the other raw material(s) will slowly transport to the cold end because of the composition/heat gradient. Nucleation will occur at the point where the concentration of dissolved metal within the flux (Ir in this case) reaches its solubility limit for the desired phase. A horizontal configuration also allows for larger yields of IrSb₃ than a vertical growth, as there are limitations on the concentration of allowed Ir within the flux (~ 3 %) to produce the correct phase [56].

The starting raw materials were composed of 0.5 g of Ir (powder, 4N) and 16.67 g of Sb (shot, 5N), and were loaded into a 5” quartz ampoule with the Ir powder on the very bottom. This ampoule was then evacuated and filled with 500 *mTorr* of argon gas before being sealed by way of hydrogen-oxygen torch. The end of the tube where the Ir sits was placed at the center of a tube furnace, as shown in Fig. 2.1. The temperature of the heating filament in the center is set to 860 degrees C. The furnace was held at this temperature for 3 weeks to allow plenty of time for crystal growth to occur. The heating element was then turned off and the growth was allowed to cool to room temperature before being opened. A large ingot of mostly Sb flux was removed and large IrSb₃ crystals were found on the extreme cold end of the tube, as seen in Fig. 2.2. This ingot was reheated to approximately 700 degrees C for 3 hours in a new quartz ampoule with a built in sieve made of quartz wool. The ampoule is then removed at that temperature and immediately place into a centrifuge at ~1500 rpm to separate the liquid flux from the solid

crystals. Crystals from this method ranged in size and morphology as there was a fairly large area where crystal growth occurred. Figure 2.3 shows the largest of the single crystals from the batch. Smaller crystals that were close to perfect rectangular prisms were used for most measurements.

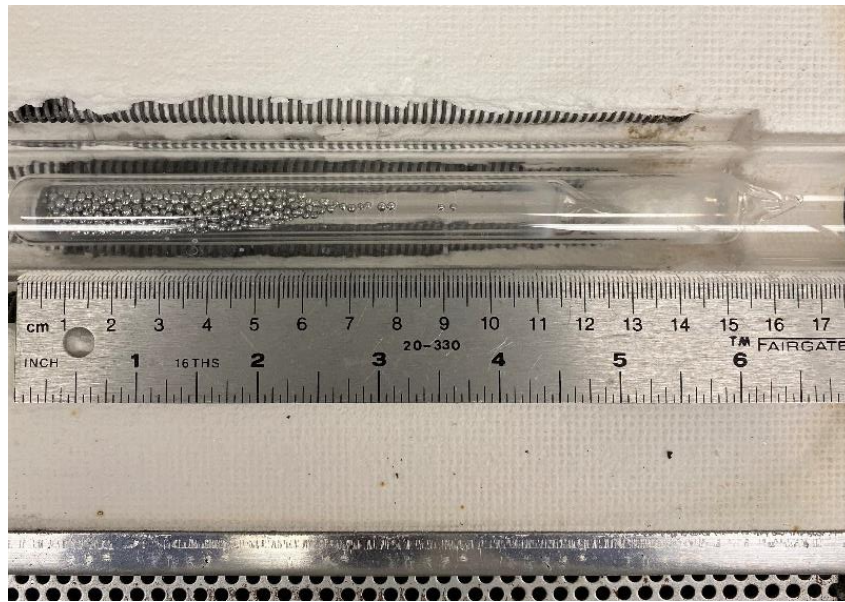


Figure 2.1: Horizontal flux transport growth of IrSb_3 .



Figure 2.2: Horizontal growth of IrSb_3 when first removed from furnace.



Figure 2.3: Largest single crystal IrSb_3 samples. (Smallest division of squares ~ 1 mm).

2.1.2 $\text{Pr}_{0.5}\text{Ir}_4\text{Sb}_{10.2}\text{Sn}_{1.8}$ Flux Growth

The process for growing single crystals of the praseodymium-based skutterudites was based on the method reported by Bauer et al. in Ref. [28] as well as Ref. [57]. For $\text{Pr}_{0.5}\text{Ir}_4\text{Sb}_{10.2}\text{Sn}_{1.8}$, the starting materials consisted of praseodymium (ingot, 3N), iridium (powder, 4N), antimony (shot, 5N) and tin (shot, 4N). The ratio in which they were initially weighed (atomic ratios 1:4:13.33:6.66) was initially chosen to attempt to grow $\text{PrIr}_4\text{Sb}_8\text{Sn}_4$. This was based upon the atomic ratio that $\text{PrOs}_4\text{Sb}_{12}$ is grown with when using the self-flux method (1:4:20). The flux method of single crystal growth allows for metals with a high melting temperature (Pr, Ir) to dissolve into a liquid metallic flux (Sb) at a temperature lower than their respective melting temperatures. As the temperature of the solution is slowly decreased, single crystals form of the desired material.

The high temperature growth is performed within a carbon coated quartz ampoule, as Sb and Pr both react with SiO_2 , effectively destroying the ampoule at high temperatures. The ampoule is coated in carbon through pyrolysis of acetone. The quartz ampoule is filled to an approximate height of 3 cm with acetone and sealed with Kimtech Kimwipes that have been rolled into a cone shape. The Kimwipes act as a plug to keep in acetone vapor and soak up excess acetone liquid. After letting the liquid coat the surfaces of the ampoule, it should be turned horizontally to allow the liquid to absorb into the Kimwipe. Any boiling acetone will not

allow the carbon to adhere well to the surface and will destroy any previous coating. It is recommended that no additional acetone be added once the process has begun, as sudden changes in temperature can also cause the carbon to break from the surface. A hydrogen-oxygen torch is then used at a very low oxygen setting to heat the end of the ampoule where the starting materials will sit. The temperature needs to be high enough to see a bright orange glow (when pyrolysis occurs), but not too high as to soften the quartz. A sufficient coating is achieved when the carbon layer blocks most of the incoming light through the tubes bottom. The main importance is that the area of the ampoule which is in direct contact with the growth solution is completely covered, as the vapors present do not seem to break down the bare quartz.

The praseodymium ingots readily react with oxygen and form a green film due to the corrosion on the exterior. They were thus were handled and cut within an inert atmosphere in a glove box. The surface layers of the ingot were removed prior to use to ensure no oxidation was included in the growth. Half of the antimony and tin shot were the first to be loaded into the end of a large diameter open quartz ampoule that had been previously carbon coated. The iridium powder was then loaded into a smaller ampoule with a weighing paper slid into the end to prevent powder from sticking to the interior. This smaller ampoule is then slid into the larger carbon-coated ampoule and turned vertically so the iridium powder reaches the bottom without adhering to the sides. Next the small chunks of Pr ingot were loaded into the ampoule with the remaining Sb/Sn on top. This ampoule is then evacuated of air and refilled with argon multiple times to ensure there is no oxygen present. The final pressure of the argon gas within the tube is approximately 500 mTorr . The ampoule is then sealed with a hydrogen-oxygen torch by hand in the typical manner.

The temperature range used for growth can be deduced through previous literature on similar materials or through temperature-composition phase diagrams. In this case, $\text{PrOs}_4\text{Sb}_{12}$ was the closest match, so similar growth parameters were used as in Ref. [58]. Temperature-composition phase diagrams are also important to consider to avoid the accidental growth of undesired compounds. It is standard practice to consider other materials which may result from particular growth parameters. The temperature is first set to reach and sit at 650°C to allow the Sb flux to melt completely for a few hours, then the temperature is ramped to 950°C . After resting at this temperature for 72 hours, a cooling rate of $1^\circ \text{C} / \text{hr}$ is used to return back to 650°C .

To remove the remaining flux, the ampoule is inserted into a centrifuge at $650^{\circ}C$ and quartz wool inside of the ampoule acts as a filter to separate the crystals from the molten antimony/tin solution. The surfaces of the crystals are then cleaned using a dilute aqua regia solution (2:3:1 \rightarrow H₂O: HCl [37% concentration]: HNO₃ [70% concentration]) that is able to dissolve excess antimony/tin in a short period of time. The single crystals are only kept in the solution for 10-15 minutes at a time and are subsequently checked under an optical microscope. The crystals generally formed in clusters of cubes with well-formed facets up to 1 mm in length. In subsequent growth attempts, the cooling rate was lowered to $0.6^{\circ}C/hr$ and larger facets of up to 2 mm were found.

2.2 Structure and Composition

2.2.1 Powder X-ray Diffraction

Powder X-ray Diffraction (PXRD) measurements were taken to help identify the structure, relative composition, as well as any impurity phase present. The measurements were taken with a PANalytical Empyrean X-ray Diffractometer that uses CuK_{α} x-rays with a wavelength of 1.5406 \AA . To get the most accurate diffraction pattern a “perfect powder” is desirable; one in which all scattering planes are equally represented. Thus, it was necessary to use a granite mortar and pestle to grind the single crystal pieces for at least 10 minutes into a fine powder. This powder was then loaded onto a low background single crystal silicon sample holder with a small depression as to avoid the use of any adherent that would add to the background. If the material did not entirely fill this area then the sample holder was flipped over to a flat side and coated with an extremely small amount of low background grease for the powder to adhere to. The materials were all measured in a goniometer scan from $5^{\circ} \leq 2\theta \leq 90^{\circ}$ in 0.008 degree steps while spinning 4 times per second. A spinning platform is especially advantageous when doing measurements on a small amount of powder, as it ensures more crystal planes are equally represented.

Analysis of PXRD data was done using the PANalytical X'Pert Highscore proprietary software suite that is integrated with the diffractometer [59]. The crystal structures and their respective diffraction patterns were simulated by inputting the constituent atoms, the space group

of the crystal, the Wyckoff positions of the atoms, and their expected occupancy fraction. For materials that have not been previously grown or analyzed, the exact Wyckoff positions can be estimated by the positions of related materials with similar constituent atoms. For example, the positions of Ir and Sb/Sn in $Pr_{0.5}Ir_4Sb_{10.2}Sn_{1.8}$ were estimated from the positions of Ir and Sb/Sn within $La_{0.9}Ir_4Sb_{10.2}Sn_{1.8}$ [33]. To get an estimate of the lattice constant of our materials we performed Rietveld refinement using the Highscore software suite [60]. The Pr, Sb, and Sn occupancy fractions for $Pr_{0.5}Ir_4Sb_{10.2}Sn_{1.8}$ (which has fractional filling) were tentatively refined and found to be fairly consistent with our estimates from energy dispersive x-ray spectroscopy measurements (EDS), giving more confidence in the results. The isotropic Debye-Waller coefficient B_{iso} was also refined for the Pr^{3+} ions, as Pr ions within skutterudite materials have been shown to vibrate within their icosahedral cages (which results in a large B_{iso} value), throwing off expected intensities of the diffraction pattern peaks. The accuracy of this refined value should be met with caution though, as single crystal x-ray diffraction is the preferred method. This coefficient can be calculated through the relation between B_{iso} and θ_E given by

$$\frac{B_{iso}}{8\pi^2} = \langle u^2 \rangle = \frac{\hbar^2}{2mk_B\theta_E} \coth\left(\frac{\theta_E}{2T}\right), \quad (2.1)$$

where B_{iso} is the isotropic Debye-Waller factor, $\langle u^2 \rangle$ is the average mean square atomic displacement amplitude, \hbar is Planck's constant, m is the mass of the oscillating atom, and θ_E is the Einstein temperature of the oscillating ion. This relation also allows for a check on the fits to the specific heat data for $Pr_{0.5}Ir_4Sb_{10.2}Sn_{1.8}$, which will be discussed further below.

2.2.2 Energy Dispersive X-ray Spectroscopy

Energy dispersive X-ray spectroscopy (EDS) measurements were performed on small single crystal samples to determine the relative composition of our grown materials. Pr filling fraction was of particular interest and this technique proved to be quite useful in this manner. All EDS measurements were taken using a JOEL-JSM-IT100LA scanning electron microscope. The accelerating voltage was set to 15 kV for all measurements. The relative compositions of the

grown materials were determined by selecting multiple randomly selected flat areas and averaging those values together.

2.3 Physical Properties

2.3.1 Resistivity

Electrical resistivity ρ measurements were taken using the Quantum Design Physical Property Measurement System (PPMS) Electronic Transport Option (ETO) at WMU. The tunable parameters for resistivity measurements are temperature (300 K to 1.7 K) and magnetic field ($-14 T \leq H \leq 14 T$). The dilution refrigeration option for the PPMS was used in measurements for temperatures $0.05 K \leq T \leq 4 K$. Samples were measured using the standard 4-wire geometry with AC currents ranging from 1-10 mA while a smaller current of 0.25 mA was used for dilution refrigerator measurements. Figure 2.4 shows an example of two samples of IrSb₃ that are wired to a PPMS rotator puck for the electronic transport measurements. The rotator option allows for angular dependent resistivity measurements in a magnetic field.

The samples that were chosen for measurement had smooth and large facets that made wiring less difficult of a procedure. Samples that had a cubic or rectangular prismatic shape were preferred, as close alignment of the crystal planes and voltage leads with respect to a magnetic field is necessary for precise magnetoresistance/hall measurements. Estimating the exact dimensions of the crystals is necessary to calculate an accurate absolute value for resistivity and symmetric samples tend to simplify that task. The surfaces of our single crystals were cleaned with acetone in a sonic bath after being thoroughly etched in dilute aqua regia solution. To get low contact resistance, we sputtered the surface with evaporated gold to create 4 leads where wires can be connected. This is done by first masking off the crystal with the legendary GE varnish in a striped pattern on the top of the crystal. This process required the proper consistency of varnish as it would often dry too quickly and become difficult to manipulate. Toluene can be added to GE varnish as a thinning agent and is recommended before each new masking attempt, as it quickly evaporates. Once the varnish had effectively dried on the samples, they were placed into a Cressington sputter coater for approximately 5 minutes with a current of 25 mA. Dotite

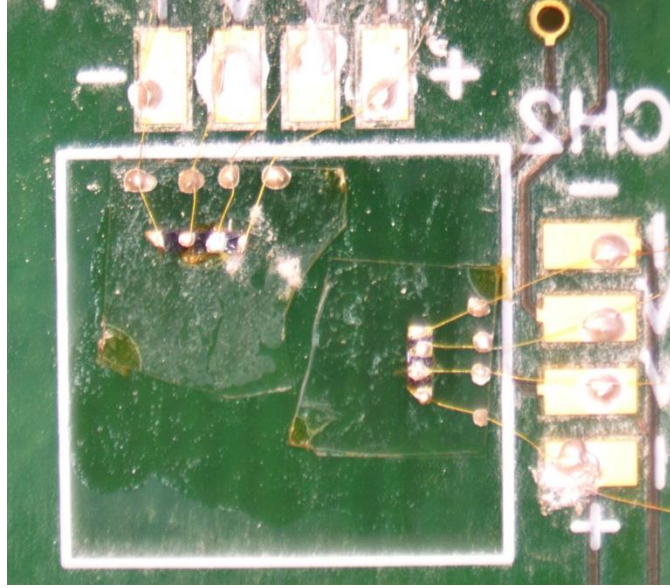


Figure 2.4: IrSb₃ single crystals wired for resistivity measurements.

silver epoxy was then used to attach the gold wires to the surface of the samples after cleaning off the masking. This epoxy had to be cured at 150° C for at least an hour.

Low temperature resistivity data was theoretically fit to gain insight on the Kondo behavior found in Pr filled samples, search for a superconducting transition as well as check for Fermi/Non-Fermi liquid behavior. All data was fit with the assumption that Matthiessen’s rule is valid and the separate contributions to the total resistivity are a simple sum. The low temperature resistivity of most metals can be well described by

$$\rho = \rho_0 + AT^2 + BT^5 . \quad (2.2)$$

The symbol ρ_0 represents the contribution from electrons scattering on impurities or defects within the crystal. This contribution is generally temperature independent and can be estimated by the resistivity at $T = 0 K$. This value is generally found using an extrapolation that results from a fit to the form above for the low temperature resistivity. This value also becomes useful as it allows one to characterize the “quality” of a crystal growth. The residual resistivity ratio is typically defined as

$$RRR = \frac{\rho(T = 300 K)}{\rho(T = 0 K)} , \quad (2.3)$$

where a large RRR is often indicative of a pure sample (depending on the material) [61]. The following term that is linear in T^2 is derived from Landau Fermi-liquid theory and accounts for electron-electron scattering [62]. The next term which is proportional to T^5 is due to electron-phonon scattering and was first introduced by Bloch [63]. The materials that show enhanced effective mass have a significant T^2 contribution at low temperatures, such that the electron-phonon Bloch term is not included in the low temperature fits.

2.3.2 Magnetization

DC magnetization measurements were taken using the Quantum Design PPMS Vibrating Sample Magnetometer (VSM) Option at WMU. Measurements were taken for $1.7 K \leq T \leq 300 K$ in magnetic fields $-14 T \leq \mu_0 H \leq 14 T$. The samples are typically mounted on a low-background quartz paddle using a small amount of GE varnish to secure the sample, as is shown in Fig. 2.5. Using this method made the process of aligning the samples fairly simple, as the facets of the cubic crystals were oriented to be parallel to the sides of the paddle. The small background from the glue and paddle can be disregarded when compared to the size of the signals measured.

The VSM option operates under the principle of Faraday's law of induction. A motor that sits atop the PPMS chamber is able to vibrate the sample's position in a sinusoidal motion at a set frequency. If a sample has a net magnetic moment then the changing magnetic flux from the motion of the sample will induce a time dependent voltage in the pickup coil such that

$$V_{out} = -\frac{d\Phi}{dt} = -\frac{d\Phi}{dz} \frac{dz}{dt}, \quad (2.4)$$

where Φ is the magnetic flux through the coil, z is the vertical position of the sample in the sample chamber with respect to the coil, and t is time. If the vertical position of the sample is oscillating in a sinusoidal manner then $z = A \cos(2\pi ft)$, where A is the amplitude of oscillation and f is the frequency of oscillation. After taking the time derivative,

$$\frac{dz}{dt} = -2\pi fA \sin(2\pi ft) \quad (2.5)$$

and the final expression becomes

$$V_{out} = 2\pi fCmA \sin(2\pi ft), \quad (2.6)$$

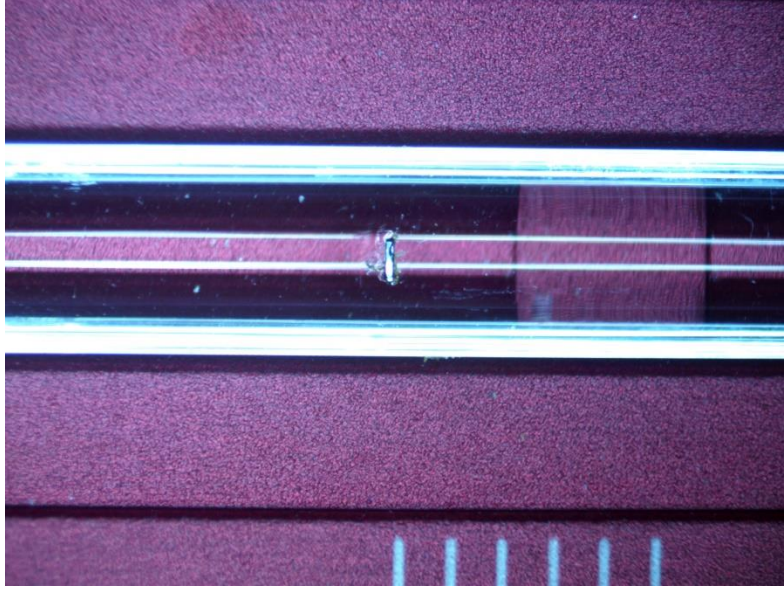


Figure 2.5: Small IrSb₃ single crystal mounted on quartz rod for magnetization.

where C is a coupling constant and m is the DC magnetic moment of the sample [64]. The PPMS VSM unit is able to determine this coupling constant and measure the corresponding magnetic moment. The total moment m (emu) is then converted to magnetization M (emu/mol) by multiplying by the molecular mass of the sample (g/mol) and then dividing by the mass of the sample. With knowledge of the magnetization M and the corresponding magnetic field H , one is able to calculate the (DC) molar magnetic susceptibility χ_m (cm^3/mol). The molar magnetic susceptibility for a magnetic material can be fit with the Curie-Weiss expression

$$\chi = \chi_0 + \frac{C}{T - \theta_w}, \quad (2.7)$$

where C is the Curie constant, T is the temperature, and θ_w is the Curie-Weiss temperature [65,66]. From this one is able to deduce the effective magnetic moment μ_{eff} through the relation $C = p^2 \mu_B^2 N_A / 3k_B = \mu_{\text{eff}}^2 N_A / 3k_B$, where N_A is Avogadro's number, k_B is the Boltzmann constant, μ_B is the Bohr magneton, and p is the effective number of Bohr magnetons. The Curie-Weiss temperature indicates ferromagnetic or antiferromagnetic correlations, depending if it is positive or negative, respectively.

2.3.3 Specific Heat

Specific heat measurements were taken using the PPMS Heat Capacity option for temperatures $1.7\text{ K} \leq T \leq 300\text{ K}$ in magnetic fields up to 14 Tesla. The PPMS Dilution Refrigerator option is able to extend the temperature range of specific heat measurements with working temperatures $0.05\text{ K} \leq T \leq 4\text{ K}$ in fields up to 14 Tesla. The measurements are taken using relaxation calorimetry, where a known amount of heat is added to a sample for a fixed time and then is allowed a cooling period of the same time. The temperature is monitored carefully with accurate time resolution to be able to deduce the characteristic time constant τ which is proportional to the specific heat of the sample at that temperature. The PPMS software can also employ a “Two-Tau” model that is able to account for poor thermal coupling between the sample and sample platform [67]. To achieve good thermal contact with the sample platform, single crystals with well-formed facets that were mostly free of defects were preferred. A small amount of Apiezon N-grease is applied to the sample platform prior to measurement to ensure good thermal coupling. Figure 2.6 shows an IrSb₃ crystal that has been mounted on the specific heat sample platform. The background contribution to the specific heat, which consists of the sample holder and N-grease, is also measured before mounting the sample so it can be reliably subtracted. Field dependence of the background was also considered when necessary, usually for samples with a relatively small signal.

The specific heat data for the filled skutterudite was analyzed in multiple different ways (at different temperature ranges) to analyze the heavy fermion behavior and characterize the material. The high temperature data for the filled skutterudites are reminiscent of a typical metal that is described well by the Debye model. The fit for the high temperature specific heat takes the form

$$C(T) = 9Nk_B \left(\frac{T}{\theta_H} \right)^3 \int_0^{\theta_H/T} dx \frac{x^4 e^x}{(e^x - 1)^2}, \quad (2.8)$$

where θ_H is the Debye temperature and $x = \theta_H/T$ [68]. Fits of this type allow for the extraction of the Debye temperature that can then be compared with more complex models at the lower temperatures.

The low temperature specific heat data for the filled skutterudites usually consists of multiple terms in order to be properly described. In general, the specific heat can be modeled



Figure 2.6: IrSb₃ single crystal mounted on sample platform of PPMS specific heat option.

with an electronic contribution and lattice contribution, such that $C(T) = C_e + C_l$. The low temperature electronic specific heat is linear in T , such that $C_e = \gamma T$ where γ is the Sommerfeld coefficient. This coefficient is useful in characterizing heavy fermion behavior, as an enhanced value is indicative of strong electron correlations. The lattice specific heat is usually dominated by phonon degrees of freedom, which takes the form $C_l = BT^3$ in the low temperature realm. The Debye temperature can then be extracted through the relation

$$B = \frac{12\pi^4}{5} \frac{nN_A k_B}{\theta_L^3}, \quad (2.9)$$

where n is the number of atoms per formula unit and θ_L is the Debye temperature from the low temperature fit. In the case of the Pr filled skutterudites, an Einstein mode is included in the lattice term. Einstein modes have been previously found in several different filled skutterudite systems [69]. These atoms have varying Einstein temperatures depending on the constituent atoms and the available space within the lattice. The Debye lattice term must be modulated such that the Pr contribution is removed and replaced with an Einstein term. This is done by considering an additional parameter x such that the lattice term becomes

$$C_l = (n-x) \frac{12\pi^4}{5} \frac{N_A k_B}{\theta_L^3} + (x) \frac{3R(\theta_E/T)^2 \exp(\theta_E/T)}{(\exp(\theta_E/T) - 1)^2}, \quad (2.10)$$

where R is the gas constant and θ_E is the corresponding Einstein temperature of the participating Pr ions.

An additional analysis was performed on the extremely low temperature ($T < 0.5$ K) specific heat for $\text{Pr}_{0.5}\text{Ir}_4\text{Sb}_{10.2}\text{Sn}_{1.8}$, as there is a large nuclear Schottky peak present below 0.25 K which dominates the other contributions. This large upturn in the specific heat is a result of hyperfine coupling within the nuclear degrees of freedom of the system. Following Ref. [31], the fit for the specific heat in this temperature range takes the form

$$C(T) = \frac{A_N}{T^2} + \gamma_n T + BT^n. \quad (2.11)$$

This form is chosen to allow a clean subtraction of all contributions that are not related to the nuclear Schottky peak, which allows one to calculate an accurate value for A_N . It will be shown in the discussion that this value allows for a qualitative look at the site averaged magnitude of the Pr moments due to intrasite hyperfine coupling at these extremely low temperatures.

3 ANALYSIS AND DISCUSSION

3.1 IrSb₃

3.1.1 Composition

A typical graph of EDS measurements for IrSb₃ is shown in Fig. 3.1. Multiple points were measured over random areas of clean surface. Figure 3.2 shows an example SEM image of the surface of sample 73.1 that was used for measurement. The rough-looking material is silver epoxy from previous transport measurements. The relative composition from these measurements were averaged together for each sample. All samples were determined to be within 1% of the expected ratio of Ir to Sb (1:3 atomic ratio). Table 1 shows the results of two of the measured samples with their respective error. Out of five samples measured, only 1 was found to have slightly excess Ir. Interestingly, this sample (73.1) also shows transport behavior of a good metal ($RRR \approx 40$). Unfortunately, it is difficult to be sure of the accuracy of the results because the estimated error (based upon the standard deviation of the measurements) is nearly as large as the discrepancy from a perfect material.

Table 1
Relative Composition of IrSb₃ from EDS Measurements.

Sample	%Ir	%Sb
73.1	25.11(6)	74.89(6)
73.2	24.46(37)	75.54(37)

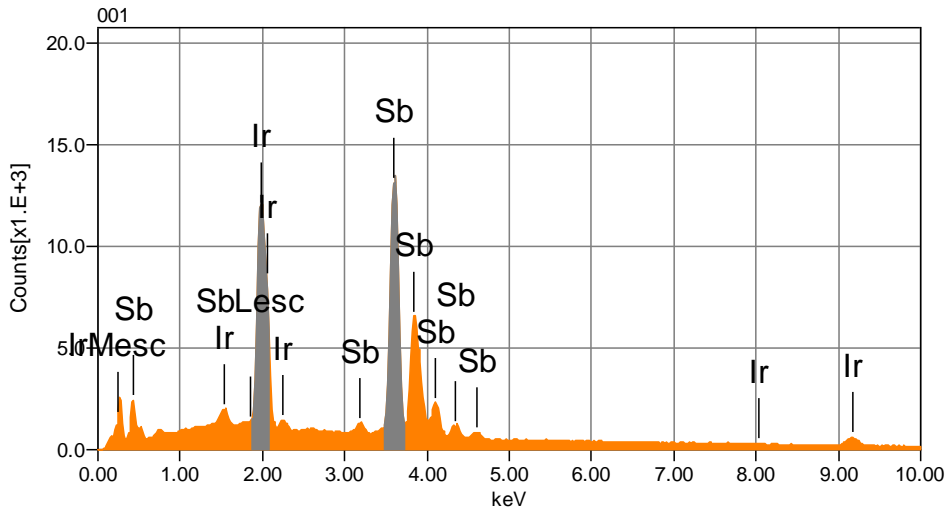


Figure 3.1: EDS graph for IrSb₃ showing peaks attributed to each element.

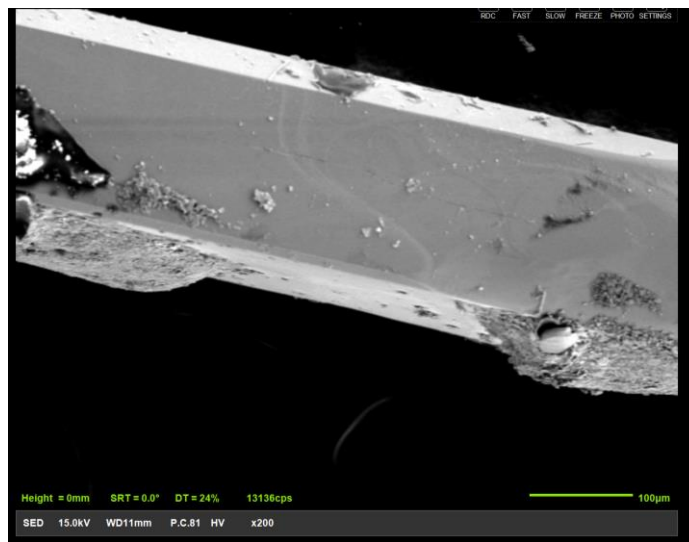


Figure 3.2: SEM picture of sample 73.1 of single crystal IrSb₃.

3.1.2 Magnetization

The molar magnetic susceptibility versus temperature graph is shown in Fig. 3.3 for a field strength of $0.1 T$. This material displays temperature independent diamagnetism, as is expected from a non-magnetic metal without unpaired electrons [70]. Diamagnetism is a result of the orbital motion of electrons in response to an applied magnetic field and has no connection to

the intrinsic spin of electrons. There is a hint of a low temperature Curie upturn that is likely from a small amount of impurity spins [33]. We will see in the discussion below that filling IrSb₃ with a rare-earth ion (Pr³⁺) that has an unfilled *f*-shell will result in a drastic change to the magnetic susceptibility.

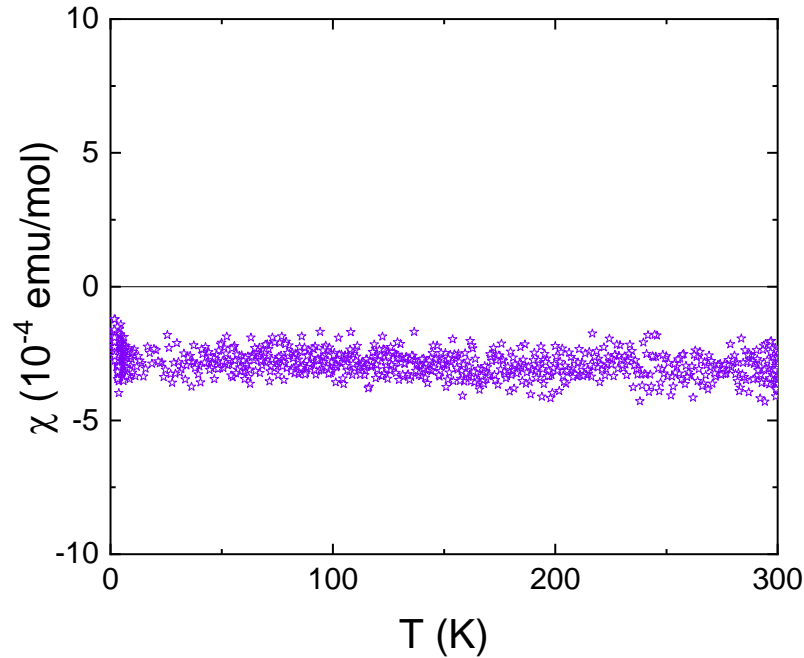


Figure 3.3: The temperature independent magnetic susceptibility of single crystal IrSb₃.

3.1.3 Specific Heat

The high temperature fit to the specific heat is shown in Fig. 3.4 for $2 \leq T \leq 200 \text{ K}$. The Debye model given in equation 2.8 produces a satisfactory fit to the entire temperature range, with Debye temperature $\theta_H = 282(2) \text{ K}$. Figure 3.5 shows the low temperature fit to the specific heat of the form $C/T = \gamma + BT^2$, where γ is the electronic coefficient and $B = 1944n / \theta_L^3$. A fit of this type in the temperature range $3 \text{ K}^2 \leq T^2 \leq 40 \text{ K}^2$ gives an extremely small $\gamma = 0.019(4) \text{ mJ} / \text{mol K}^2$, which is approximately 3 orders of magnitude smaller than the filled counterpart Pr_{0.5}Ir₄Sb_{10.2}Sn_{1.8}. The density of states effective mass in a single parabolic band model can be calculated through the relation $m^* = (3\hbar^2 / k_F k_B^2 V_0) \gamma$, where V_0 is the volume of the compound per unit mole and $k_F = (3\pi n_H)^{1/3}$ [71]. The Fermi wave number is estimated through

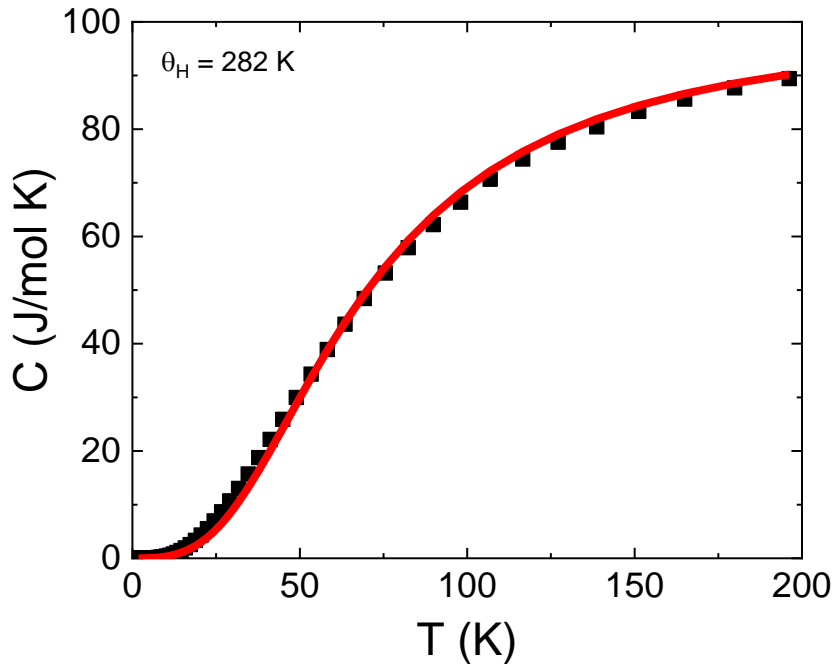


Figure 3.4: High temperature specific heat of IrSb_3 .

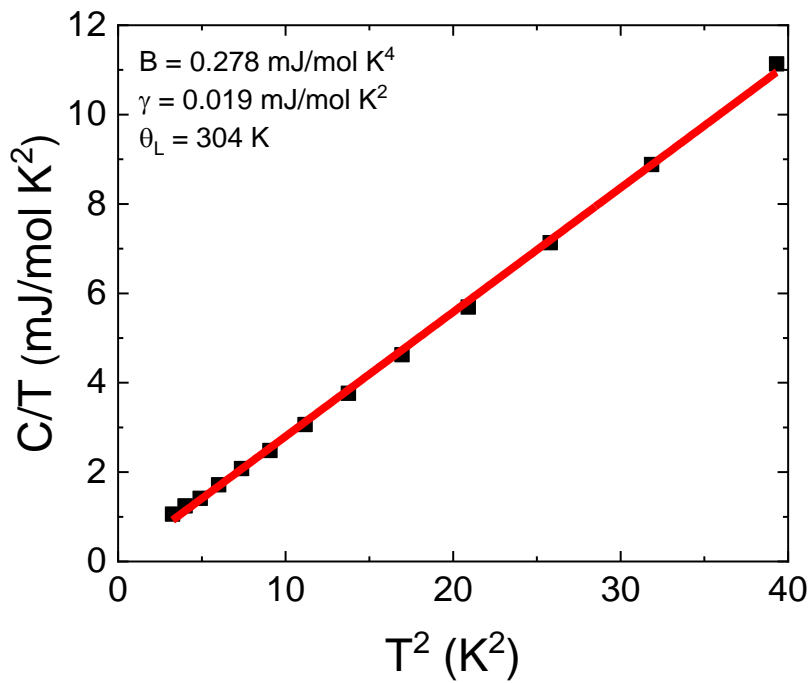


Figure 3.5: Low temperature specific heat divided by temperature versus temperature squared of IrSb_3 .

the carrier concentration as determined by Hall measurements, $n_H = 3.9 \times 10^{18} \text{ cm}^{-3}$. The result of this calculation is $m^* = 0.17m_0$, where m_0 is the value of the mass of a free electron. This is not far from the small value of m^* that was predicted in Ref. [72]. The Debye temperature determined from the slope of the graph B is given by $\theta_L = 304(3) \text{ K}$. Ab initio calculations of an IrSb₃ supercell with 128 atoms produced a remarkably close Debye temperature of $\theta_w = 303 \text{ K}$ [73]. Our measurement is also consistent with previous experimental values ($\theta_L = 305 \text{ K}$), such as in Ref. [71,74]. We shall see in the next section that the partial filling of Pr ions in this material induces a large change in electron correlations and lattice dynamics, as is shown through specific heat and resistivity measurements.

3.1.4 Resistivity

3.1.4.1 Longitudinal Resistivity

Previous studies on the low temperature resistivity of IrSb₃ show an insulating upturn in the resistivity at lower temperatures [75,76]. It should be noted that these studies were done on polycrystalline samples that were grown in a stoichiometric ratio. This is consistent with some *ab initio* calculations that predict a full bandgap across the high symmetry lines of the first Brillion zone [77]. However, other calculations have claimed IrSb₃ to be a point Fermi surface zero-gap semiconductor and noted the quasilinear dispersion of the gap-crossing band at small wave vector values near the Γ point [78,79]. Surprisingly, through a careful horizontal flux transport growth of this material, drastically different behavior from previous experimental reports has been observed in the transport properties. These properties also confirm the theoretical predictions that this material can behave semi-metallically. Figure 3.6 shows the normalized resistivity trends of several samples all grown within the same batch where ρ_0 corresponds to the value of the resistivity at 300 K. One of the samples (73.0) shows the traditional semiconducting behavior with a much larger absolute value of the resistivity. Sample 73.1 shows quite the opposite behavior with the resistivity trend of a decent metal with very low residual resistivity and a residual resistivity ratio $RRR = 40.4$. Sample 73.2 also demonstrates metallic behavior but has a larger absolute value of the resistivity and a much lower RRR of about 1.7 and a different functional dependence on temperature.

The large discrepancy in resistive behavior is likely due to a compositional gradient resulting from the horizontal growth technique and the atomic vacancies or inclusions that result. As the flux (Sb in this case) melts in the ampoule, Ir will start to transport from the hot end of the tube to the cool end. Somewhere along that path, the concentration of Ir reaches the solubility limit of the desired material and begins to crystallize. As the nucleation site grows, the point in the temperature gradient where the solubility limit was reached is no longer accessible. Thus, the growth has to occur at a different temperatures and local relative compositions as time goes on and as starting material is used up. This could easily result in an excess or lack of a stoichiometric amounts of Ir within the crystal structure. Large variance in transport behavior from crystals in the same batch has been observed in Dirac semimetal Cd_3As_2 , with properties varying up to a factor of 200 [80]. Similarly, the topological insulator $\text{Bi}_2\text{Te}_2\text{Se}$ and related compounds doped with Sb have been found to be both insulating and metallic in the bulk [81]. This has largely been attributed to Se/Te vacancies or defects within the material that change the carrier concentration and effectively shift the Fermi level in accordance. It is likely that much of the variance in behavior seen in single crystal IrSb_3 can be attributed to Sb vacancies in the lattice or in some cases excess Sb found in interstitial sites. It should be noted that each sample

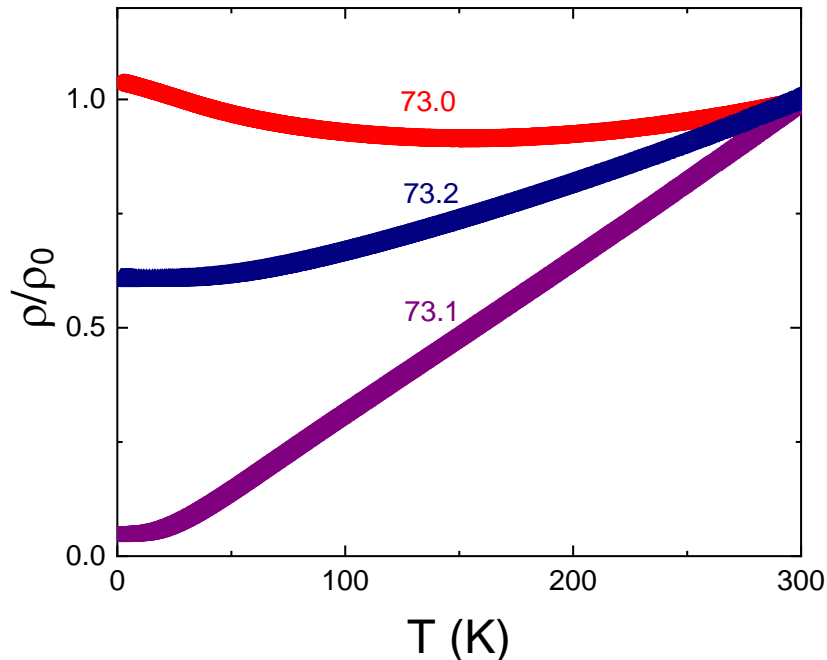


Figure 3.6: Normalized temperature dependence of the resistivity of three samples of IrSb_3 .

has a slightly different size and morphology, so the current density is not constant between measurements. As sample 73.0 represents a more prototypical IrSb₃ sample, that analysis is presented first.

An Arrhenius plot of the resistivity data for sample 73.0 displayed in Fig. 3.7 is linear in the limited temperature range of $70\text{ K} \leq T \leq 125\text{ K}$. The activation energy Δ required for conduction can be extracted from the slope of the best fit line to the $\ln(\rho)$ vs T^{-1} plot, as the Arrhenius equation is given by $\rho = \rho_1 \exp(\Delta/k_B T)$, where ρ_1 is the pre-exponential factor [82]. This form for the resistivity however, does not fit well to the lower temperature range, as there seems to be a crossover in conduction mechanism as the temperature is lowered. Similar crossover behavior has been observed in fellow skutterudite CoSb₃ [83], as well as three-dimensional topological insulator Bi_{1.5}Sb_{0.5}Te_{1.7}Se_{1.3} [82]. As a result, the resistivity for $38\text{ K} \leq T \leq 100\text{ K}$ has been fit to the 3D Mott variable range hopping (VRH) equation given by $\rho = \rho_0 \exp(T_0/T)^{1/4}$, with T_0 representing the localization temperature. The localization temperature is inversely proportional to the density of states at the Fermi level $N(E_F)$ and is

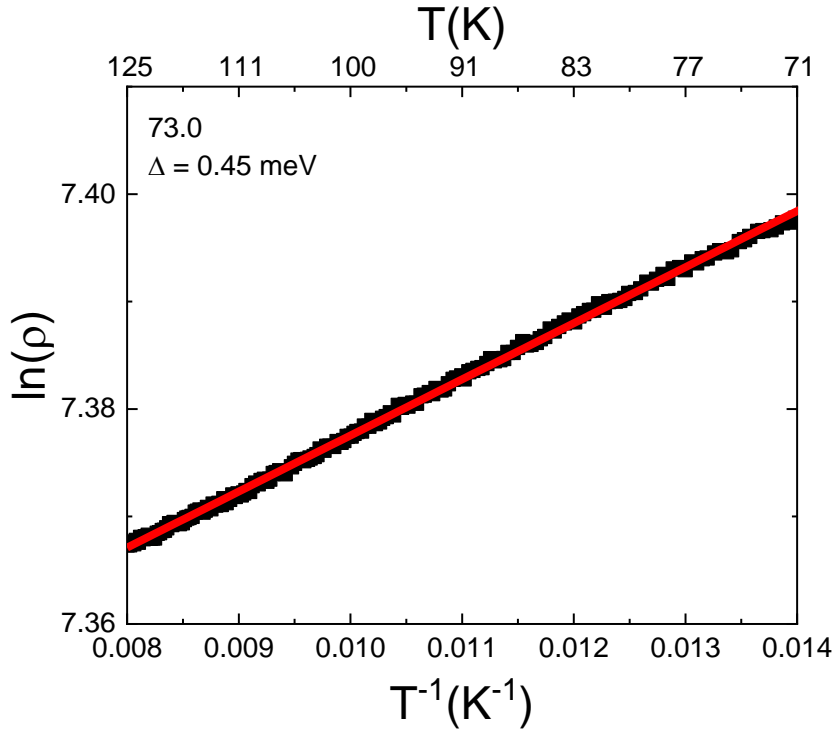


Figure 3.7: Arrhenius plot of IrSb₃ sample 73.0 for $70\text{ K} \leq T \leq 125\text{ K}$.

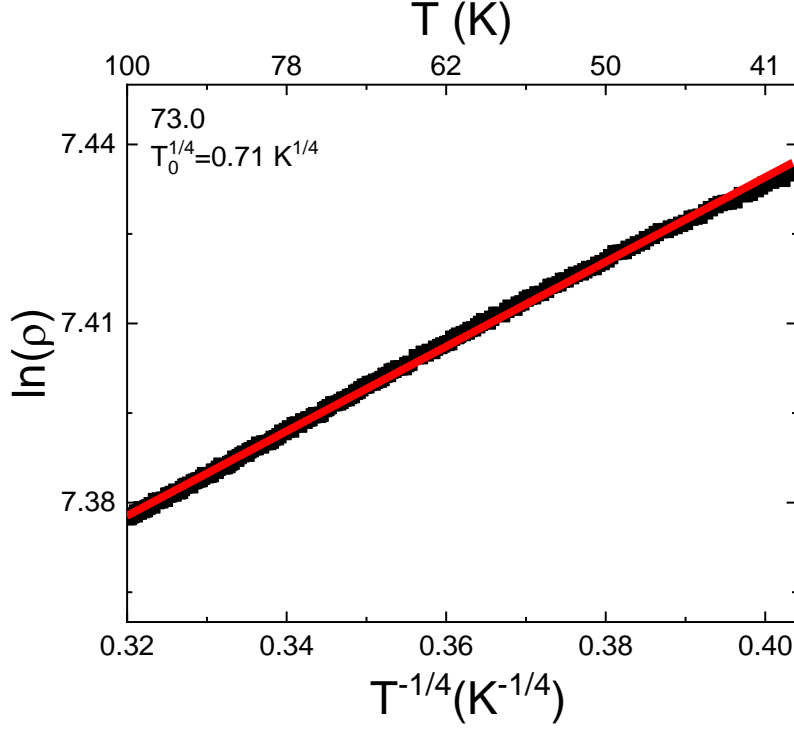


Figure 3.8: Resistivity of IrSb₃ sample 73.0 for temperatures $38K \leq T \leq 100K$.

given by $T_0 = 21.2/k_B a^3 N(E_F)$, where a is the localization length [84]. Figure 3.8 shows a linear relationship in the $\ln(\rho)$ vs $T^{-1/4}$ over a large temperature range $40 K \leq T \leq 100 K$. The slope of the best fit line gives a value of $T_0 = 0.26(3) K$. This value is extremely small in comparison to CoSb₃, which amounts to $T_0 \approx 1 \times 10^5 K$ in Ref. [83]. Below this temperature range, the resistivity changes drastically from 3D VRH insulating behavior and begins to saturate. This saturation behavior has been observed in non-trivial topological semimetal LuPdBi and is attributed to a parallel circuit of insulating bulk and metallic surface conduction [85]. From this analysis one can conclude that 3D VRH is the dominant transport method for $T < 100 K$, similar to what was observed in related material CoSb₃.

The low temperature resistivity ρ vs T for sample 73.1 and corresponding fit is shown in Fig. 3.9. The resistivity behavior is reproduced well in the temperature range of $2 K \leq T \leq 30 K$, under the assumption that it takes the form $\rho = \rho_0 + AT^2 + BT^5$. A fit of this form leads to the values $\rho_0 = 3.57(6) \mu\Omega cm$, $A = 0.00472(6) \mu\Omega cm / K^2$, and $B = 4.69(7) \times 10^{-8} \mu\Omega cm / K^5$.

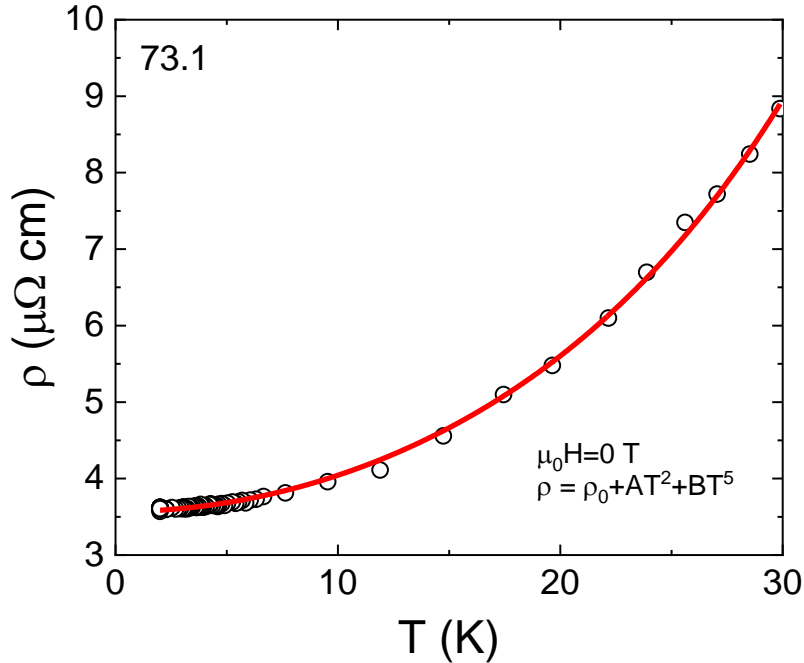


Figure 3.9: Low temperature resistivity versus temperature for IrSb₃.

These values will be discussed later in relation to the filled isostructural material Pr_{0.5}Ir₄Sb_{10.2}Sn_{1.8}. The large RRR and small value of the resistivity is consistent with the semi-metallic behavior that was discussed earlier in this section.

3.1.4.2 Magnetoresistance

The low temperature resistivity of sample 73.1 shows novel behavior never before reported in IrSb₃. The resistivity of this sample in a magnetic field follows suit with equally intriguing behavior. Applying a magnetic field along the *a* axis of the crystal with a perpendicular current along the *c* axis results in an extremely large magnetoresistance in the sample, as can be seen in Fig. 3.10. Figure 3.11 shows the geometry of the measurements on sample 73.1. The 3 perpendicular directions (*a*, *b*, *c*) are aligned along the normal of the facets of the measured crystal, which has a seemingly perfect rectangular shape. However, it cannot be said with certainty that these directions also correspond with the primary unit cell axes, as we do not have single crystal x-ray diffraction data to confirm the orientation. It is however possible for a cubic crystal to grow more in one direction if that is thermodynamically favorable, so these perpendicular facets may indeed correspond to the primary crystal planes. An applied magnetic

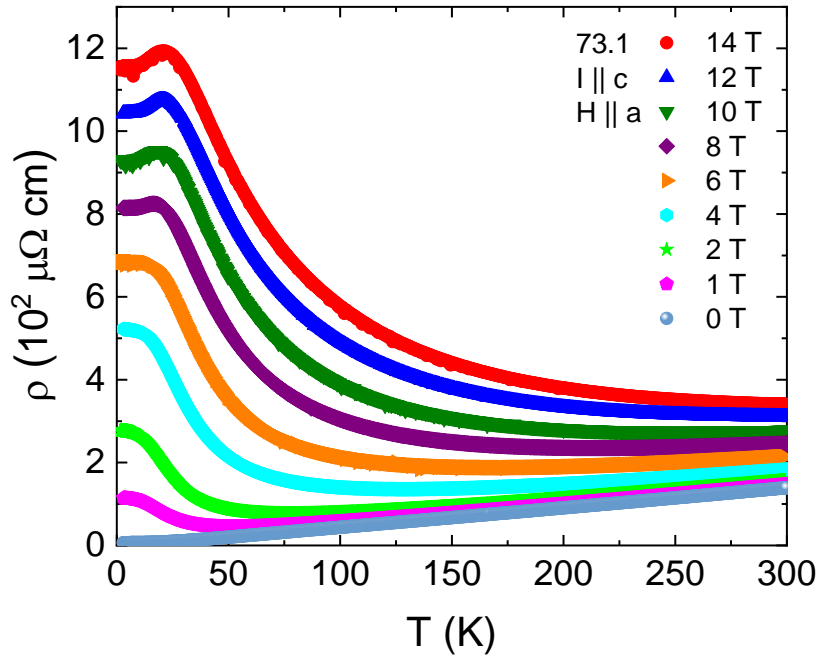


Figure 3.10: Low temperature resistivity versus temperature in various fields for IrSb₃.

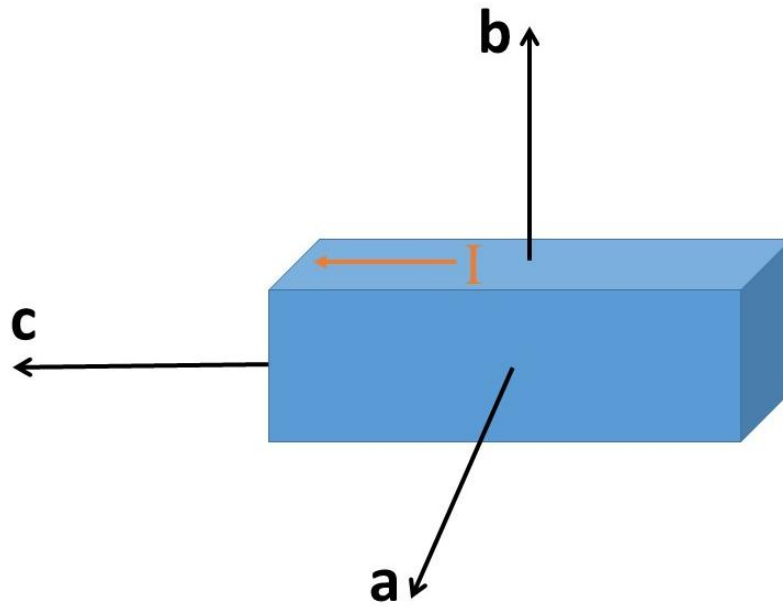


Figure 3.11: Measurement geometry for magnetoresistance.

field as low as 0.25 T is enough to induce insulating-like behavior at low temperatures. This type of behavior has been previously observed in semimetals like bismuth and graphite, and was explained through a multiband treatment that is valid for semimetals with a compensated density of hole and electron carriers [86]. Semimetals that are close to perfectly compensated should have a non-saturating magnetoresistance that is $\propto H^2$. The current and following sections will show that clearly is not the case for this material. This type of field induced metal to insulator behavior has also been seen in various topological semimetals, such as PtSn₄ [87], Cd₃As₂ [80], WTe₂ [88]. Notably, the closely related skutterudite RhSb₃ that is thought to be a zero-gap 3D Dirac semimetal also displays a very similar field induced resistivity upturn [2]. The onset temperature increases with the magnitude of the field such that the sample becomes insulating at around 260 K in a field of 14 T.

This upturn in resistivity is accompanied by a plateau at the lowest temperatures, and for higher fields this plateau becomes a peak. This plateau/reentrant behavior has been seen in graphite and bismuth and has been proposed to be due to multiband effects [86], as well as superconducting correlations of graphite in applied fields high enough to reach the quantum limit [89]. In more recent studies, graphite has been predicted to be topological insulating crystalline material [90] while bismuth also has been experimentally demonstrated to be in the vicinity of a topological phase transition to a strong topological insulator [91]. It is possible that reentrant metallic behavior is a topological effect, as it has also been reported in topological semimetals WP₂ and TaAs [92,93].

The extremely large magnetoresistance is anisotropic in this material, as can be seen in Fig. 3.12-3.13, which compares resistivity with field along two perpendicular principle directions. The largest MR% is observed when the field is aligned with the *a* direction and reaches a value of $3.6 \times 10^4\%$ by 14 T at 2 K. In the perpendicular direction along the *b* axis, the MR% only reaches approximately $1.9 \times 10^4\%$ at the same field and temperature. Quantum oscillations are present in both directions, but have a larger magnitude along the *b* direction. Both curves show no sign of saturation up to 14 T, however much higher field levels would need to be measured to claim that the MR does not indeed saturate. The large MR is approximately an order of magnitude lower than Weyl semimetals NbP, NbAs, TaAs, and more than twice that of TaP [94]. It is also an order of magnitude larger (at 14 T) than that of related compound RhSb₃ [2].

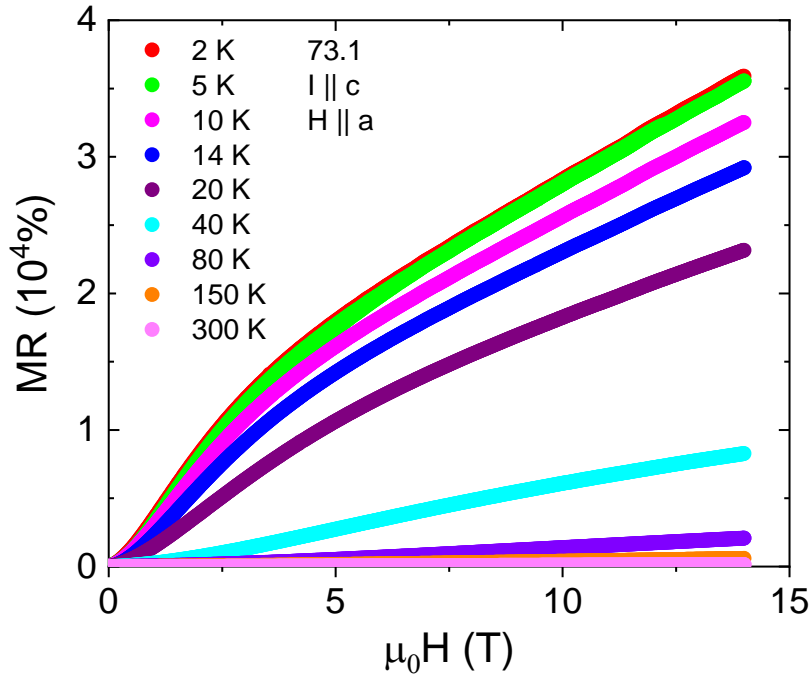


Figure 3.12: MR% of IrSb₃ for various temperatures with field along the *a* axis.

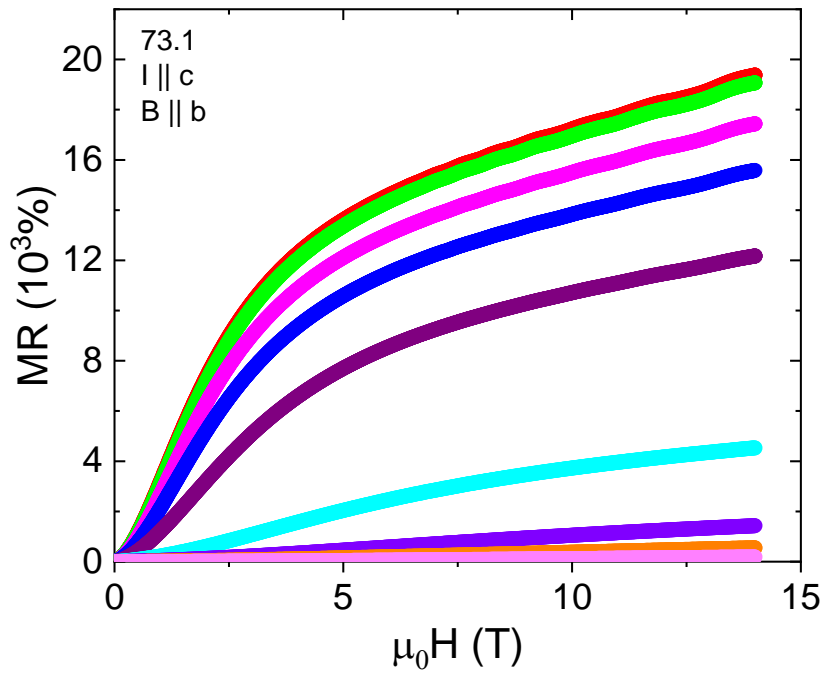


Figure 3.13: MR% of IrSb₃ for various temperatures with field along the *b* axis.

The functional dependence on field changes drastically with decreasing temperature. From room temperature to about 80 K there is typical Lorentzian magnetoresistance that is $\propto H^2$ for most of the field range. This behavior quickly becomes sublinear at low temperatures and high fields. Compensated semimetals with no other scattering mechanism generally have a very large MR which will continue as H^2 under the condition that $n_h \approx n_e$, which is clearly not the case here. Sub-linear MR ($\propto H^n$, $n < 1$) has been observed in various topological semimetals and is thought to be attributed to weak anti-localization (WAL) effects. WAL is a quantum effect that produces an additional scattering term that is a result of the destructive interference of electrons on time-reversed paths in parameter space. WAL has been commonly observed in topological materials [95] and is usually indicative of a non-trivial Berry phase [96].

Previous theoretical analysis place this material in the proximity of a topological phase, with internal strain or tetragonal displacements in the Sb sublattice able to drive the system into a non-trivial topological state [97]. However, the results of their first principle calculations found no metallic character of the quasilinear band (contrary to other reports) and they thus concluded that IrSb₃ is topologically trivial in its equilibrium structure. Contrary to this, the recent groundbreaking topological quantum chemistry theory predicts IrSb₃ to be a topological semimetal [98,99]. Specifically, it is categorized as a symmetry enforced semimetal with Fermi degeneracy (similar to HgTe) and can be driven to a topological insulating state by lowering the crystal symmetry. This analysis is seemingly the most consistent with many of the transport signatures observed experimentally.

An in depth analysis of the topological transport characteristics that seem to be present in this material is currently outside the scope of this project. Further efforts will be focused on determining the Berry phase from quantum oscillations, as well as analyzing potential WAL effects in the magnetoresistance. Angle resolved photoemission spectroscopy (ARPES) measurements are generally necessary to confirm the existence of excitations with Dirac-like dispersion, along with evidence from transport measurements.

3.1.4.3 Hall Resistivity

The symmetrized hall resistivity ρ_{hall} is shown in Fig. 3.14 for a full range of temperature values for sample 73.1. This sample was chosen as the focus for Hall measurements

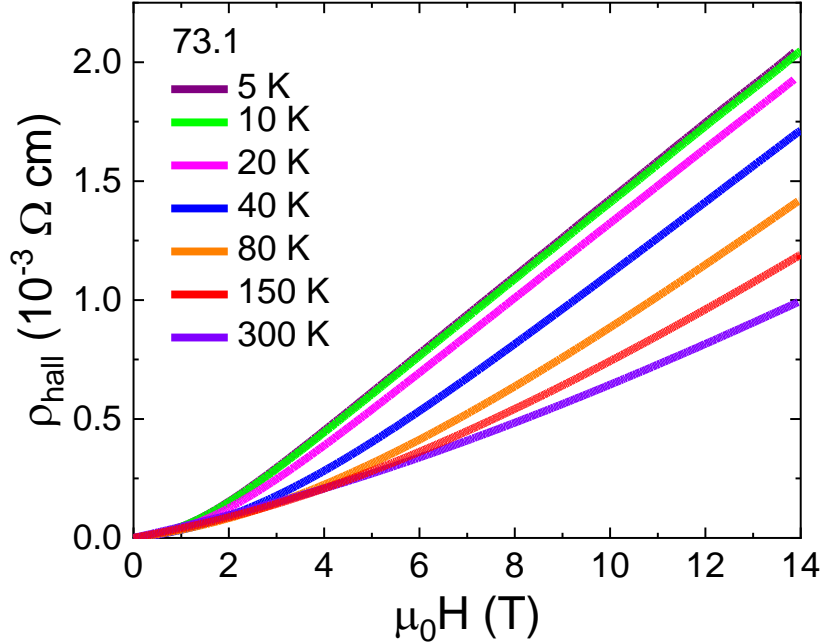


Figure 3.14: Symmetrized Hall resistivity versus temperature for IrSb₃.

as it shows the most interesting and novel behavior. The resistivity is calculated by taking the same measurements with the field direction reversed such that

$\rho_{hall} = 0.5(\rho_{xy}(\mu_0 H) - \rho_{xy}(-\mu_0 H))$, where ρ_{xy} is the transverse resistivity. The purpose of this correction is to account for any misalignment of the hall leads that would produce a signal from the longitudinal direction. The positive slope of the hall resistivity confirms that holes are the dominant carrier for this sample. This is in agreement with previous studies that have found p-type carriers in their undoped polycrystalline samples [75,100,101]. A single band model is assumed for simplicity, though the curvature in the lower fields of the hall resistivity hints at multiple carriers. The hall coefficient is given by $R_H = \rho_{hall}/B$ and can be calculated from the high field slope of the ρ_{hall} vs $\mu_0 H$ plots. From that value one can also calculated the carrier concentration of holes $n_H = 1/R_H e$ [65]. A plot of the Hall coefficient and corresponding carrier concentration as a function of temperature is shown in Fig 3.15. The room temperature carrier concentration $n_H = 6.97 \times 10^{18} \text{ (cm}^{-3}\text{)}$ is of the same order as that found previously in polycrystalline samples [100–102]. This is a fairly low carrier-density system, and paired with metallic resistivity is consistent with the Fermi level crossing near the zero-gap at the Γ point. The carrier concentration decreases by only about 50% from room temperature down to base.

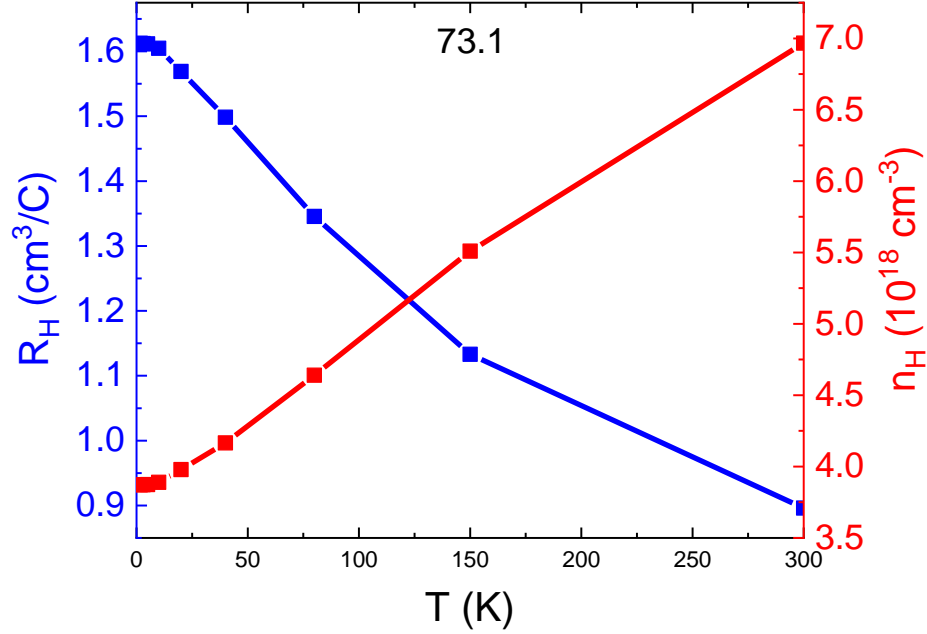


Figure 3.15: Hall coefficient (left) and carrier concentration (right) for IrSb₃.

The Hall mobility can be determined through its relation to the Hall coefficient and longitudinal resistivity and is given by $\mu_H = R_H / \rho_{xx}$. The calculated Hall mobility is shown in Fig. 3.16 over the full temperature range. Previous measurements of the Hall mobility of IrSb₃ were reported to be on the order of $1,000 \text{ cm}^2/\text{Vs}$ at room temperature, whereas sample 73.1 is about 6 times that amount [75,103]. At lower temperatures this sample shows an extremely large value for the Hall mobility, surpassing $220,000 \text{ cm}^2/\text{Vs}$ by $T = 5 \text{ K}$. Such a large value has been coined as ultrahigh mobility and has been observed in many exotic semimetals. Weyl semimetal TaAs has a hall mobility of the same order [104], while Dirac semimetal Cd₃As₂ [80] and Weyl semimetal candidate NbP [105] are one order larger. Fellow antimony based skutterudite RhSb₃ that was recently posited to be 3D Dirac semimetal also has an ultrahigh mobility that is slightly smaller than that found for sample 73.1 [2]. These Hall measurements are an additional piece of evidence towards the potential non-trivial topological nature of IrSb₃. Ultrahigh mobility in this material may be indicative of a topological protection against backscattering that results in a long transport lifetime. This also helps to explain the large value of magnetoresistance, as the application of field could destroy this protection [80]. The previous section also presented other transport characteristics that have been commonly found within

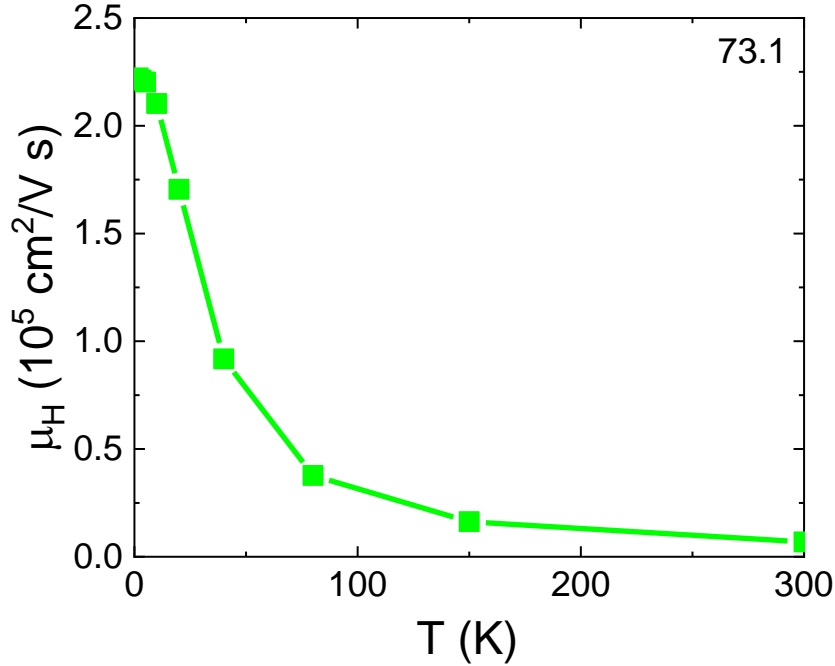


Figure 3.16: Hall mobility versus temperature for IrSb₃.

topological semimetals, extremely large magnetoresistance (MR) and sub-linear MR that may be from weak anti-localization (WAL) effects.

3.2 Pr_{0.5}Ir₄Sb_{10.2}Sn_{1.8}

3.2.1 Crystallography and composition

The first attempted growth of PrIr₄Sb₈Sn₄ resulted in a composition that was different than intended. EDS measurements were used to verify the actual stoichiometric composition of the single crystal growth. Figure 3.17 gives an example of several clean spots that were chosen on the sample to measure to produce a data set. Multiple data sets were then averaged, which resulted in the composition Pr_{0.49(6)}Ir_{4.03(4)}Sb_{10.14(13)}Sn_{1.83(8)}. For ease of reference and due to the compositional similarity to the synthesized powder in Ref. [33], this compound shall be referred to as Pr_{0.5}Ir₄Sb_{10.2}Sn_{1.8}.

Figure 3.18 shows the PXRD pattern and Rietveld refinement of a powdered single crystal Pr_{0.5}Ir₄Sb_{10.2}Sn_{1.8} sample. The refined parameters with estimated error can be found in Table 2. The peaks are well indexed by the LaFe₄P₁₂ type cubic structure with space group $Im\bar{3}$

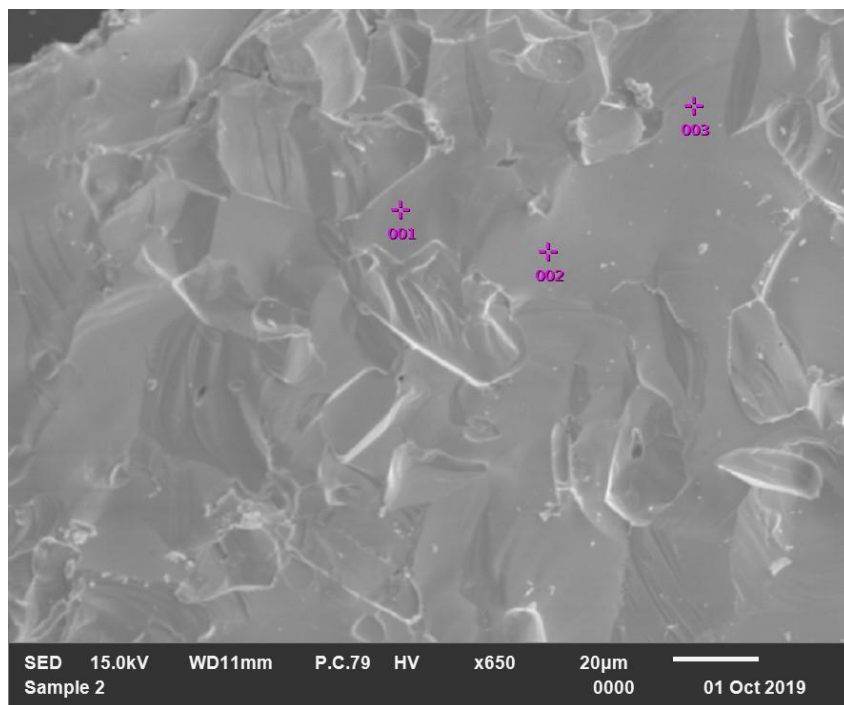


Figure 3.17: Photograph of $\text{Pr}_{0.5}\text{Ir}_4\text{Sb}_{10.2}\text{Sn}_{1.8}$ at x650 magnification.

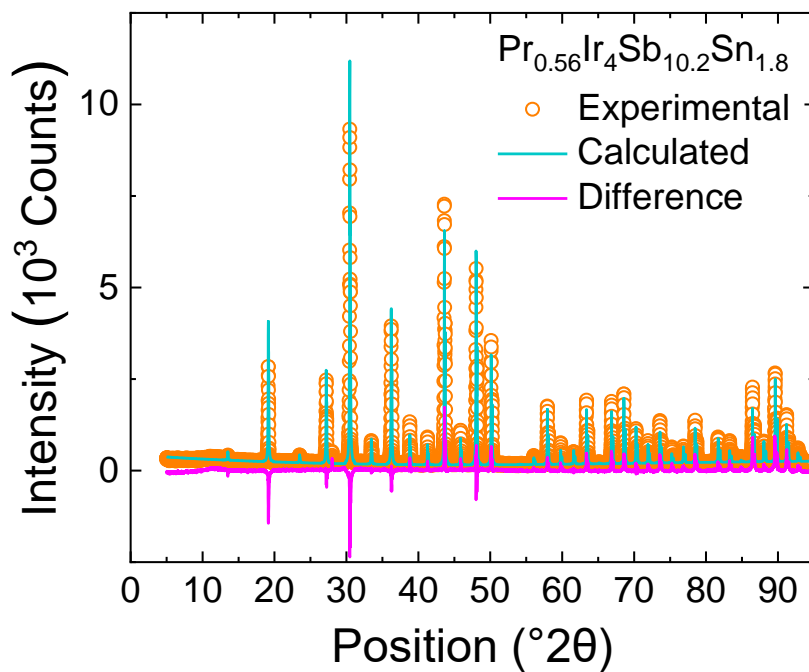


Figure 3.18: XRPD pattern and refinement for $\text{Pr}_{0.5}\text{Ir}_4\text{Sb}_{10.2}\text{Sn}_{1.8}$.

Table 2

Rietveld Refinement Parameters for $\text{Pr}_{0.56}\text{Ir}_4\text{Sb}_{10.08}\text{Sn}_{1.92}$.

Cell Parameter	9.2783(4) Å
Pr Occupancy Site Factor (SOF)	0.564(4)
Pr B_{iso}	3.649(17) Å ²
GOF	3.23

(#204). There is one very small peak of impurity phase at 28° . A search and match was performed to compare other potential phases that could have resulted from the growth, however no match was found. This peak has a very low intensity, thus it is mostly inconsequential to the fit. Refinement of the lattice parameter resulted in $a = 9.2783 \text{ \AA}$. This is very close to the value given by Ref. [33] of $a = 9.2773 \text{ \AA}$ for $\text{Pr}_{0.9}\text{Ir}_4\text{Sb}_{10.2}\text{Sn}_{1.8}$. The Pr occupancy was tentatively refined using multiple separate data sets and found to be approximately 0.56. This result is in fair agreement with EDS measurements. The simulated pattern is produced under the assumption that within a unit cell there are random distributions of 12 Sb/Sn atoms on 24g sites. An Sb occupancy of 0.84 and Sn occupancy of 0.16 resulted in a better fit to the data and are close to the results of EDS measurements. Errors in the agreement of the refinement with EDS may also be due to variances of composition between crystals (as is seen in resistivity measurements) as well as a potential non-random substitution of Sn on Sb sites. Over or underestimations of peaks within the refinement may be due to preferential orientation of crystallites or larger crystal sections which were not properly ground prior to measurement. Compositional variances found in the samples could also contribute to the lack of a perfect fit.

3.2.2 Magnetization

Figure 3.19 shows measurements of the DC magnetic susceptibility χ from $2 \text{ K} \leq T \leq 300 \text{ K}$ in a field of $\mu_0 H = 100 \text{ mT}$. The temperature dependence of the data implies paramagnetic behavior, as can be seen by the increasing moment with decreasing temperature. Filling IrSb_3 with Pr^{3+} ions has caused the material to display paramagnetism rather than

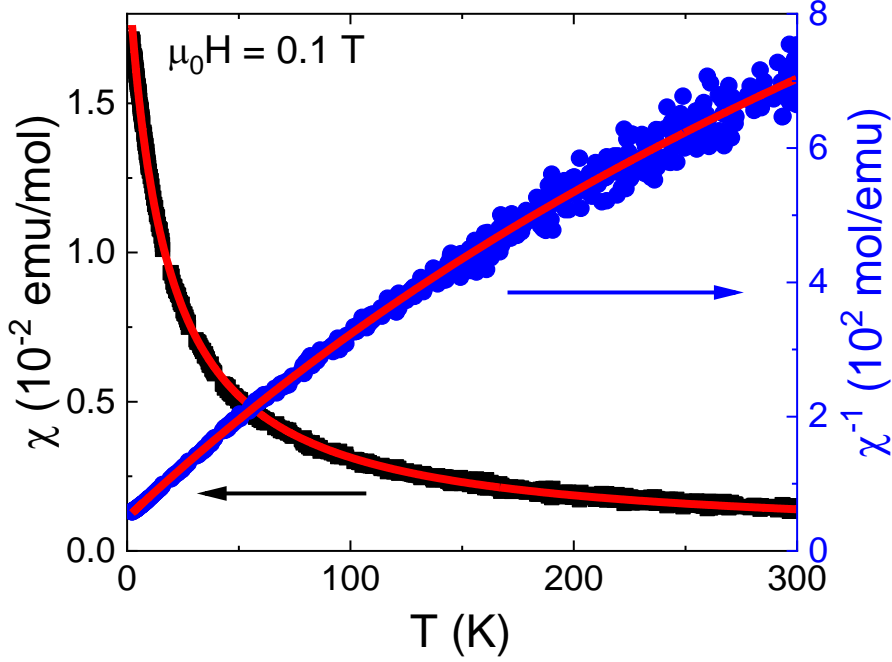


Figure 3.19: The molar magnetic susceptibility (left axis) and its inverse (right axis) for $\text{Pr}_{0.5}\text{Ir}_4\text{Sb}_{10.2}\text{Sn}_{1.8}$.

temperature independent diamagnetism. This is due to the localized unfilled shell of f-electrons of the Pr ions. The local spins align with the applied field and create a net magnetic moment, one that gets stronger as spin fluctuations decrease with thermal energy.

A Curie-Weiss fit is performed using the expression described earlier in the text, $\chi = \chi_0 + C/(T - \theta_w)$. The best fit produces $\chi_0 = 4.5(1) \times 10^{-4} \text{ emu/mol}$, $\mu_{\text{eff}} = 1.56(15) \mu_B/f.u.$, and Curie-Weiss temperature $\theta_w = -15.5(5) \text{ K}$. Antiferromagnetic correlations which are common for Kondo lattice compounds are indicated by a large negative Curie-Weiss temperature [106,107]. The Curie-Weiss temperature can also be used to get a rough idea of the Kondo temperature through the relation $T_K = |\theta_w|/4$ [107]. This estimates the Kondo temperature as $T_K \approx 3.9 \text{ K}$. The effective moment of the Pr ions is calculated as

$\mu_{\text{eff}} \approx 3.12 \mu_B/\text{Pr}^{3+}$, if one takes into account the partial filling of Pr^{3+} ions in $\text{Pr}_{0.5}\text{Ir}_4\text{Sb}_{10.2}\text{Sn}_{1.8}$.

The effective moment found is smaller than the value of a Pr^{3+} free ion that has $\mu_{\text{eff}} \approx 3.58 \mu_B$. It is however close to the effective moment $\mu_{\text{eff}} \approx 2.97 \mu_B/f.u.$ found for $\text{PrOs}_4\text{Sb}_{12}$ which also shows heavy fermion behavior [28]. The effective moment may be reduced in value due to

screening of the f -moments of the through the Kondo effect or mixed valence states of the Pr^{3+} ions. One can already start to deduce from the magnetization data that a main consequence of filling IrSb_3 with a rare-earth ion is inducing Kondo-alloy effects.

Figure 3.20 shows magnetic susceptibility χ measurements for $2\text{ K} \leq T \leq 8\text{ K}$, for various low fields in a zero field cooled (ZFC) and field cooled (FC) experimental scheme. There is a transition at $T \approx 4.2\text{ K}$ ($\mu_0 H = 5\text{ mT}$) that is evidenced by a small and sudden diamagnetic signal. The transition shifts to lower temperature with increasing field and is eventually pushed below $T = 2\text{ K}$ at a field of $\mu_0 H = 60\text{ mT}$. There is hysteretic behavior seen when comparing the ZFC vs FC data. This behavior is consistent with superconductivity with $T_c \approx 4.2\text{ K}$ [108,109]. Without considering demagnetization effects, the volume fraction can be estimated to be $< 0.5\%$. Demagnetization effects should not change the estimate by a considerable amount due to the geometry of the sample.

Figure 3.21 shows $M(H)$ sweeps at a constant temperature for $\text{Pr}_{0.5}\text{Ir}_4\text{Sb}_{10.2}\text{Sn}_{1.8}$ at temperatures in proximity of $T_c \approx 4.2\text{ K}$. In the lowest fields to approximately $\mu_0 H = 60\text{ mT}$ there is magnetic hysteresis that reproduced well with multiple sweeps. There is a coexistence of paramagnetic behavior with a small diamagnetic peak at low fields [110]. The diamagnetic peak and irreversibility in the $M(H)$ loop are typical of a “dirty” type 2 superconductor [111]. The coercivity seen due to the diamagnetic signal monotonically approaches zero as T approaches T_c . Thus, most of the hysteretic behavior is due the field sweeps into and out of the superconducting state “freezing” magnetic flux in the material.

The possibility of an impurity phase within the material should be considered, as the superconducting fraction is very small. There is no direct evidence of Sn impurities in the PXRD data, however there is a possibility that the small superconducting fractions found in the majority of the samples are due to a small amount of impurity phase of Sn. Elemental Sn has a T_c that is lower than what is found for this material, approximately 3.7 K . However, there is evidence of Sn alloys doped with Sb that are type 2 superconductors and have greater transition temperatures close to 4 K [112]. The highest transition temperature was found to be $T_c = 3.96\text{ K}$ at a 6% atomic concentration of Sb. This value is close to, but still significantly lower than the transition temperature found in these samples. It also seems unlikely that this particular alloy would form,

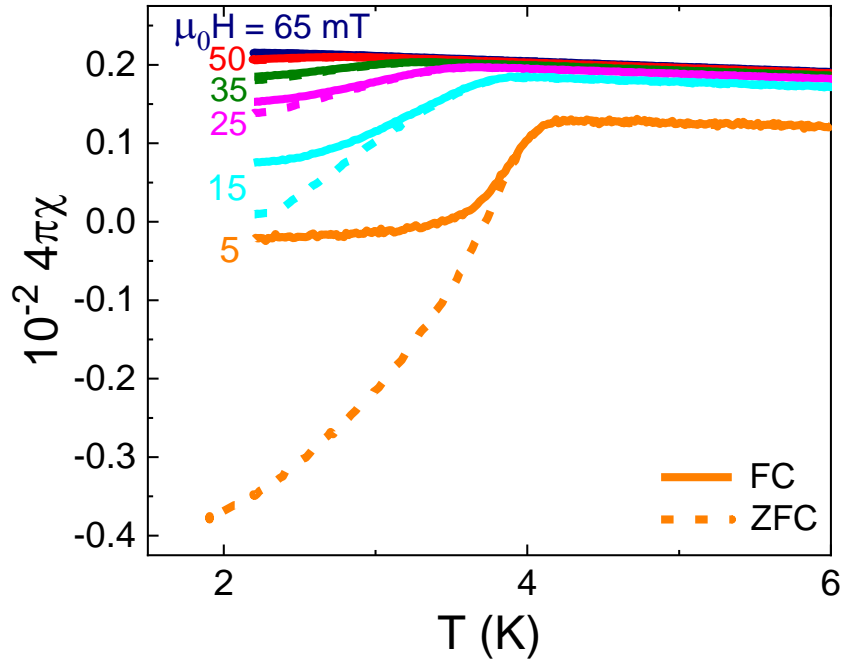


Figure 3.20: ZFC and FC magnetic susceptibility near the superconducting transition for $\text{Pr}_{0.5}\text{Ir}_4\text{Sb}_{10.2}\text{Sn}_{1.8}$.

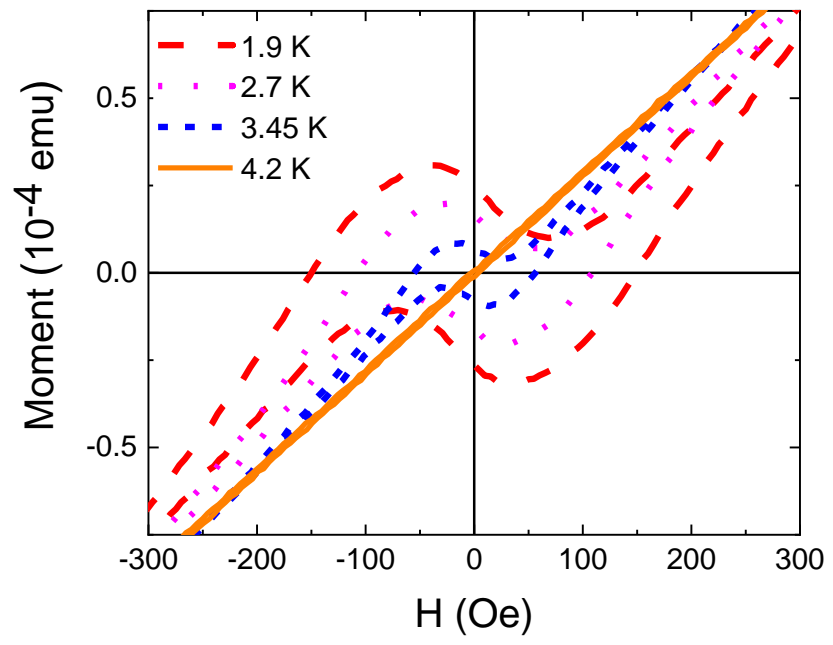


Figure 3.21: Hysteresis loops for $\text{Pr}_{0.5}\text{Ir}_4\text{Sb}_{10.2}\text{Sn}_{1.8}$.

as the single crystals were grown in a flux of 2:1 ratio of Sb to Sn. The lower critical field H_{c1} values that are inferred from the hysteresis loops in Fig. 3.21 are also lower than that found for any superconducting Sn-Sb alloy reported in Ref. [112].

3.2.3 Specific Heat

Figure 3.22 shows the specific heat $C(T)$ for $2 K < T < 200 K$. The high temperature specific heat has the general temperature dependence of typical metal and is reproduced well by the Debye model. The temperature dependence of the high temperature specific heat takes the form given previously in equation 2.8. The resulting Debye temperature is found as $\theta_H \approx 268 K$. The compound $\text{LaOs}_4\text{Sb}_{12}$ has a comparable value of $\theta_H = 304 K$ [28] as well as the Pr based skutterudite $\text{PrRu}_4\text{As}_{12}$ ($\theta_H = 344 K$) [113]. It is also slightly lower than what was found for the unfilled material IrSb_3 ($\theta_H = 282 K$).

Figure 3.23 hones in on the low temperature $C(T)$. Although the magnetization data indicates a superconducting fraction, there is no detectable peak from a superconducting phase transition. However, due to the small amount of superconducting material (0.5%), the expected $\Delta C/T_c \gamma = 1.43$ (calculated assuming weak-coupling isotropic BCS theory) is difficult to detect, as the other contributions to the specific heat at that temperature are approximately two orders of magnitude greater [114]. Kondo correlations that appear to be present in this material may further reduced a specific heat jump from superconductivity [115]. Figure 3.24 shows the same data as $C(T)/T$ vs T^2 for $1.8 K \leq T \leq 20 K$. The solid line is a $C(T) = BT^3$ Debye term with $\theta_L = 240 K$ for reference. One can see there is a curvature present that is causing the specific heat to deviate from T^3 behavior over the entire temperature range. There is likely an extra contribution to the specific heat from a low temperature Einstein mode or from Kondo resonance or a combination of the two.

An Einstein oscillator term likely needs to be considered to model oscillations of the Pr^{3+} ions within their oversized pnictogen cages. Einstein modes have been found to exist in several different filled skutterudite systems as a result of the guest atoms. To test this hypothesis, the Pr contribution is removed from the Debye specific heat and is substituted for an Einstein mode,

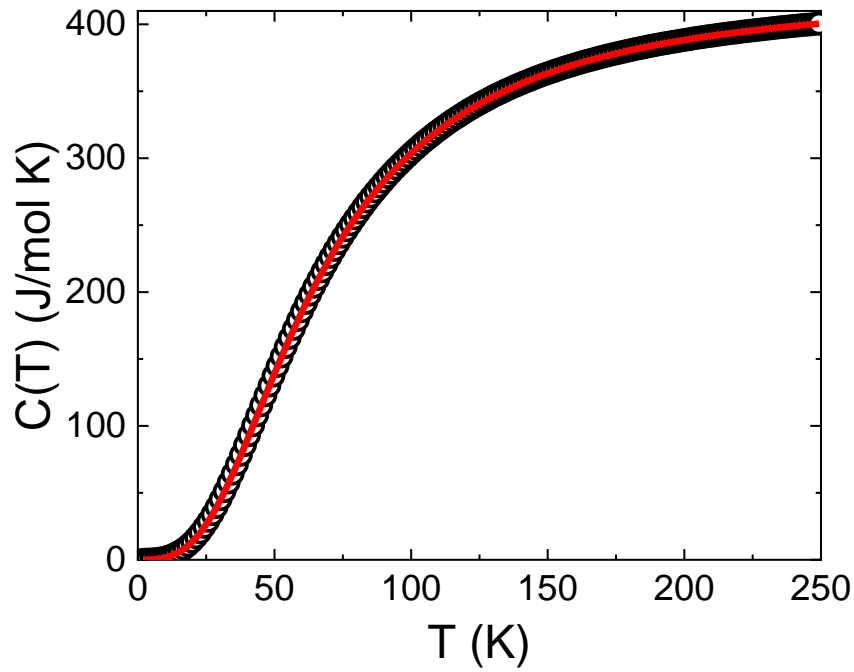


Figure 3.22: High temperature specific heat for $\text{Pr}_{0.5}\text{Ir}_4\text{Sb}_{10.2}\text{Sn}_{1.8}$.

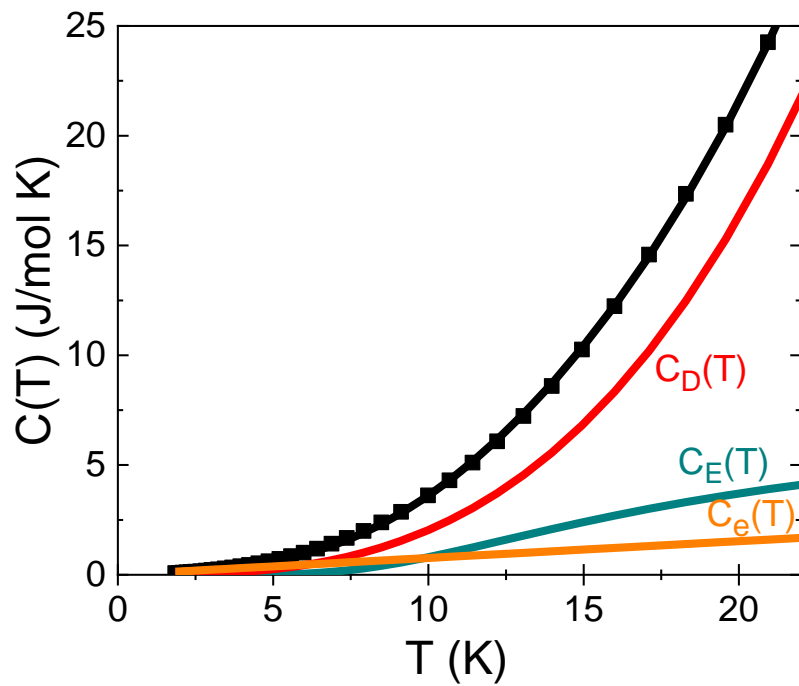


Figure 3.23: Low temperature specific heat for $\text{Pr}_{0.5}\text{Ir}_4\text{Sb}_{10.2}\text{Sn}_{1.8}$.

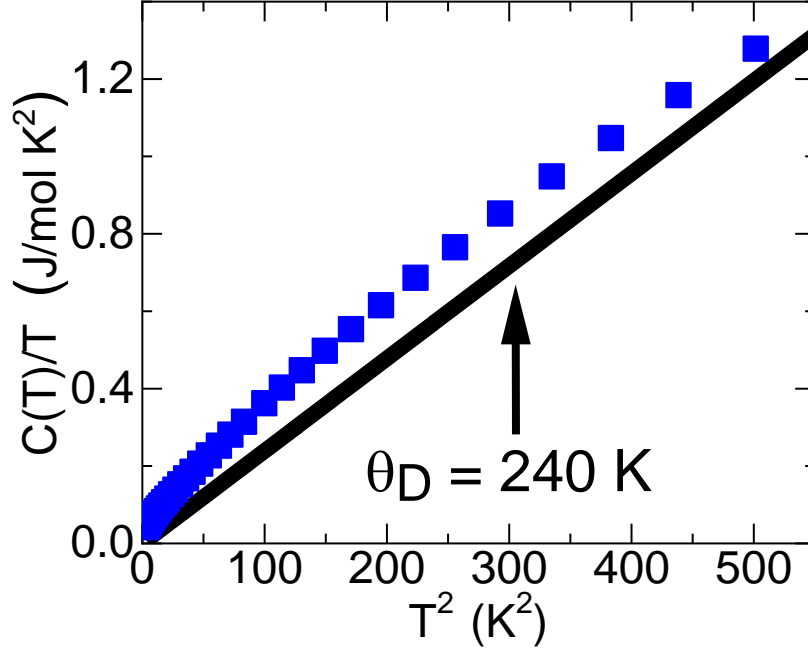


Figure 3.24: Low temperature specific heat over temperature for $\text{Pr}_{0.5}\text{Ir}_4\text{Sb}_{10.2}\text{Sn}_{1.8}$. The black line is a guide to the eye.

using fits of the form

$$C(T) = C_e(T) + (n-x)C_D(T) + (x)C_E(T), \quad (3.1)$$

for $1.8 \text{ K} \leq T \leq 25 \text{ K}$. In this equation, $n = 16.5$, $C_e(T) = \gamma T$, $C_D = BT^3$ where $B = 1944/\theta_L^3$ with θ_L representing the Debye temperature, and

$$C_E(T) = 3R \frac{(\theta_E/T)^2 e^{(\theta_E/T)}}{(e^{(\theta_E/T)} - 1)^2}, \quad (3.2)$$

where θ_E is the Einstein temperature. It should be noted that within the lattice term it is required that $x \leq 0.5$. This ensures that only the Pr^{3+} ions contribute. The values obtained for the fit are $\gamma = 86(6) \text{ mJ/mol K}^2$, $\theta_L = 240(1) \text{ K}$, $\theta_E = 61(2) \text{ K}$, and $x = 0.39(4)$. The quality of the fit improves significantly as $\chi^2 = 0.87$ with the Einstein term, compared to $\chi^2 = 7.23$ without.

The Debye temperature is consistent with the high temperature fit and is less than that found for the low temperature fit of IrSb_3 . The Debye temperature of a solid sets a limit on the highest normal mode of vibration found and is also related to the elastic and thermal properties. By filling IrSb_3 with Pr (and Sn to compensate electronically), the lattice constant of the material increases slightly. This fact, along with fractional Pr filling, seems to have a softening effect on

the lattice. Random Sn inclusions on Sb sites may also introduce disorder into the lattice vibrations due to the mismatch of ionic radii. A previous report that focuses on the effects of a filler ion in the skutterudite structure claims that the Einstein modes that result from a filler ion couple with the acoustic modes of the lattice, effectively reducing the phonon group velocity in proximity to a characteristic frequency [116]. They thus concluded that anharmonic umklapp scattering processes are responsible for interfering with phonon propagation. This is in contrast to previous treatment of the filler ion, where rattling motion of the ion in its oversized cage is thought to result in resonant acoustic phonon scattering [117]. The depression of the phonon spectrum from the filler ion is also thought to be responsible for lowering the thermal conductivity, a desired effect in the pursuit of a good thermoelectric material [118].

The value of the Einstein temperature found in the fit is close to values found for $\text{PrOs}_4\text{Sb}_{12}$ ($\theta_E \approx 75 \text{ K}$) in x-ray absorption fine structure measurements [39]. The enhanced isotropic Debye-Waller coefficient B_{iso} (mentioned earlier in the text) found for the Pr^{3+} ions by refinement of the PXRd data is also remarkably consistent with an existing Einstein oscillator with $\theta_E \approx 63 \text{ K}$. The electronic specific heat coefficient is relatively enhanced from that of a typical metal and is indicative of the strong electron correlations within this material. It also lies within the range that is typically classified as heavy fermion [50,119–121].

The lattice contribution, which is made of Debye and Einstein modes, is given by

$$C_{lat}(T) = (16.5 - x)C_D(T) + (r)C_E(T), \quad (3.3)$$

and is subtracted from $C(T)$. This allows for a deeper analysis of the low temperature specific heat, as only $C_{e+m}(T)$ remains, the electronic and magnetic contributions. Figure 3.25 shows the plot of $C_{e+m}(T)/T$ vs T for $1.8 \text{ K} \leq T \leq 20 \text{ K}$ and fields of up to $\mu_0 H = 14 \text{ T}$. Figure 3.26 shows $C_{e+m}(T)/T$ vs T^2 at the lowest temperatures. There is a wide peak centered near 8 K at $\mu_0 H = 0 \text{ T}$ which has a strong field dependence. This peak is likely an artifact of the subtraction of the lattice contribution, though it is expected to have excess specific heat in this temperature region due to Kondo effects. The inset shows that the low temperature region starts to follow $C(T)/T = \gamma + BT^2$ more closely as the field is increased. The entropy due to the Pr ions is determined by combining dilution refrigerator data with higher temperature data to include the entropy below $T = 1.8 \text{ K}$. Figure 3.27 shows the result of splicing the data from the two

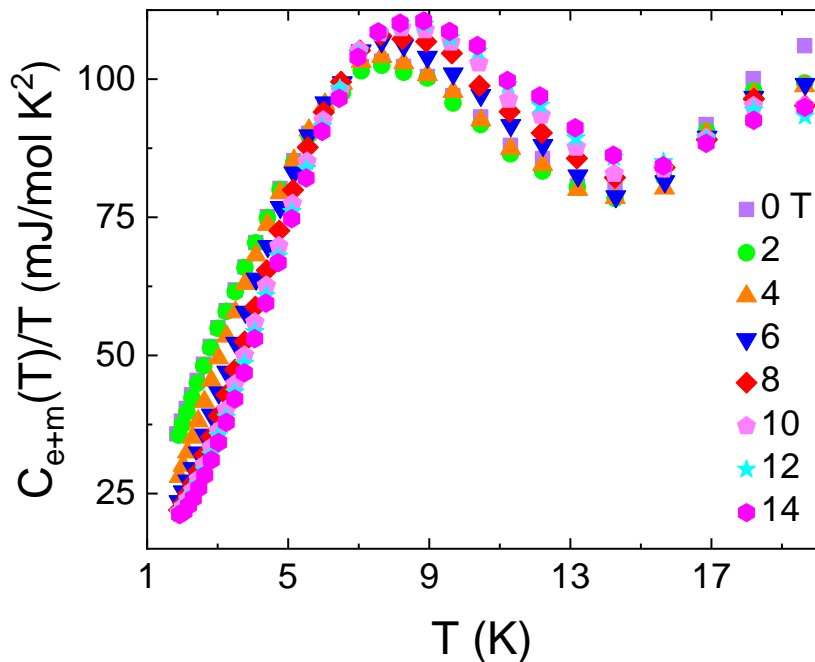


Figure 3.25: Low temperature electronic and magnetic specific heat over temperature for $\text{Pr}_{0.5}\text{Ir}_4\text{Sb}_{10.2}\text{Sn}_{1.8}$.

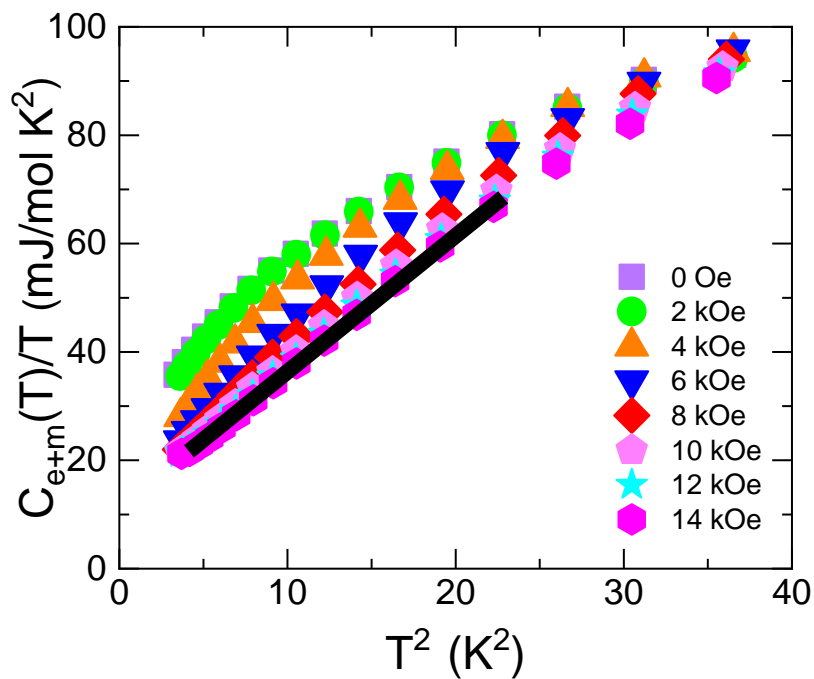


Figure 3.26: Low temperature electronic and magnetic specific heat over temperature versus temperature squared for $\text{Pr}_{0.5}\text{Ir}_4\text{Sb}_{10.2}\text{Sn}_{1.8}$. The line is a guide to the eye and represents adherence to T^3 behavior as excess specific heat is suppressed with field.

measurements after the subtraction of the nuclear and lattice contributions to the specific heat. Numerical integration of the $(C - C_{lat} - C_{nuc})/T$ vs T plot gives the total entropy, which is then scaled to the amount of Pr within the material. The results show that the entropy is greatly reduced from that expected for a ground-state doublet, even up to $T = 20 K$. The implication of a reduced spin entropy, as well as the enhanced Sommerfeld coefficient, are both consistent with the Kondo effect appearing in this material [115,122].

The field dependent specific heat is analyzed by plotting $[C(\mu_0 H) - C(\mu_0 H = 14 T)]/T$ or $\Delta C_{mag}(T)/T$, shown in Fig. 3.28. There is peak centered near $T \approx 3 K$ at zero field. This is fairly close to the estimate of the Kondo temperature $T_K \approx 4 K$ from magnetic susceptibility data. The excess specific heat $\Delta C_{mag}(T)$ appears to be shifted towards higher temperatures as the field is increased. This behavior is clearly indicative of Kondo correlations, as the suppression of the Kondo effect by magnetic fields has been observed in numerous materials [123–125]. When exposed to similar magnetic fields values, the Kondo alloys $Ce_{1-x}Y_xCu_2Si_2$ and $La_{1-x}Ce_xAl_2$ show the same qualitative behavior in $C(T)/T = \gamma(T)$ [126].

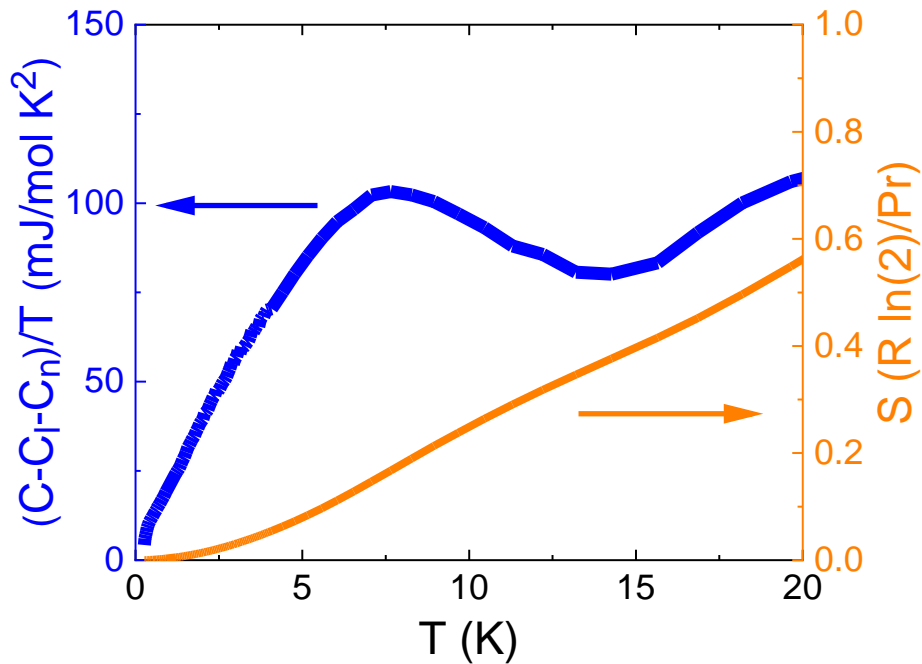


Figure 3.27: Low temperature specific heat (left axis) and corresponding entropy (right axis) for $0.25 K \leq T \leq 20 K$ for $Pr_{0.5}Ir_4Sb_{10.2}Sn_{1.8}$.

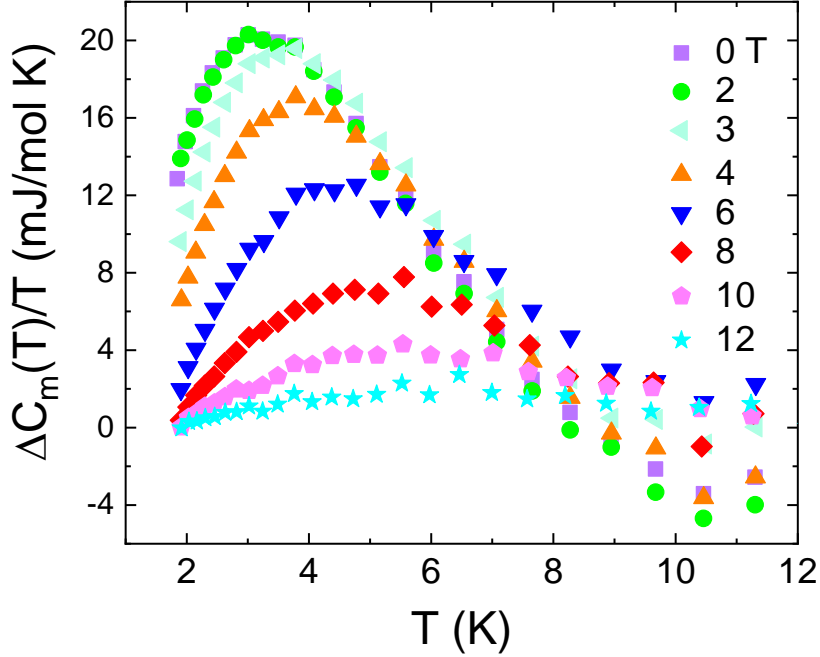


Figure 3.28: Low temperature field dependent specific heat for $\text{Pr}_{0.5}\text{Ir}_4\text{Sb}_{10.2}\text{Sn}_{1.8}$.

Finding a consistent model for the low temperature specific heat is difficult due to the coexistence of excess specific heat at low temperatures from the Kondo effect and a possible Einstein mode from rattling of the Pr ions. Results of the fitting procedure vary depending on small changes in temperature range due to the relatively close proximity of these contributions. The parameters that are reported for the low temperature model do not entirely reproduce the high temperature data. They still however serve as an estimated lattice contribution to be used for subtraction. Inelastic neutron or inelastic x-ray scattering measurements may help in determining a more accurate Einstein temperature for this material without the use of interdependent fitting parameters [127]. It may also be possible to synthesize a lanthanum analogue of this material with a similar filling fraction of La to approximate the phonon contribution.

Figure 3.29 shows the specific heat at very low temperatures ($T < 0.25 \text{ K}$) where a nuclear contribution from hyperfine splitting dominates. To separate the nuclear contribution, one can assume that the specific heat takes the form given in Equation 2.11, for $T \leq 0.5 \text{ K}$. To get an accurate value for A_n , it is useful to subtract a curve with the power dependence n as a fitting parameter to remove all contributions that are not related to the nuclear Schottky peak. This fit gives a value of $A_n^{1/2} = 2.26 \times 10^{-2} (\text{J K/mol})^{1/2}$, which amounts to about 79% of the Sb

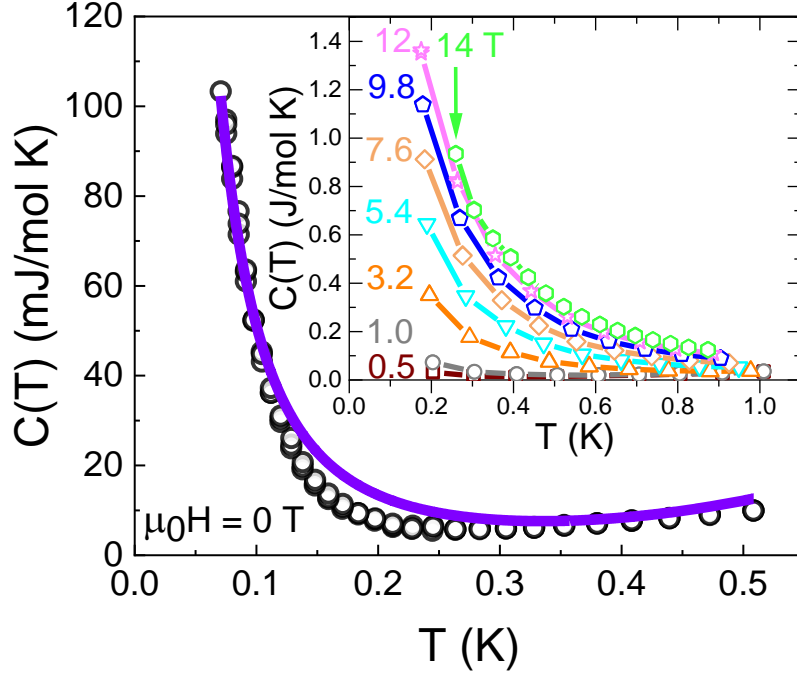


Figure 3.29: The nuclear specific heat with field dependence inset for $\text{Pr}_{0.5}\text{Ir}_4\text{Sb}_{10.2}\text{Sn}_{1.8}$.

electronic quadrupole contribution estimated for $\text{PrOs}_4\text{Sb}_{12}$ from Sb NQR measurements [31]. According to Aoki et al., approximately 99% of the nuclear Schottky contribution comes from Sb for $\text{PrOs}_4\text{Sb}_{12}$ in zero field. Intra-site hyperfine coupling between the Pr^{3+} 4f moments and the nucleus is responsible for most of the field dependence of $A_n^{1/2}$ in $\text{PrOs}_4\text{Sb}_{12}$, while Os and Sb contribute a negligible amount. This allows one to get a qualitative view of the local site averaged magnetic moments of the Pr ions from the nuclear specific heat.

Using the nuclear Schottky contributions of $\text{PrOs}_4\text{Sb}_{12}$ as a reference for $\text{Pr}_{0.5}\text{Ir}_4\text{Sb}_{10.2}\text{Sn}_{1.8}$ is tempting, as it has potential in determining relative Sb concentrations or contributing to an analysis of the magnetism of the Pr ions at low temperatures. Some important differences may make such an analysis more challenging. Ir isotopes with large quadrupole moments ($Q'_{\text{Pr}} = 775 \text{ mb}$ averaged over existing stable isotopes [128]) complicate the situation for $\text{Pr}_{0.5}\text{Ir}_4\text{Sb}_{10.2}\text{Sn}_{1.8}$ in zero field. There are likely also differences in the local electric field gradient for Sb nuclei that affect the quadrupole contribution. Sn has no stable isotope with $I \geq 1$ and a very small nuclear moment when averaged over all stable isotopes; thus it does not add any complication [129]. Experimental values of the electric field gradient ∇E as well as H_{eff} for Ir and Sb in $\text{Pr}_{0.5}\text{Ir}_4\text{Sb}_{10.2}\text{Sn}_{1.8}$ would help in calculating the zero field contribution and achieving

more quantitative results. However, those measurements are currently beyond the scope of this work.

A qualitative look at the site averaged magnitude of the Pr magnetic moment may still be formed because the field dependence of $A_n^{1/2}$ presents less complications. As stated earlier, 99% of the field dependence in $\text{PrOs}_4\text{Sb}_{12}$ is due to the hyperfine coupling of Pr ions. The Os and Sb in that material give a nearly negligible contribution to the field dependence. A similarly small contribution is expected for the Sb/Sn in $\text{Pr}_{0.5}\text{Ir}_4\text{Sb}_{10.2}\text{Sn}_{1.8}$. As the magnitude of the nuclear moments for ^{191}Ir and ^{193}Ir are only approximately 4% of the magnitude of the ^{141}Pr nuclear moment, the Ir contribution should not have a great effect on the analysis. The dominant interaction is expected to come from Pr due to the 4f moments becoming polarized in a magnetic field, while the other constituent atoms are non-magnetic. This would mean H_{eff} is larger for the Pr nuclei, and thus a stronger hyperfine coupling.

The Hamiltonian for the hyperfine interactions is given by

$$H_N = a' I_z + P \left(I_z^2 - \frac{I(I+1)}{3} \right), \quad (3.4)$$

where $a' = A_{hf} \langle J_z \rangle$ represents the magnetic hyperfine constant and

$$P = B \left\langle J_z^2 - \frac{J(J+1)}{3} \right\rangle, \quad (3.5)$$

is the quadrupole coupling constant [17]. The magnetic hyperfine constant gives a measure of the electronic magnetization while quadrupole coupling constant provides an average value of the electric quadrupole moment. Following Aoki et al. [31], one can replace $\langle J_z \rangle$ with the site

averaged $\left(\overline{\langle J_z \rangle^2} \right)^{1/2}$, and then define the site averaged magnetic moment of the Pr ions,

$m_{Pr} = g_J \left(\overline{\langle J_z \rangle^2} \right)^{1/2}$. The magnetic hyperfine Pr contribution to the field dependent $A_n^{1/2}$ is

$$A_n^{\text{Pr}} = \frac{R}{3} \left(\frac{A_{hf} m_{Pr}}{g_j} \right)^2 I(I+1), \quad (3.6)$$

where A_{hf} is the magnetic dipole hyperfine coupling constant, m_{Pr} is the site-averaged magnitude of the Pr magnetic moment and g is the Landé g-factor. Through this relation, one

can determine that the plot of $A_n^{1/2}$ vs $\mu_0 H$ in Fig. 3.30 reflects a qualitative view of the magnitude of the site averaged moment.

There is a steep increase in the magnitude of $A_n^{1/2}$ as the field is increased, followed by a saturation type behavior. The change in slope at approximately $\mu_0 H = 5 T$ is aligned well with $C(H)/T$ data shown in Fig. 3.31, which also gives a measure of the Kondo correlations. The field dependence of the specific heat shows that as the conduction electrons couple with the $4f$ moments at lower temperatures, there is a notable loss of spin entropy. The $4f$ moments become polarized as the field magnitude is increased; this results in the probability of spin-flip scattering decreasing, thus the Kondo effect is suppressed. The plot of γ vs $\mu_0 H$ shown in Fig. 3.31 was produced by fitting the specific heat to $C(T) = \gamma T + BT^3$ from $1.8 K \leq T \leq 4 K$. This analysis also agrees with the previous arguments on the field suppression of the Kondo effect. The Sommerfeld coefficient decreases with field and then saturates at around $10 mJ/mol K^2$. A relatively weak correlation between the $4f$ moments and conduction electrons is implied by the value found for γ in zero field ($29 mJ/mol K^2$). This amount is on the lower end of the range where heavy fermions are typically defined. There is a discrepancy in the value found for γ

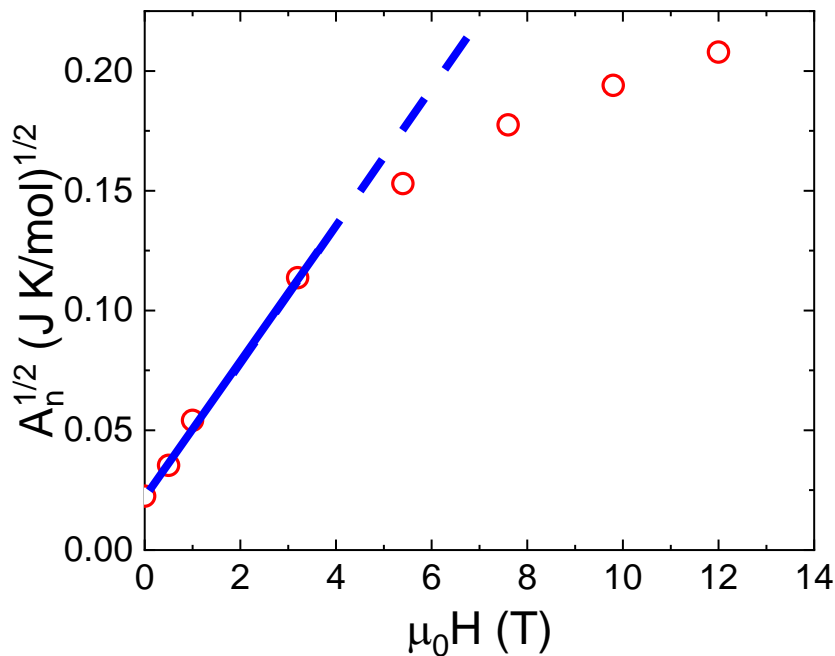


Figure 3.30: Field dependence of the nuclear specific heat coefficient for $\text{Pr}_{0.5}\text{Ir}_4\text{Sb}_{10.2}\text{Sn}_{1.8}$.

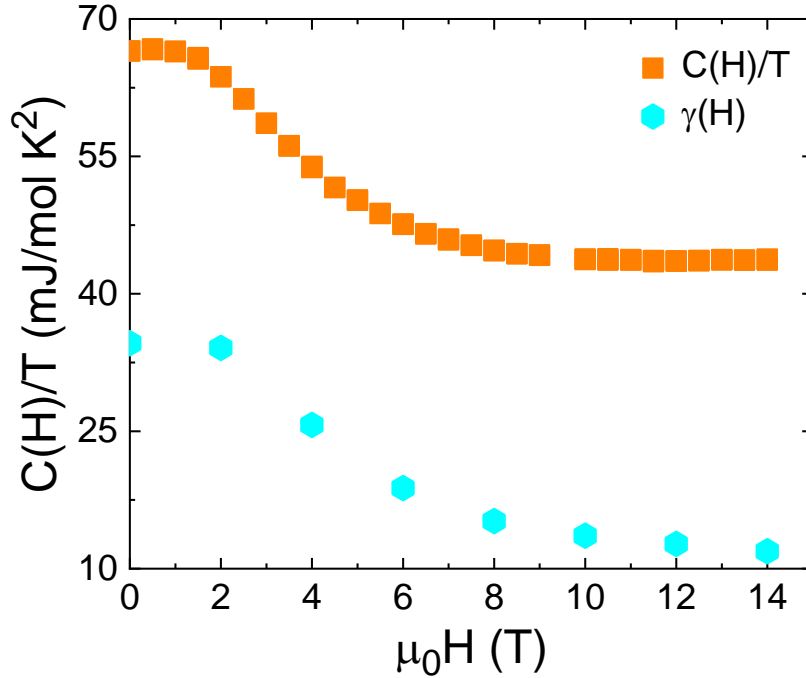


Figure 3.31: The specific heat over temperature and linear specific heat coefficient versus field for $\text{Pr}_{0.5}\text{Ir}_4\text{Sb}_{10.2}\text{Sn}_{1.8}$.

between this fit and the previous fit on a larger temperature range (86 mJ/mol K^2). This is likely due to the complications in the specific heat presented by a Kondo resonance peak and potential Einstein mode, which can give varying results over different temperature ranges. Both fits show an enhanced electron correlations through the value found for γ , however they are both close to the lower limit defined for a heavy fermion compound. This exhaustive analysis on the specific heat of the filled skutterudite shows that the filling of Pr within IrSb_3 results in weak, but apparent Kondo-alloy effects; much like those seen in other Pr based filled skutterudites. Unfortunately, the superconductivity found in this material could not be analyzed through the specific heat to determine the gap structure due to the relatively small peak expected from the transition.

3.2.4 Resistivity

Figure 3.32 is a plot of the low temperature resistivity of sample 21.1. From $10 \text{ K} \leq T \leq 60 \text{ K}$, the temperature dependence of the resistivity closely follows that of a Fermi

liquid, while at lower temperatures there is a minimum. To model this behavior, it is assumed the resistivity for $4.2 \text{ K} \leq T \leq 60 \text{ K}$ takes the form

$$\rho(T) = \rho_0 + AT^2 + c_K \ln(T), \quad (3.7)$$

The first term ρ_0 is due to electron scattering on defects and impurities in the lattice, also known as the residual resistivity. The next term with T^2 dependence models the metallic electron-electron scattering. The low temperature upturn that is likely due to Kondo scattering is accounted for by the term with logarithmic T dependence [115]. The result of the fit gives $\rho_0 = 397 \mu\Omega\text{cm}$, $A = 0.0092 \mu\Omega\text{cm}/\text{K}^2$, and $c_K = -4.6 \mu\Omega\text{cm}$. Similar large values for the residual resistivity ρ_0 have been observed in Pr and Ce based Kondo materials [115,130]. As mentioned in the previous chapter, many heavy fermion systems have been found to closely follow the Kadowaki-Woods ratio $A/\gamma^2 \approx 10^{-5} \mu\Omega\text{cm}(\text{mol K}/\text{mJ})^2$. The value for A found in this analysis as well as the value found for the linear specific heat coefficient at low temperatures ($\gamma = 29.4 \text{ mJ}/\text{mol K}^2$) results in a ratio of $A/\gamma^2 = 1.06 \times 10^{-5} \mu\Omega\text{cm}(\text{mol K}/\text{mJ})^2$. This is consistent with the expected value for a heavy fermion system. The minimum in the resistivity at $T = 10.3 \text{ K}$ that is followed by a logarithmic increase in ρ is indicative of incoherent Kondo

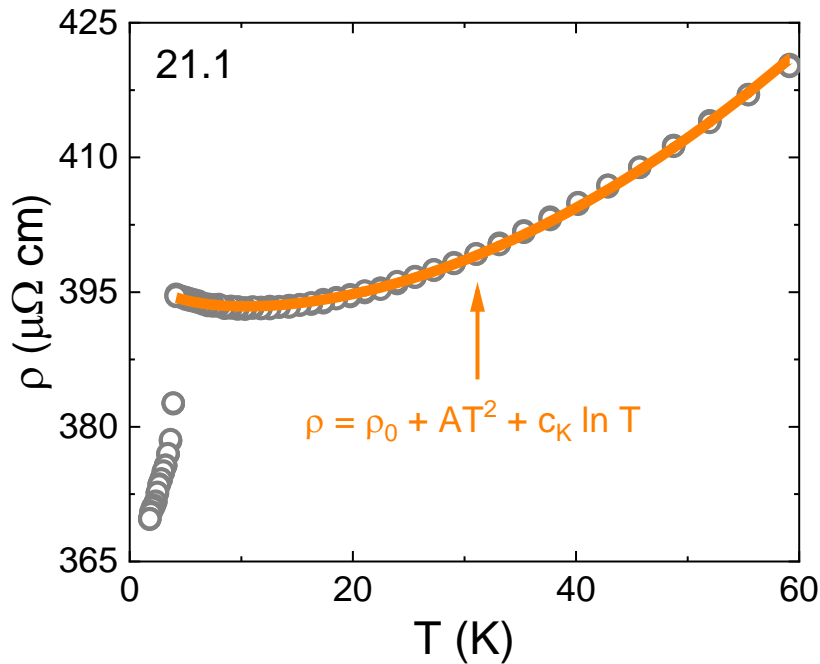


Figure 3.32: The low temperature resistivity for sample 21.1 of $\text{Pr}_{0.5}\text{Ir}_4\text{Sb}_{10.2}\text{Sn}_{1.8}$.

scattering. The fit for the logarithmic term produces a value of $c_K = -4.6 \mu\Omega cm$, which is comparable to other heavy fermion systems that show Kondo scattering at low temperatures [115,131,132].

As the resistivity continues to increase logarithmically as the temperature decreases, there is a sudden drop in the resistivity at $T \approx 4.2 K$. This is consistent with the diamagnetic signal seen in the magnetization at approximately the same temperature that suggests only a small fraction of the volume is superconducting, as the resistivity does not go to zero. This means that normal state carriers are still dominant and coexist with a fractional amount of superconducting Cooper pairs. There are many different behaviors found in several other measured samples when looking below the superconducting transition. The resistivity in that region is depicted in Fig. 3.33 for 5 samples from two different batches. Samples 64.1 and 64.2 are both in the Kondo impurity regime to the lowest temperatures measured, as there both continue in a logarithmic fashion as the temperature is lowered. The former does not have a transition in the resistivity while the latter has one of the larger drops in resistivity. The largest drop in resistivity is from sample 21.1, which is then followed by a weak temperature dependence as the resistivity gradually drops. The temperature dependence of 21.2 is nearly constant below the transition,

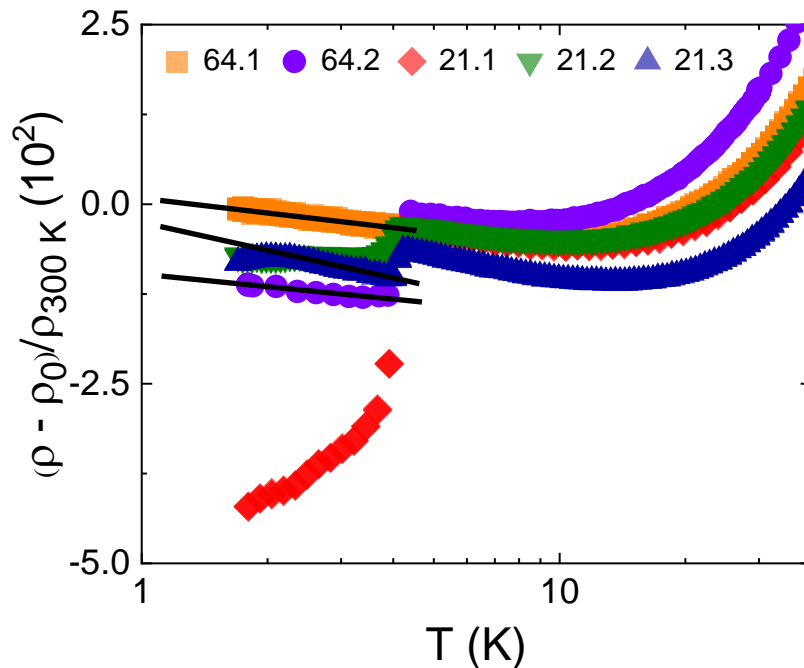


Figure 3.33: The low temperature resistivity of 5 samples of $Pr_{0.5}Ir_4Sb_{10.2}Sn_{1.8}$ in a logarithmic temperature scale.

with a hint of a maximum near 3 K. Sample 21.3 has a logarithmic dependence below 4 K and has a maximum at 2 K. An argument towards this contrasting behavior is that the Kondo temperature and superconducting fractions vary between the samples. There is likely a range of occupancy fractions for Pr ions and the distribution of Sn atoms on Sb sites may not be consistent. This may result in lattice parameter changes, as well as differences in the local density of states for the f-electrons. This could result in the strength of the super-exchange interaction J and the Kondo temperature T_K to change from sample to sample [133].

The complexities seen in the behavior below the transition is likely from an interplay between the superconducting fraction properties, the Kondo temperature, and the spin-flip scattering probability. As this material is only partially filled, it is expected to have a resistance that saturates at temperatures below T_K . When the magnetic moments become completely screened, they form spinless elastic scattering centers that cause the resistivity to become constant. An example of this can be seen in the resistivity of $\text{Ce}_x\text{La}_{1-x}\text{Cu}_6$. When the Ce atoms completely replace La ($x = 1$) the material shows coherent Kondo scattering. When the Ce concentrations are given by $x \leq 0.9$, then the resistivity becomes constant at temperatures below T_K [134]. This means that any strongly field dependent drop in the resistivity can be attributed to the superconducting portion of the crystal. As shown in the specific heat, the suppression of the Kondo effect requires a field of approximately $5 T$, which is much higher than fields needed to effect the magnetoresistance.

To explore the superconductivity a bit further, the magnetoresistance versus field plots are shown in Fig. 3.34 in proximity of the transition. Rather than a smooth and steep transition, there are many kinks within the curves at the lowest temperatures. Evidence of this can be seen in Fig 3.35, a graph of the differential resistivity versus magnetic field. Below the upper critical field value for each temperature, there is a steep decrease in resistivity, which then becomes a shallow tail in the low fields.

In zero field, the transition follows a similar trend with an initial steep drop and low temperature tail. As Ref. [135] has proposed for $\text{Ba}_{0.07}\text{K}_{0.93}\text{Fe}_2\text{As}_2$, this may be due to multiple areas within the sample that have varying critical fields and temperatures. In contrast to this, Fig. 3.36 shows the magnetoresistance of sample 64.2, an example of more homogenous behavior. This sample shows Kondo scattering below the transition, all the way to $1.8 K$. There is also no

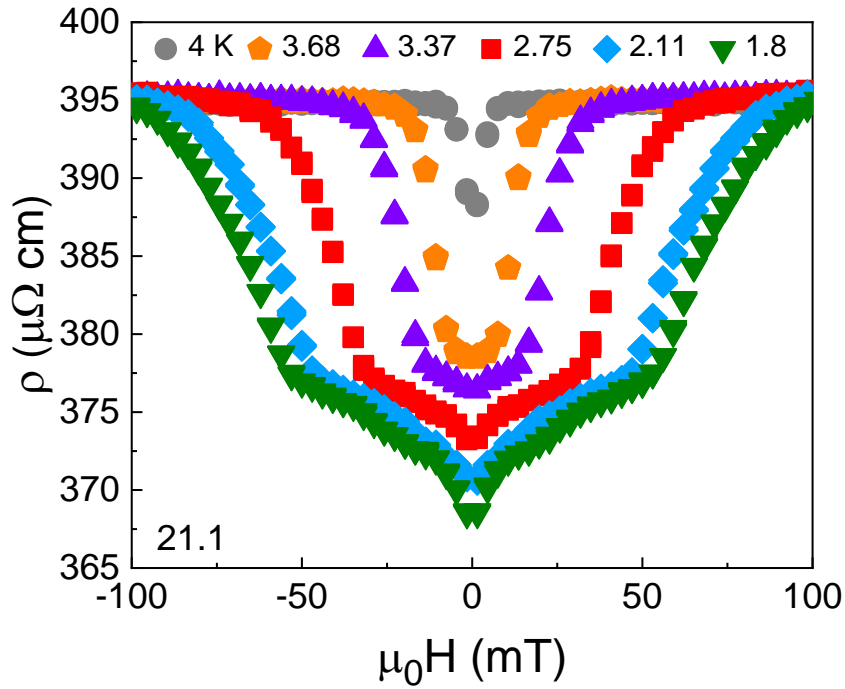


Figure 3.34: Superconducting transitions in the magnetoresistance of sample 21.1 of $\text{Pr}_{0.5}\text{Ir}_4\text{Sb}_{10.2}\text{Sn}_{1.8}$.

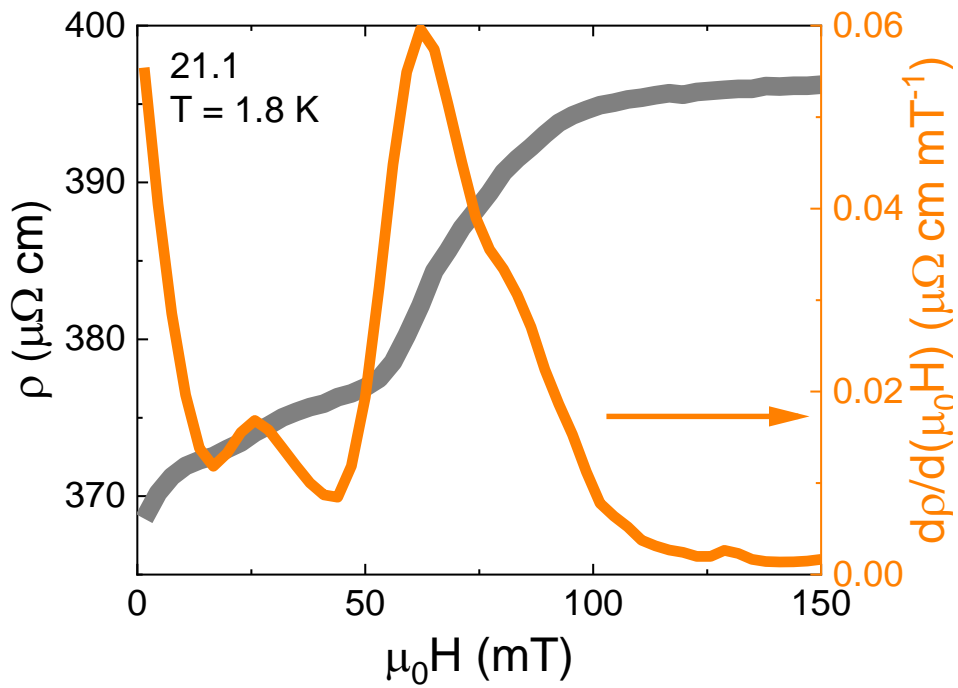


Figure 3.35: Superconducting transition at 1.8 K (left axis) and corresponding derivative with respect to field for sample 21.1 of $\text{Pr}_{0.5}\text{Ir}_4\text{Sb}_{10.2}\text{Sn}_{1.8}$.

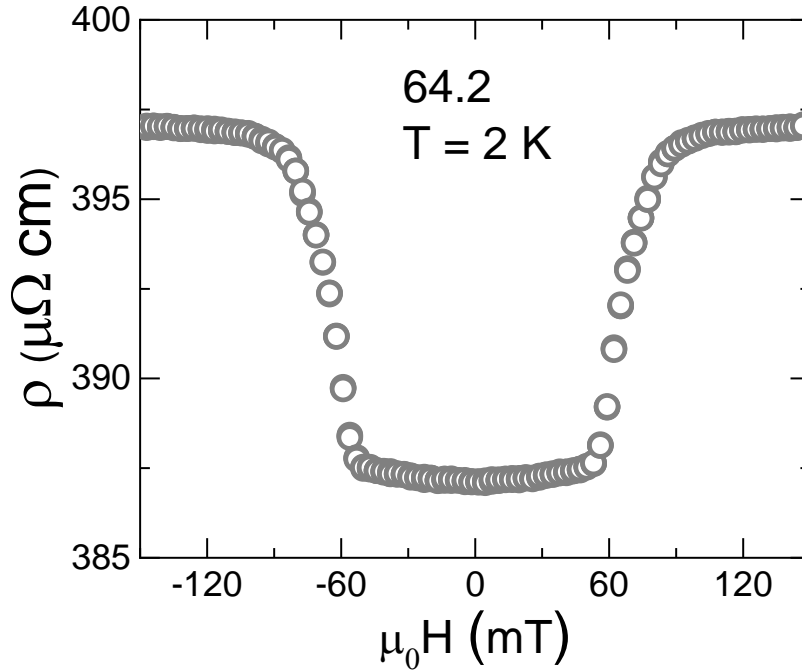


Figure 3.36: Superconducting transition at 2 K of sample 64.2 of $\text{Pr}_{0.5}\text{Ir}_4\text{Sb}_{10.2}\text{Sn}_{1.8}$.

low temperature tail below the initial transition and accordingly, there is little field dependence in the magnetoresistance until the assumed H_{c2} at that temperature. One possible explanation is that there is more than one macroscopic superconducting domain in sample 21.1 while sample 64.2 has a single homogenous superconducting domain. A bit of evidence towards this claim lies in the RRR calculated for each sample. Sample 64.2 has a larger RRR of 1.97, while sample 21.1 is equal to 1.65. A larger value is expected for a more homogenous sample that is closer to a perfect crystal.

One other possibility should be mentioned because of the extremely small fraction of superconducting material. The broad transitions with multiple kinks that are been observed in the magnetoresistance may be due to effects of reduced dimensionality of the superconductivity. It has been previously reported that superconductivity of 1 or 2 dimensions is affected more greatly by thermal fluctuations of the superconducting order parameter [136]. These fluctuations can greatly influence the temperature at which zero resistance is reached [137]. Surface superconductivity with similar properties, such as nonzero resistance, has also been previously observed in the Weyl semimetal TaIrTe_4 [138]. Further work is necessary to determine the dimensionality and origin of superconductivity found in these samples.

This extensive analysis of the resistivity has given a great amount of evidence towards the heavy fermion behavior of $\text{Pr}_{0.5}\text{Ir}_4\text{Sb}_{10.2}\text{Sn}_{1.8}$. By adding in Pr ions into the interstitial spaces of IrSb_3 , as well as the necessary substitution of Sn on Sb sites, the resistivity is dominated by Kondo correlations at low temperatures. As this material is only partially filled, it falls into the Kondo impurity regime where one observes a logarithmic correction to the resistivity at temperatures below the characteristic temperature T_K . The value found for the Fermi liquid coefficient A is enhanced from the value found for its unfilled genesis IrSb_3 and also confirms heavy fermion behavior through its agreement with the Kadowaki-Woods ratio. The origin of the superconductivity that was observed in the resistivity and magnetization is still unconfirmed. One potential way to look into this would be to systematically decrease one dimension of the crystal at a time and track the fractional superconducting volume. Another quick measurement check would be to powder the sample and take magnetic susceptibility measurements again. If the superconductivity is intrinsic and only occurs along 1D edges or 2D surfaces, then the superconducting fraction would increase as the powdered sample will have a larger surface to bulk ratio.

4 CONCLUSION

In this study I have made a direct comparison between single crystal IrSb₃ and a new filled version of this material, Pr_{0.5}Ir₄Sb_{10.2}Sn_{1.8}. I detail the growth methods as well as structure and composition determinations based upon PXRD and SEM/EDS measurements. Then, through careful low temperature specific heat, electrical transport, and magnetization measurements, I track the physical effects of filling IrSb₃ with a rare earth ion as well as Sn to electrically compensate. Unexpected behavior is found within IrSb₃ single crystal resistivity measurements that gives evidence towards its true band structure and topological nature. Heavy fermion behavior as well as a small superconducting fraction is observed in the filled version and is confirmed through its extensive physical characterization.

It has been shown in this study that single crystal IrSb₃ has very different properties than was previously reported in polycrystalline samples and past first principle calculations. Several samples from the same growth batch show metallic resistivity, with the highest quality crystal observed to have an extremely small residual resistivity $\rho_0 = 3.56 \mu\Omega cm$ and large residual resistivity ratio of approximately 40. There were also samples in the same growth that have the expected semiconducting behavior. This large variance in resistive behavior is likely due to a compositional gradient formed in the growth process. As they were grown in a horizontal configuration under a heat gradient, it is highly likely that certain growth areas have varying relative concentrations of Ir to Sb. EDS measurements give some evidence to this claim, however the differences in concentration are within the experimental error tolerance. The semiconducting samples show a crossover from activation behavior to 3D Mott VRH insulating resistivity as the temperature decreases and then saturates at the lowest temperatures. Transport characteristics that are common to topologically non-trivial semimetals were observed in one of the samples. The relativistic nature of topological semimetals and the Dirac/Weyl fermions that they host are thought to be responsible for extremely large magnetoresistance, ultrahigh mobility, small effective mass, and a non-trivial Berry phase that can produce WAL effects. Electron-hole compensation has been used as a potential explanation for the large non-saturating MR observed

in many topological semimetals, however hall measurements show this isn't the case for many of these materials. There have also been proposals of a topological mechanism that protects against backscattering that is suppressed with the application of magnetic field [139]. Further studies are currently underway with a focus on the topological nature of the band structure of IrSb₃ and the transport characteristics that result.

Upon partial filling of the cage-like voids in Pr_{0.5}Ir₄Sb_{10.2}Sn_{1.8}, many changes are observed in magnetization, specific heat, and resistivity. The diamagnetic temperature independent magnetization of IrSb₃ becomes paramagnetic due to the highly localized unfilled f-shell of the Pr filler ions. The calculated effective moment of the Pr ions is reduced from that expected for a free Pr³⁺ ion, likely due to Kondo effects present or mixed valency. A small but steep diamagnetic response appears in the low temperature magnetization. Hysteresis curves as well as the comparison ZFC and FC data point to a small fraction of material (<0.5%) displaying type 2 superconductivity. An impurity phase of Sb doped Sn was first considered as the origin of the superconductivity, however the transition temperatures and critical field values do not match the reported values in the literature, and no evidence of an impurity phase was detected in the PXRD patterns.

An extensive analysis on the specific heat of Pr_{0.5}Ir₄Sb_{10.2}Sn_{1.8} highlights the effects of a rare earth filler ion. To model the lattice contribution properly, an Einstein mode from the rattling of Pr ions in their oversized cages had to be accounted for. The Debye contribution also increased from the unfilled IrSb₃. Fits to the low temperature specific heat that included the adapted lattice model show an enhanced linear contribution ($\gamma = 86 \text{ mJ/mol K}^2$), which was the first indication of heavy fermion behavior. The linear coefficient found for IrSb₃ is approximately 4500 times smaller. This shows the large increase in the effective mass of the quasiparticles of the filled versus the unfilled version. A strongly field dependent portion of the specific heat is pushed to higher temperatures with increasing field, as one would expect from Kondo correlations. The low temperature entropy is also reduced from that of a ground state doublet. When conduction electrons completely screen the local moments, an inert Kondo singlet is expected to form. Most reported Pr based skutterudites have a ground state of at least two-fold degeneracy (the ground state degeneracy of this system is currently unknown); thus the reduced entropy is another sign of Kondo correlations. In depth analysis of the nuclear contribution to the specific heat and its dependence on field strength shows the destruction of the Kondo effect with

large field values. There is a sharp increase in the implied value of the magnetic moment that eventually saturates with field. The field dependence of the electronic specific heat also agrees closely with the previously mentioned analysis.

Adding Pr^{3+} ions within the skutterudite lattice also results in extreme changes to the resistive behavior. Graphs of the resistivity show a logarithmic upturn at low temperatures, a behavior resulting from Kondo scattering between the conduction electrons and 4f moments of Pr ions. The Fermi liquid coefficient A extracted from the low temperature resistivity as well as the linear specific coefficient follow the Kadowaki-Woods ratio

$A/\gamma^2 \approx 10^{-5} \mu\Omega\text{cm}(\text{mol K}/\text{mJ})^2$. The value for A is also larger than that of its unfilled genesis, another effect of strong electron correlations.

When the temperature reaches 4.2 K, there is a small drop in the resistivity; one that coincides well with the diamagnetic transition found in the magnetization. The fact that the resistivity does not quite reach zero is also consistent with only a small fraction of the material going superconducting, while other non-superconducting bulk carriers are still contributing to the resistivity. Multiple peaks in the differential magnetoresistivity versus magnetic field plots point towards a few potential situations in the superconducting behavior of this material. There may be nonhomogeneous samples with multiple superconducting domains with varying critical field values. Superconductivity of reduced dimensionality can also show similar broad and kinked transitions. More work needs to be done on the analysis of the superconducting behavior to determine if it is indeed intrinsic to the material.

From careful self-flux and horizontal flux transport growth techniques, I have created IrSb_3 with never before reported low temperature properties as well as a new filled version of this Skutterudite, $\text{Pr}_{0.5}\text{Ir}_4\text{Sb}_{10.2}\text{Sn}_{1.8}$. I have demonstrated through a comprehensive low temperature physical characterization using specific heat, electron transport, and magnetization measurements, that partial filling of IrSb_3 with Pr ions results in Kondo-alloy behavior. This filled material also becomes superconducting at low temperatures and may host interesting superconducting properties, like the related material $\text{PrOs}_4\text{Sb}_{12}$. The small superconducting fraction may be from inhomogeneous samples or be of reduced dimensionality. An impurity phase has not been completely ruled out; current evidence however does not support this claim. I am interested to plan future work to discover if the superconductivity is indeed intrinsic to the material. One straightforward method with the characterization methods found in this work

would be to systematically decrease one of the dimensions of the crystal and track the effects on the superconducting fraction. This may give evidence towards surface, filamentary, or impurity superconductivity.

REFERENCES

- [1] B. Yan and S.-C. Zhang, *Topological Materials*, Rep. Prog. Phys. **75**, 096501 (2012).
- [2] K. Wang, F. Boschini, B. J. Ramshaw, D. Graf, L. Wang, M. Michiardi, A. Zonno, E. Rotenberg, A. Bostwick, A. Damascelli, and J. Paglione, *Dirac Dispersion and Non-Trivial Berry's Phase in Three-Dimensional Semimetal RhSb₃*, ArXiv:1703.04673 [Cond-Mat] (2017).
- [3] M. Yang and W.-M. Liu, *The d-p Band-Inversion Topological Insulator in Bismuth-Based Skutterudites*, Sci Rep **4**, 5131 (2015).
- [4] J. C. Smith, S. Banerjee, V. Pardo, and W. E. Pickett, *Dirac Point Degenerate with Massive Bands at a Topological Quantum Critical Point*, Phys. Rev. Lett. **106**, 056401 (2011).
- [5] R. E. Baumbach and M. B. Maple, *Filled Skutterudites: Magnetic and Electrical Transport Properties*, in *Encyclopedia of Materials: Science and Technology* (Elsevier, 2010), pp. 1–6.
- [6] D. Cao, F. Bridges, P. Chesler, S. Bushart, E. D. Bauer, and M. B. Maple, *Evidence for Rattling Behavior of the Filler Atom (L) in the Filled Skutterudites LT₄X₁₂ (L=Ce, Eu, Yb; T=Fe, Ru ; X=P, Sb) from EXAFS Studies*, Phys. Rev. B **70**, 9 (2004).
- [7] K. H. J. Buschow, editor , *Encyclopedia of Materials: Science and Technology* (Elsevier, Amsterdam ; New York, 2001).
- [8] G. Rogl and P. Rogl, *Skutterudites, a Most Promising Group of Thermoelectric Materials*, Current Opinion in Green and Sustainable Chemistry **4**, 50 (2017).
- [9] J.-Y. Cho, M. Siyar, W. C. Jin, E. Hwang, S.-H. Bae, S.-H. Hong, M. Kim, and C. Park, *Electrical Transport and Thermoelectric Properties of SnSe–SnTe Solid Solution*, Materials **12**, 3854 (2019).
- [10] Z. Liu, X. Yang, G. Chen, and P. Zhai, *Molecular Dynamics Study of the Influence of Sb-Vacancy Defects on the Lattice Thermal Conductivity of Crystalline CoSb₃*, Computational Materials Science **124**, 403 (2016).
- [11] G. Rogl, A. Grytsiv, P. Rogl, E. Bauer, and M. Zehetbauer, *A New Generation of P-Type Didymium Skutterudites with High ZT*, Intermetallics **19**, 4 (2011).
- [12] G. Rogl, A. Grytsiv, F. Failamani, M. Hoehenhofer, E. Bauer, and P. Rogl, *Attempts to Further Enhance ZT in Skutterudites via Nano-Composites*, Journal of Alloys and Compounds **695**, 682 (2017).
- [13] T. Dahal, Q. Jie, W. Liu, K. Dahal, C. Guo, Y. Lan, and Z. Ren, *Effect of Triple Fillers in Thermoelectric Performance of P-Type Skutterudites*, Journal of Alloys and Compounds **623**, 104 (2015).
- [14] X. Shi, J. Yang, J. R. Salvador, M. Chi, J. Y. Cho, H. Wang, S. Bai, J. Yang, W. Zhang, and L. Chen, *Multiple-Filled Skutterudites: High Thermoelectric Figure of Merit through Separately Optimizing Electrical and Thermal Transports*, J. Am. Chem. Soc. **133**, 20 (2011).

- [15] H. Sugawara, T. D. Matsuda, K. Abe, Y. Aoki, H. Sato, S. Nojiri, Y. Inada, R. Settai, and Y. Ōnuki, *Exotic Heavy-Fermion State in the Filled Skutterudite $\text{PrFe}_4\text{P}_{12}$ Uncovered by the de Haas–van Alphen Effect*, Phys. Rev. B **66**, 134411 (2002).
- [16] S. Sanada, Y. Aoki, H. Aoki, A. Tsuchiya, D. Kikuchi, H. Sugawara, and H. Sato, *Exotic Heavy-Fermion State in Filled Skutterudite $\text{SmOs}_4\text{Sb}_{12}$* , J. Phys. Soc. Jpn. **74**, 246 (2005).
- [17] Y. Aoki, T. Namiki, T. D. Matsuda, K. Abe, H. Sugawara, and H. Sato, *Anomalous Heavy-Fermion and Ordered States in the Filled Skutterudite $\text{PrFe}_4\text{P}_{12}$* , Phys. Rev. B **65**, 064446 (2002).
- [18] D. A. Gajewski, N. R. Dilley, E. D. Bauer, E. J. Freeman, R. Chau, M. B. Maple, D. Mandrus, B. C. Sales, and A. H. Lacerda, *Heavy Fermion Behaviour of the Cerium-Filled Skutterudites Ce_2CoSb_6 and Ce_2NiSb_6* , Journal of Physics: Condensed Matter **10**, 6973 (1998).
- [19] M. Kohgi, K. Iwasa, M. Nakajima, N. Metoki, S. Araki, N. Bernhoeft, J.-M. Mignot, A. Gukasov, H. Sato, Y. Aoki, and H. Sugawara, *Evidence for Magnetic-Field-Induced Quadrupolar Ordering in the Heavy-Fermion Superconductor $\text{PrOs}_4\text{Sb}_{12}$* , J. Phys. Soc. Jpn. **72**, 1002 (2003).
- [20] J. Kikuchi, M. Takigawa, Hitoshi Sugawara, and H. Sato, *Quadrupole Order and Field-Induced Heavy-Fermion State in the Filled Skutterudite via ^1P NMR*, Physica B: Condensed Matter **359–361**, 877 (2005).
- [21] R. E. Baumbach, P. C. Ho, T. A. Sayles, M. B. Maple, R. Wawryk, T. Cichorek, A. Pietraszko, and Z. Henkie, *Non-Fermi Liquid Behavior in the Filled Skutterudite Compound $\text{CeRu}_4\text{As}_{12}$* , Journal of Physics: Condensed Matter **20**, 075110 (2008).
- [22] M. Nicklas, S. Kirchner, R. Borth, R. Gumeniuk, W. Schnelle, H. Rosner, H. Borrmann, A. Leithe-Jasper, Yu. Grin, and F. Steglich, *Charge-Doping-Driven Evolution of Magnetism and Non-Fermi-Liquid Behavior in the Filled Skutterudite $\text{CePt}_4\text{Ge}_{12-x}\text{Sb}_x$* , Phys. Rev. Lett. **109**, 236405 (2012).
- [23] C. Sekine, T. Uchiumi, I. Shirotni, and T. Yagi, *Metal-Insulator Transition in $\text{PrRu}_4\text{P}_{12}$ with Skutterudite Structure*, Phys. Rev. Lett. **79**, 3218 (1997).
- [24] K. Matsuhira, Y. Hinatsu, C. Sekine, T. Togashi, H. Maki, I. Shirotni, H. Kitazawa, T. Takamasu, and G. Kido, *Metal–Insulator Transition of Filled Skutterudite Compound $\text{SmRu}_4\text{P}_{12}$* , J. Phys. Soc. Jpn. **71**, 237 (2002).
- [25] B. Yan, L. Müchler, X.-L. Qi, S.-C. Zhang, and C. Felser, *Topological Insulators in Filled Skutterudites*, Phys. Rev. B **85**, 165125 (2012).
- [26] I. Shirotni, T. Uchiumi, K. Ohno, C. Sekine, Y. Nakazawa, K. Kanoda, S. Todo, and T. Yagi, *Superconductivity of Filled Skutterudites $\text{LaRu}_4\text{As}_{12}$ and $\text{PrRu}_4\text{As}_{12}$* , Phys. Rev. B **56**, 7866 (1997).
- [27] E. Bauer, A. Grytsiv, X.-Q. Chen, N. Melnychenko-Koblyuk, G. Hilscher, H. Kaldarar, H. Michor, E. Royanian, G. Giester, M. Rotter, R. Podloucky, and P. Rogl, *Superconductivity in Novel Ge-Based Skutterudites: $\{\text{Sr}, \text{Ba}\}\text{Pt}_4\text{Ge}_{12}$* , Phys. Rev. Lett. **99**, 217001 (2007).
- [28] E. D. Bauer, N. A. Frederick, P.-C. Ho, V. S. Zapf, and M. B. Maple, *Superconductivity and Heavy Fermion Behavior in $\text{PrOs}_4\text{Sb}_{12}$* , Phys. Rev. B **65**, 100506 (2002).
- [29] Y. Aoki, A. Tsuchiya, T. Kanayama, S. R. Saha, H. Sugawara, H. Sato, W. Higemoto, A. Koda, K. Ohishi, K. Nishiyama, and R. Kadono, *Time-Reversal Symmetry-Breaking Superconductivity in Heavy Fermion $\text{PrOs}_4\text{Sb}_{12}$ Detected by Muon Spin Relaxation*, Phys. Rev. Lett. **91**, 067003 (2003).

- [30] A. Yatskar, W. P. Beyermann, R. Movshovich, and P. C. Canfield, *Possible Correlated-Electron Behavior from Quadrupolar Fluctuations in PrInAg₂*, Phys. Rev. Lett. **77**, 3637 (1996).
- [31] Y. Aoki, T. Namiki, S. Ohsaki, S. R. Saha, H. Sugawara, and H. Sato, *Thermodynamical Study on the Heavy-Fermion Superconductor PrOs₄Sb₁₂: Evidence for Field-Induced Phase Transition*, J. Phys. Soc. Jpn. **71**, 9 (2002).
- [32] S. H. Curnoe, H. Harima, K. Takegahara, and K. Ueda, *Structural Phase Transition and Anti-Quadrupolar Ordering in PrFe₄P₁₂ and PrRu₄P₁₂*, Physica B: Condensed Matter **312–313**, 837 (2002).
- [33] H. Luo, J. W. Krizan, L. Muechler, N. Haldolaarachchige, T. Klimczuk, W. Xie, M. K. Fuccillo, C. Felser, and R. J. Cava, *A Large Family of Filled Skutterudites Stabilized by Electron Count*, Nat Commun **6**, 6489 (2015).
- [34] *Handbook on the Physics and Chemistry of Rare Earths*, Vol. chapter 211 (n.d.).
- [35] M. B. Maple, P.-C. Ho, N. A. Frederick, V. S. Zapf, W. M. Yuhasz, and E. D. Bauer, *A New Heavy Fermion Superconductor: The Filled Skutterudite Compound PrOs₄Sb₁₂*, ArXiv:Cond-Mat/0303370 (2003).
- [36] M.-A. Measson, D. Braithwaite, G. Lapertot, J.-P. Brison, P. Bordet, H. Sugawara, P. C. Canfield, and J. Flouquet, *Double Superconducting Transition in the Filled Skutterudite PrOs₄Sb₁₂ and Sample Characterizations*, Phys. Rev. B **77**, 13 (2008).
- [37] K. Miyake, H. Kohno, and H. Harima, *Theory of a New Type of Heavy-Electron Superconductivity in PrOs₄Sb₁₂: Quadrupolar-Fluctuation Mediated Odd-Parity Pairings*, J. Phys.: Condens. Matter **15**, 19 (2003).
- [38] B. Lian, X.-Q. Sun, A. Vaezi, X.-L. Qi, and S.-C. Zhang, *Topological Quantum Computation Based on Chiral Majorana Fermions*, Proc Natl Acad Sci USA **115**, 10938 (2018).
- [39] W. J. de Haas, J. de Boer, and G. J. van den Berg, *The Electrical Resistance of Gold, Copper and Lead at Low Temperatures*, Physica **1**, 1115 (1934).
- [40] P. W. Anderson, *Localized Magnetic States in Metals*, Phys. Rev. **124**, 41 (1961).
- [41] A. Blandin and J. Friedel, *Propriétés Magnétiques Des Alliages Dilués. Interactions Magnétiques et Antiferromagnétisme Dans Les Alliages Du Type Métal Noble-Métal de Transition*, J. Phys. Radium **20**, 160 (1959).
- [42] C. Zener, *Interaction Between the d Shells in the Transition Metals*, Phys. Rev. **81**, 440 (1951).
- [43] T. Kasuya, *A Theory of Metallic Ferro- and Antiferromagnetism on Zener's Model*, Prog. Theor. Phys. **16**, 45 (1956).
- [44] K. Yosida, *Magnetic Properties of Cu-Mn Alloys*, Phys. Rev. **106**, 893 (1957).
- [45] P. Coleman, *Many Body Physics: Unfinished Revolution*, Ann. Henri Poincaré **4**, 559 (2003).
- [46] N. Rivier and M. J. Zuckermann, *Equivalence of Localized Spin Fluctuations and the Kondo-Nagaoka Spin-Compensated State*, Phys. Rev. Lett. **21**, 904 (1968).
- [47] A. A. Abrikosov, *Electron Scattering on Magnetic Impurities in Metals and Anomalous Resistivity Effects*, Physics Physique Fizika **2**, 5 (1965).
- [48] H. Suhl, *Dispersion Theory of the Kondo Effect*, Phys. Rev. **138**, A515 (1965).
- [49] Y. Nagaoka, *Self-Consistent Treatment of Kondo's Effect in Dilute Alloys*, Phys. Rev. **138**, A1112 (1965).

- [50] P. Coleman, *Heavy Fermions: Electrons at the Edge of Magnetism*, ArXiv:Cond-Mat/0612006 (2007).
- [51] P. Coleman, *Heavy Fermions and the Kondo Lattice: A 21st Century Perspective*, ArXiv:1509.05769 [Cond-Mat] (2015).
- [52] D. Neilson, *Landau Fermi Liquid Theory*, Aust. J. Phys. **49**, 79 (1996).
- [53] E. Pavarini and Institute for Advanced Simulation, editors, *Correlated Electrons: From Models to Materials ; Lecture Notes of the Autumn School 2012 at Forschungszentrum Jülich 3-7 September 2012* (Forschungszentrum Jülich, Jülich, 2012).
- [54] M. A. Ruderman and C. Kittel, *Indirect Exchange Coupling of Nuclear Magnetic Moments by Conduction Electrons*, Phys. Rev. **96**, 99 (1954).
- [55] J. Kroha, *Interplay of Kondo Effect and RKKY Interaction*, ArXiv:1710.00192 [Cond-Mat] (2017).
- [56] J.-Q. Yan, B. C. Sales, M. A. Susner, and M. A. McGuire, *Flux Growth in a Horizontal Configuration: An Analog to Vapor Transport Growth*, Phys. Rev. Materials **1**, 023402 (2017).
- [57] W. M. Yuhasz, *A Study of Strongly Correlated Electron Behavior in the Filled Skutterudites*, ProQuest Dissertations and Theses 165 (2006).
- [58] E. D. Bauer, A. Slebarski, E. J. Freeman, C. Sirvent, and M. B. Maple, *Kondo Insulating Behaviour in the Filled Skutterudite Compound $CeOs_4Sb_{12}$* , J. Phys.: Condens. Matter **13**, 4495 (2001).
- [59] T. Degen, M. Sadki, E. Bron, U. König, and G. Nénert, *The HighScore Suite*, Powder Diffraction **29**, S13 (2014).
- [60] H. M. Rietveld, *A Profile Refinement Method for Nuclear and Magnetic Structures*, J Appl Crystallogr **2**, 65 (1969).
- [61] T. Fujii and I. Morimoto, *Residual Resistivity of High Purity Iron*, Jpn. J. Appl. Phys. **8**, 1154 (1969).
- [62] D. van der Marel, J. L. M. van Mechelen, and I. I. Mazin, *Common Fermi-Liquid Origin of T -Squared Resistivity and Superconductivity in n -Type $SrTiO_3$* , Phys. Rev. B **84**, 205111 (2011).
- [63] F. Bloch, *Über die Quantenmechanik der Elektronen in Kristallgittern*, Z. Physik **52**, 555 (1929).
- [64] Quantum Design, *Vibrating Sample Magnetometer (VSM) Option User's Manual, 1096-100, Rev. B0*.
- [65] C. Kittel, *Introduction to Solid State Physics*, 8th ed (Wiley, Hoboken, NJ, 2005).
- [66] R. Mondal, R. Bapat, S. K. Dhar, and A. Thamizhavel, *Magnetocrystalline Anisotropy in the Kondo-Lattice Compound $CeAgAs_2$* , Phys. Rev. B **98**, 115160 (2018).
- [67] Quantum Design, *PPMS Heat Capacity Option User's Manual, 1085-150, Rev. M7*.
- [68] J. M. Schliesser and B. F. Woodfield, *Development of a Debye Heat Capacity Model for Vibrational Modes with a Gap in the Density of States*, J. Phys.: Condens. Matter **27**, 285402 (2015).
- [69] M. Mizumaki, S. Tsutsui, T. Uruga, H. Tanida, D. Kikuchi, H. Sugawara, and H. Sato, *Rare Earth Dependence of Einstein Temperatures in Filled Skutterudite Compounds $REFe_4P_{12}$ ($RE = La, Ce, Pr, Nd, \text{ and } Sm$)*, J. Phys. Soc. Jpn. **80**, 074603 (2011).
- [70] G. A. Bain and J. F. Berry, *Diamagnetic Corrections and Pascal's Constants*, J. Chem. Educ. **85**, 532 (2008).

- [71] T. Suzuki, A. Kikkawa, Y. Tokura, and Y. Taguchi, *Impact of Electron Doping on Thermoelectric Properties in Filled Skutterudite IrSb₃*, Phys. Rev. B **93**, 155101 (2016).
- [72] Y. Yin, Y. Huang, Y. Wu, G. Chen, W.-J. Yin, S.-H. Wei, and X. Gong, *Exploring Emerging Photovoltaic Materials Beyond Perovskite: The Case of Skutterudite*, Chem. Mater. **29**, 9429 (2017).
- [73] W. Li and N. Mingo, *Lattice Dynamics and Thermal Conductivity of Skutterudites CoSb₃ and IrSb₃ from First Principles: Why IrSb₃ Is a Better Thermal Conductor than CoSb₃*, Phys. Rev. B **90**, 094302 (2014).
- [74] D. W. Song, W. L. Liu, T. Zeng, T. Borca-Tasciuc, G. Chen, J. C. Caylor, and T. D. Sands, *Thermal Conductivity of Skutterudite Thin Films and Superlattices*, Appl. Phys. Lett. **77**, 3854 (2000).
- [75] T. Caillat, A. Borshchevsky, and J.-P. Fleurial, *Preparation and Thermoelectric Properties of P- and n-Type IrSb₃*, in *AIP Conference Proceedings*, Vol. 316 (AIP, Kansas City, Missouri (USA), 1994), pp. 31–34.
- [76] T. M. Tritt, G. S. Nolas, G. A. Slack, A. C. Ehrlich, D. J. Gillespie, and J. L. Cohn, *Low-temperature Transport Properties of the Filled and Unfilled IrSb₃ Skutterudite System*, Journal of Applied Physics **79**, 8412 (1996).
- [77] X. Yang, Z. Dai, Y. Zhao, W. Niu, J. Liu, and S. Meng, *Pressure Induced Excellent Thermoelectric Behavior in Skutterudites CoSb₃ and IrSb₃*, Phys. Chem. Chem. Phys. **21**, 851 (2019).
- [78] D. J. Singh and W. E. Pickett, *Skutterudite Antimonides: Quasilinear Bands and Unusual Transport*, Phys. Rev. B **50**, 11235 (1994).
- [79] K. Koga, K. Akai, K. Oshiro, and M. Matsuura, *Electronic Structure and Optical Properties of Binary Skutterudite Antimonides*, Phys. Rev. B **71**, 155119 (2005).
- [80] T. Liang, Q. Gibson, M. N. Ali, M. Liu, R. J. Cava, and N. P. Ong, *Ultra-high Mobility and Giant Magnetoresistance in the Dirac Semimetal Cd₃As₂*, Nature Mater **14**, 280 (2015).
- [81] R. K. Gopal, S. Singh, A. Mandal, J. Sarkar, and C. Mitra, *Topological Delocalization and Tuning of Surface Channel Separation in Bi₂Se₂Te Topological Insulator Thin Films*, Sci Rep **7**, 4924 (2017).
- [82] P. Dutta, A. Pariari, and P. Mandal, *Prominent Metallic Surface Conduction and the Singular Magnetic Response of Topological Dirac Fermion in Three-Dimensional Topological Insulator Bi_{1.5}Sb_{0.5}Te_{1.7}Se_{1.3}*, Sci Rep **7**, 4883 (2017).
- [83] A. Gharleghi, Y.-H. Pai, F.-H. Lin, and C.-J. Liu, *Low Thermal Conductivity and Rapid Synthesis of N-Type Cobalt Skutterudite via a Hydrothermal Method*, J. Mater. Chem. C **2**, 4213 (2014).
- [84] M. Jenderka, J. Barzola-Quiquia, Z. Zhang, H. Frenzel, M. Grundmann, and M. Lorenz, *Mott Variable Range Hopping and Weak Antilocalization Effect in Heteroepitaxial Na₂IrO₃ Thin Films*, Phys. Rev. B **88**, 045111 (2013).
- [85] G. Xu, W. Wang, X. Zhang, Y. Du, E. Liu, S. Wang, G. Wu, Z. Liu, and X. X. Zhang, *Weak Antilocalization Effect and Noncentrosymmetric Superconductivity in a Topologically Nontrivial Semimetal LuPdBi*, Sci Rep **4**, 5709 (2015).
- [86] X. Du, S.-W. Tsai, D. L. Maslov, and A. F. Hebard, *Metal-Insulator-Like Behavior in Semimetallic Bismuth and Graphite*, Phys. Rev. Lett. **94**, 166601 (2005).
- [87] X. Luo, R. C. Xiao, F. C. Chen, J. Yan, Q. L. Pei, Y. Sun, W. J. Lu, P. Tong, Z. G. Sheng, X. B. Zhu, W. H. Song, and Y. P. Sun, *Origin of the Extremely Large Magnetoresistance in Topological Semimetal PtSn₄*, Phys. Rev. B **97**, 205132 (2018).

- [88] M. N. Ali, J. Xiong, S. Flynn, J. Tao, Q. D. Gibson, L. M. Schoop, T. Liang, N. Haldolaarachchige, M. Hirschberger, N. P. Ong, and R. J. Cava, *Large, Non-Saturating Magnetoresistance in WTe_2* , Nature **514**, 205 (2014).
- [89] Y. Kopelevich, J. H. S. Torres, R. R. da Silva, F. Mrowka, H. Kempa, and P. Esquinazi, *Reentrant Metallic Behavior of Graphite in the Quantum Limit*, Phys. Rev. Lett. **90**, 156402 (2003).
- [90] F. Tang, H. C. Po, A. Vishwanath, and X. Wan, *Topological Materials Discovery by Large-Order Symmetry Indicators*, Sci. Adv. **5**, eaau8725 (2019).
- [91] F. Schindler, Z. Wang, M. G. Vergniory, A. M. Cook, A. Murani, S. Sengupta, A. Yu. Kasumov, R. Deblock, S. Jeon, I. Drozdov, H. Bouchiat, S. Guéron, A. Yazdani, B. A. Bernevig, and T. Neupert, *Higher-Order Topology in Bismuth*, Nature Phys **14**, 918 (2018).
- [92] N. Kumar, Y. Sun, N. Xu, K. Manna, M. Yao, V. Süß, I. Leermakers, O. Young, T. Förster, M. Schmidt, H. Borrmann, B. Yan, U. Zeitler, M. Shi, C. Felser, and C. Shekhar, *Extremely High Magnetoresistance and Conductivity in the Type-II Weyl Semimetals WP_2 and MoP_2* , Nat Commun **8**, 1642 (2017).
- [93] X. Huang, L. Zhao, Y. Long, P. Wang, D. Chen, Z. Yang, H. Liang, M. Xue, H. Weng, Z. Fang, X. Dai, and G. Chen, *Observation of the Chiral-Anomaly-Induced Negative Magnetoresistance in 3D Weyl Semimetal TaAs*, Phys. Rev. X **5**, 031023 (2015).
- [94] S. Singh, V. Süß, M. Schmidt, C. Felser, and C. Shekhar, *Strong Correlation between Mobility and Magnetoresistance in Weyl and Dirac Semimetals*, J. Phys. Mater. **3**, 024003 (2020).
- [95] H.-Z. Lu and S.-Q. Shen, *Weak Localization and Weak Anti-Localization in Topological Insulators*, ArXiv:1409.1299 [Cond-Mat] 91672E (2014).
- [96] T. Zhang, J. Pan, and P. Sheng, *Berry Phase Induced Localization to Anti-Localization Transition in Two-Dimensional Dirac Fermion Systems*, ArXiv:1710.10907 [Cond-Mat] (2017).
- [97] V. Pardo, J. C. Smith, and W. E. Pickett, *Linear Bands, Zero-Momentum Weyl Semimetal, and Topological Transition in Skutterudite-Structure Pnictides*, Phys. Rev. B **85**, 214531 (2012).
- [98] B. Bradlyn, L. Elcoro, J. Cano, M. G. Vergniory, Z. Wang, C. Felser, M. I. Aroyo, and B. A. Bernevig, *Topological Quantum Chemistry*, Nature **547**, 298 (2017).
- [99] M. G. Vergniory, L. Elcoro, C. Felser, N. Regnault, B. A. Bernevig, and Z. Wang, *A Complete Catalogue of High-Quality Topological Materials*, Nature **566**, 480 (2019).
- [100] S. W. Kim, Y. Kimura, and Y. Mishima, *Effects of Doping on the High-Temperature Thermoelectric Properties of $IrSb_3$ Skutterudite Compounds*, Journal of Electronic Materials **32**, 1141 (2003).
- [101] G. A. Slack and V. G. Tsoukala, *Some Properties of Semiconducting $IrSb_3$* , Journal of Applied Physics **76**, 1665 (1994).
- [102] M. Koshigoe, I. Shiota, Y. Shinohara, Y. Imai, and I. A. Nishida, *Preparation and Thermoelectric Properties of $IrSb_3$* , in *Functionally Graded Materials 1996* (Elsevier, 1997), pp. 581–586.
- [103] S. W. Kim, Y. Kimura, and Y. Mishima, *Enhancement of High Temperature Thermoelectric Properties of Intermetallic Compounds Based on a Skutterudite $IrSb_3$ and a Half-Heusler $TiNiSb$* , Science and Technology of Advanced Materials **5**, 485 (2004).

- [104] C. Zhang, Z. Yuan, S. Xu, Z. Lin, B. Tong, M. Z. Hasan, J. Wang, C. Zhang, and S. Jia, *Tantalum Monoarsenide: An Exotic Compensated Semimetal*, Phys. Rev. B **95**, 085202 (2017).
- [105] C. Shekhar, A. K. Nayak, Y. Sun, M. Schmidt, M. Nicklas, I. Leermakers, U. Zeitler, Y. Skourski, J. Wosnitza, Z. Liu, Y. Chen, W. Schnelle, H. Borrmann, Y. Grin, C. Felser, and B. Yan, *Extremely Large Magnetoresistance and Ultrahigh Mobility in the Topological Weyl Semimetal Candidate NbP*, Nature Phys **11**, 645 (2015).
- [106] B. K. Rai, I. W. H. Oswald, W. Ban, C.-L. Huang, V. Loganathan, A. M. Hallas, M. N. Wilson, G. M. Luke, L. Harriger, Q. Huang, Y. Li, S. Dzsaber, J. Y. Chan, N. L. Wang, S. Paschen, J. W. Lynn, A. H. Nevidomskyy, P. Dai, Q. Si, and E. Morosan, *Low-Carrier Density and Fragile Magnetism in a Kondo Lattice System*, Phys. Rev. B **99**, 085120 (2019).
- [107] J. Chen, Z. Wang, S. Zheng, C. Feng, J. Dai, and Z. Xu, *Antiferromagnetic Kondo Lattice Compound CePt₃P*, Sci Rep **7**, 41853 (2017).
- [108] J. R. Clem and Z. Hao, *Theory for the Hysteretic Properties of the Low-Field Dc Magnetization in Type-II Superconductors*, Phys. Rev. B **48**, 13774 (1993).
- [109] M. Rotter, M. Tegel, and D. Johrendt, *Superconductivity at 38 K in the Iron Arsenide (Ba_{1-x}K_x)Fe₂As₂*, Phys. Rev. Lett. **101**, 107006 (2008).
- [110] V. Sandu, P. Gyawali, T. Katuwal, C. C. Almasan, B. J. Taylor, and M. B. Maple, *Magnetic Response of Y_{0.47}Pr_{0.53}Ba₂Cu₃O_{7- δ} : Superconductivity, Glassiness, and Paramagnetism*, Phys. Rev. B **74**, 184511 (2006).
- [111] M. J. Qin, H. L. Ji, X. Jin, X. X. Yao, X. S. Rong, Y. M. Ni, L. Xiao, and X. K. Fu, *Paramagnetism and Macroscopic Magnetic Properties of Single-Crystal Y_xGd_{1-x}Ba₂Cu_{2.43}Al_{0.19}O_{6+y}*, Phys. Rev. B **50**, 4086 (1994).
- [112] W. F. Love, *Superconductivity in Tin-Bismuth and Tin-Antimony Alloys*, Phys. Rev. **92**, 238 (1953).
- [113] M. B. Maple, Z. Henkie, R. E. Baumbach, T. A. Sayles, N. P. Butch, P.-C. Ho, T. Yanagisawa, W. M. Yuhasz, R. Wawryk, T. Cichorek, and A. Pietraszko, *Correlated Electron Phenomena in Ce- and Pr-Based Filled Skutterudite Arsenides and Antimonides*, J. Phys. Soc. Jpn. **77**, 7 (2008).
- [114] M. Tinkham, *Introduction to Superconductivity* (R. E. Krieger Pub. Co, Huntington, N.Y, 1980).
- [115] D. Kaczorowski and A. Ślebarski, *Kondo Lattice Behavior and Magnetic Ordering in CeRh₂Si*, Phys. Rev. B **81**, 214411 (2010).
- [116] H. Geng, X. Meng, H. Zhang, and J. Zhang, *Lattice Thermal Conductivity of Filled Skutterudites: An Anharmonicity Perspective*, Journal of Applied Physics **116**, 163503 (2014).
- [117] G. S. Nolas, G. A. Slack, D. T. Morelli, T. M. Tritt, and A. C. Ehrlich, *The Effect of Rare-Earth Filling on the Lattice Thermal Conductivity of Skutterudites*, J. Appl. Phys. **79**, 4002 (1996).
- [118] W. Li and N. Mingo, *Thermal Conductivity of Fully Filled Skutterudites: Role of the Filler*, Phys. Rev. B **89**, 184304 (2014).
- [119] T. Namiki, Y. Aoki, H. Sato, C. Sekine, I. Shirotnani, T. D. Matsuda, Y. Haga, and T. Yagi, *Superconducting Properties of Pr-Based Filled Skutterudite PrRu₄As₁₂*, J. Phys. Soc. Jpn. **76**, 093704 (2007).

- [120] S. Yadav, D. Singh, D. Venkateshwarlu, M. K. Gangrade, S. S. Samatham, and V. Ganesan, *Magneto-Heat Capacity Study on Kondo Lattice System $Ce(Ni_{1-x}Cu_x)_2Al_3$* , *Bull Mater Sci* **39**, 537 (2016).
- [121] V. K. Anand, Z. Hossain, and C. Geibel, *Magnetic Order in $Pr_2Pd_3Ge_5$ and Possible Heavy-Fermion Behavior in $Pr_2Rh_3Ge_5$* , *Phys. Rev. B* **77**, 184407 (2008).
- [122] P. K. Das, N. Kumar, R. Kulkarni, and A. Thamizhavel, *Magnetic Properties of the Heavy Fermion Antiferromagnet $CeMg_3$* , *Phys. Rev. B* **83**, 134416 (2011).
- [123] P. Gegenwart, J. Custers, C. Geibel, K. Neumaier, T. Tayama, K. Tenya, O. Trovarelli, and F. Steglich, *Magnetic-Field Induced Quantum Critical Point in $YbRh_2Si_2$* , *Phys. Rev. Lett.* **89**, 056402 (2002).
- [124] E. D. Mun, S. L. Bud'ko, C. Martin, H. Kim, M. A. Tanatar, J.-H. Park, T. Murphy, G. M. Schmiedeshoff, N. Dilley, R. Prozorov, and P. C. Canfield, *Magnetic-Field-Tuned Quantum Criticality of the Heavy-Fermion System $YbPtBi$* , *Phys. Rev. B* **87**, 075120 (2013).
- [125] A. C. Y. Fang, S. R. Dunsiger, A. Pal, K. Akintola, J. E. Sonier, and E. Mun, *Magnetic Field Induced Effects in the Quasikagome Kondo Lattice System $CePtPb$* , *Phys. Rev. B* **100**, 024404 (2019).
- [126] C. D. Bredl, S. Horn, F. Steglich, B. Lüthi, and R. M. Martin, *Low-Temperature Specific Heat of $CeCu_2Si_2$ and $CeAl_3$: Coherence Effects in Kondo Lattice Systems*, *Phys. Rev. Lett.* **52**, 1982 (1984).
- [127] R. P. Hermann, R. Jin, W. Schweika, F. Grandjean, D. Mandrus, B. C. Sales, and G. J. Long, *Einstein Oscillators in Thallium Filled Antimony Skutterudites*, *Phys. Rev. Lett.* **90**, 135505 (2003).
- [128] P. Pyykkö, *Year-2017 Nuclear Quadrupole Moments*, *Molecular Physics* **116**, 1328 (2018).
- [129] N. J. Stone, *Nuclear Magnetic Dipole and Electric Quadrupole Moments: Their Measurement and Tabulation as Accessible Data*, *Journal of Physical and Chemical Reference Data* **44**, 031215 (2015).
- [130] S. Nakatsuji, Y. Machida, Y. Maeno, T. Tayama, T. Sakakibara, J. van Duijn, L. Balicas, J. N. Millican, R. T. Macaluso, and J. Y. Chan, *Metallic Spin-Liquid Behavior of the Geometrically Frustrated Kondo Lattice $Pr_2Ir_2O_7$* , *Phys. Rev. Lett.* **96**, 087204 (2006).
- [131] A. N. Medina, D. P. Rojas, F. G. Gandra, W. R. Azanha, and L. P. Cardoso, *Change of the Kondo Regime in $CePd_2Al_3$ Induced by Chemical Substitution: Verification of the Doniach Diagram*, *Phys. Rev. B* **59**, 8738 (1999).
- [132] C. L. Yang, X. Wang, X. Zhang, D. S. Wu, M. Liu, P. Zheng, J. Y. Yao, Z. Z. Li, Y.-F. Yang, Y. G. Shi, J. L. Luo, and N. L. Wang, *Kondo Effect in the Quasiskutterudite $Yb_3Os_4Ge_{13}$* , *Phys. Rev. B* **91**, 075120 (2015).
- [133] M. Niyafar, Ramani, M. C. Radhakrishna, A. Hassnpour, M. Mozaffari, and J. Amighian, *The Correlation of Lattice Constant with Superexchange Interaction in Bi-YIG Fabricated by Mechanochemical Processing*, in *ICAME 2007*, edited by N. S. Gajbhiye and S. K. Date (Springer Berlin Heidelberg, Berlin, Heidelberg, 2008), pp. 575–580.
- [134] A. Sumiyama, Y. Oda, H. Nagano, Y. Ōnuki, K. Shibusani, and T. Komatsubara, *Coherent Kondo State in a Dense Kondo Substance: $Ce_xLa_{1-x}Cu_6$* , *J. Phys. Soc. Jpn.* **55**, 1294 (1986).

- [135] T. Terashima, K. Kihou, M. Tomita, S. Tsuchiya, N. Kikugawa, S. Ishida, C.-H. Lee, A. Iyo, H. Eisaki, and S. Uji, *Hysteretic Superconducting Resistive Transition in $Ba_{0.07}K_{0.93}Fe_2As_2$* , Phys. Rev. B **87**, 184513 (2013).
- [136] P. C. Hohenberg, *Existence of Long-Range Order in One and Two Dimensions*, Phys. Rev. **158**, 383 (1967).
- [137] Y. Zhang, C. H. Wong, J. Shen, S. T. Sze, B. Zhang, H. Zhang, Y. Dong, H. Xu, Z. Yan, Y. Li, X. Hu, and R. Lortz, *Dramatic Enhancement of Superconductivity in Single-Crystalline Nanowire Arrays of Sn*, Sci Rep **6**, 32963 (2016).
- [138] Y. Xing, Z. Shao, J. Ge, J. Luo, J. Wang, Z. Zhu, J. Liu, Y. Wang, Z. Zhao, J. Yan, D. Mandrus, B. Yan, X.-J. Liu, M. Pan, and J. Wang, *Surface Superconductivity in the Type II Weyl Semimetal $TaIrTe_4$* , National Science Review **7**, 579 (2020).
- [139] J. Hu, S.-Y. Xu, N. Ni, and Z. Mao, *Transport of Topological Semimetals*, Annu. Rev. Mater. Res. **49**, 207 (2019).